

Steel Reinforcement Section Loss Guidance Tables

Behrouz Shafei, Principal Investigator
Institute for Transportation
Iowa State University

SEPTEMBER 2022

Research Report
Final Report 2022-32

To request this document in an alternative format, such as braille or large print, call [651-366-4718](tel:651-366-4718) or [1-800-657-3774](tel:1-800-657-3774) (Greater Minnesota) or email your request to ADArequest.dot@state.mn.us. Please request at least one week in advance.

Technical Report Documentation Page

1. Report No. MN 2022-32	2.	3. Recipients Accession No.	
4. Title and Subtitle Steel Reinforcement Section Loss Guidance Tables		5. Report Date September 2022	
		6.	
7. Author(s) Behrouz Shafei & Weizhuo Shi		8. Performing Organization Report No.	
9. Performing Organization Name and Address Institute for Transportation Iowa State University 2711 S. Loop Drive, Suite 4700 Ames, IA 50010		10. Project/Task/Work Unit No.	
		11. Contract (C) or Grant (G) No. (c) 1003320 (wo) 12	
12. Sponsoring Organization Name and Address Minnesota Department of Transportation Office of Research & Innovation 395 John Ireland Boulevard, MS 330 St. Paul, Minnesota 55155-1899		13. Type of Report and Period Covered Final Report	
		14. Sponsoring Agency Code	
15. Supplementary Notes https://www.mndot.gov/research/reports/2022/202232.pdf			
16. Abstract (Limit: 250 words) <p>The strength and durability of reinforced concrete (RC) bridges are adversely affected by the deterioration of their structural members. When investigating bridges in need of maintenance and repair, the deterioration due to the corrosion of steel rebars is commonly found to be a primary source of structural damage and degradation. To ensure the safety and performance of RC bridges while reducing their direct and indirect costs, an accurate estimate of the extent of reinforcement section loss has central importance for a wide spectrum of engineers and decision-making authorities.</p> <p>This research project investigated the steps required to achieve such rebar section loss estimates. To achieve this purpose, field assessments of rebar section loss were correlated with available predictive models and later calibrated to condition-specific field data. The outcome, which has been delivered in the form of steel reinforcement section loss guidance tables, directly contributes to understanding variability in rebar section loss when making loss predictions for use in structural evaluation. This facilitates planning preventive and/or corrective actions tailored to the condition state of deteriorating bridge elements.</p>			
17. Document Analysis/Descriptors Reinforcement (Engineering), Corrosion, Field studies, Predictive models		18. Availability Statement No restrictions. Document available from: National Technical Information Services, Alexandria, Virginia 22312	
19. Security Class (this report) Unclassified	20. Security Class (this page) Unclassified	21. No. of Pages 144	22. Price

STEEL REINFORCEMENT SECTION LOSS GUIDANCE TABLES

FINAL REPORT

Prepared by:

Behrouz Shafei, Ph.D., P.E.
Associate Professor
Institute for Transportation, Iowa State University

Weizhuo Shi, Ph.D.
Postdoctoral Research Associate
Institute for Transportation, Iowa State University

SEPTEMBER 2022

Published by:

Minnesota Department of Transportation
Office of Research & Innovation
395 John Ireland Boulevard, MS 330
St. Paul, Minnesota 55155-1899

This report represents the results of research conducted by the authors and does not necessarily represent the views or policies of the Minnesota Department of Transportation or Iowa State University. This report does not contain a standard or specified technique.

The authors, the Minnesota Department of Transportation, and Iowa State University do not endorse products or manufacturers. Trade or manufacturers' names appear herein solely because they are considered essential to this report.

ACKNOWLEDGMENTS

The Minnesota Department of Transportation (MnDOT) sponsored this research project. The following members served on the Technical Advisory Panel (TAP) for this project:

- Paul Pilarski
- Jessica Duncan
- Cory Stuber
- Sarah Sondag
- Eric Rustad
- Scott Larson
- Nickolas Haltvick

The authors would like to thank the TAP members, especially Paul Pilarski and Jessica Duncan, for their time, guidance, and feedback. The authors would also like to acknowledge the administrative coordination made by David Glycer throughout the course of this research project. The authors wish to thank Doug Wood, Owen Steffens, and Mia Wright for their assistance with the laboratory investigations performed in Iowa State University's Structures Laboratory. In addition, the technical support of Matthew Frank and Aaron Jordan for performing the rebar 3D scanning is gratefully acknowledged. Special thanks is also given to the MnDOT field engineers for collecting rebar samples from the bridge under consideration during the time that interstate travels were restricted due to the pandemic.

TABLE OF CONTENTS

CHAPTER 1: Introduction	1
CHAPTER 2: Literature Review	2
2.1 Direct Measurement for Rebar Section Loss	2
2.1.1 Destructive Testing Methods	2
2.1.2 Nondestructive Testing Methods	3
2.2 Corrosion Activity and Rate	3
2.2.1 Half-Cell Potential (HCP)	4
2.2.2 Electrical Resistivity (ER)	4
2.2.3 Galvanostatic Pulse Measurement (GPM)	5
2.2.4 Linear Polarization (LPR)	5
2.3 Prediction of Corrosion Rate	6
2.3.1 Mathematical Models	7
2.3.2 Empirical Models	8
2.3.3 Numerical Models	10
2.4 Factors Affecting the Corrosion Rate	10
2.4.1 Bridge Structure Environment	10
2.4.2 Concrete Quality	10
2.4.3 Depth of Concrete Cover	11
2.4.4 Extent of Exposure to Water and Deicing Salts	11
2.5 Factors Affecting Delamination	11
2.6 Overall Assessment	14
CHAPTER 3: Comparison and Formulation of Predictive Models	15
3.1 Empirical Models for Corrosion Rate Prediction	16
3.1.1 Alonso et al. (1988)	16
3.1.2 Morinaga (1990)	17
3.1.3 Liu and Weyers (1998)	19

3.1.4 Vu and Stewart (2000)	19
3.1.5 Li (2004a)	20
3.1.6 Li (2004b)	21
3.1.7 Pour-Ghaz et al. (2009)	22
3.2 Empirical Models for Predicting Structural Deterioration	23
3.2.1 Rodrigues et al. (1996).....	23
3.2.2 Vidal et al. (2004)	24
3.2.3 Zhang et al. (2010).....	24
3.2.4 Andrade et al. (2015).....	25
3.3 Numerical Models for Predicting Structural Deterioration	26
3.3.1 Qiao et al. (2016).....	26
3.3.2 Cheng et al. (2018)	26
3.3.3 Castorena-González et al. (2020)	26
3.4 Summary of Modeling Approaches.....	27
CHAPTER 4: Field Investigation Prior to Repair	28
4.1 Bridge details	28
4.2 Pier Maps	30
4.2.1 Pier 12WB	30
4.2.2 Pier 21EB.....	33
4.2.3 Pier 46WB	36
4.2.4 Pier 48EB.....	37
4.2.5 Pier 15EB.....	39
4.3 Rebar Sample Collection and Visual Assessments	42
CHAPTER 5: Sample Collection and Laboratory Tests.....	47
5.1 Sample Collection.....	47
5.2 Section Loss Measurement.....	48
5.2.1 3D Scanning.....	48

5.2.2 Comparison of Corrosion Level	58
5.3 Tensile Testing.....	62
5.4 Overall Assessment	67
CHAPTER 6: Predictive Models for Rebar Section Loss	68
6.1 Introduction	68
6.2 Models for Predicting Steel Section Loss.....	69
6.3 Situation I – Individual Cracks	70
6.3.1 Vidal et al. (2004)’s Model	70
6.3.2 Zhang et al. (2010)’s Model	71
6.3.3 Khan et al. (2014)’s Model	72
6.3.4 Final Model for Situation I	72
6.4 Situation II – Delamination and Spalling.....	73
6.4.1 Vidal et al. (2007)’s Model	74
6.4.2 Zhu et al. (2015)’s Model	74
6.4.3 Final Model for Situation II	76
CHAPTER 7: Conclusions and Implementation Steps	79
References	82
APPENDIX A: Photos of In-Progress Repairs	
APPENDIX B: Sample Extraction	

LIST OF FIGURES

Figure 3.1. Concrete electrical resistivity and corrosion rate, following Alonso et al. (1988)	16
Figure 3.2. Predicted steel loss as a function of time, following Alonso et al. (1988).....	17
Figure 3.3. Predicted steel loss as a function of time, following Morinaga (1990).....	18
Figure 3.4. Predicted steel loss over time, including the environmental parameters, following the modified model provided by Morinaga (1990).....	18
Figure 3.5. Predicted steel loss as a function of time, following Liu and Weyers (1998)	19
Figure 3.6. Predicted corrosion rate, following Vu and Stewart (2000)	20
Figure 3.7. Predicted steel loss, following Vu and Stewart (2000).....	20
Figure 3.8. Predicted corrosion rate, following Li (2004a)	21
Figure 3.9. Predicted steel loss, following Li (2004a)	21
Figure 3.10. Predicted steel loss, following Li (2004b): (a) different temperatures with $w/b = 0.45$ and (b) different w/b with $T = 10^{\circ}\text{C}$	22
Figure 3.11. Predicted crack width for concrete with different rebar section losses, following Zhang et al. (2010)	25
Figure 3.12. Predicted crack width, as a function of bar diameter, following Andrade et al. (2015)	25
Figure 3.13. Crack width analysis as a function of x_p (steel corroded cross-section after surface cracking)	27
Figure 4.1. Location of Bridge 27831 (highlighted area)	28
Figure 4.2. Design information from 1967 plans for Bridge No. 27831	30
Figure 4.3. Pier 12WB mapping diagrams (photo taken in 2018)	30
Figure 4.4. Location 14 of Pier 12WB	31
Figure 4.5. East face of Pier 12WB (photo taken in 2020)	31
Figure 4.6. West face of Pier 12WB (photo taken in 2020)	32
Figure 4.7. Pier 21EB mapping diagrams (east face, photo taken in 2018)	34
Figure 4.8. Location 7 of Pier 21EB.....	34
Figure 4.9. East face of Pier 21EB (photo taken in 2020)	35

Figure 4.10. West face of Pier 21EB (photo taken in 2020)	35
Figure 4.11. Pier 46WB mapping diagrams (east face, photo taken in 2018)	36
Figure 4.12. Location 9 of Pier 46WB	36
Figure 4.13. Pier 48EB mapping diagrams (east face, photo taken in 2018)	37
Figure 4.14. Location 8 of Pier 48EB.....	37
Figure 4.15. East face of Pier 48EB (photo taken in 2020)	38
Figure 4.16. West face of Pier 48EB (photo taken in 2020).....	39
Figure 4.17. Pier 15EB mapping diagrams (west face, photo taken in 2018)	40
Figure 4.18. Very thin bars between Beams 7 and 8 in Pier 15EB	40
Figure 4.19. Location 5 of Pier 15EB.....	40
Figure 4.20. East face of Pier 15EB (photo taken in 2020)	41
Figure 4.21. West face of Pier 15EB (photo taken in 2020).....	42
Figure 4.22. Rebar samples extracted from the studied piers.....	46
Figure 5.1. 3D laser scanner.....	49
Figure 5.2. 3D scanning for S1 sample: (a) before scanning, and (b) after scanning	49
Figure 5.3. Scanned rebar model treatment: (a) original model obtained from the 3D scanning; and (b) model treated using Geomagic software	50
Figure 5.4. Model modification in Matlab: (a) before modification and (b) after modification.....	50
Figure 5.5. Typical corrosion sectional area at a specific height.....	51
Figure 5.6. Measured cross-sectional area along the S1 bar	51
Figure 5.7. Cross-sectional area variation along the length of the rebar samples.....	58
Figure 5.8. Rebar samples extracted from the bridge piers under consideration	59
Figure 5.9. Rebar visual assessment for Pier 46WB: (a) 2018 inspection photo, (b) 2020 photo during repair, and (c) bar sample extracted from the pier.....	61
Figure 5.10. Tensile test setup used for the corroded steel bars.....	62
Figure 5.11. Failure points in the corroded rebars under tensile tests	64

Figure 5.12. Load versus displacement curve for the corroded steel bars.....	65
Figure 5.13. Summary of tensile test results	66
Figure 6.1. Schematic illustration of various stages of corrosion	69
Figure 6.2. Comparison of the developed predictive model with the experimental test data from Vidal et al. (2004).....	70
Figure 6.3. Comparison of the developed predictive model with the experimental test data from Zhang et al. (2010).....	71
Figure 6.4. Comparison of the developed predictive model with the experimental test data from Khan et al. (2014).....	72
Figure 6.5. Developed plot for predicting steel section loss in Situation I	73
Figure 6.6. Comparison of the developed predictive model with the experimental test data from Vidal et al. (2007).....	74
Figure 6.7. Comparison of the developed predictive model with the experimental test data from Zhu et al. (2015) for (a) pitting corrosion and (b) uniform corrosion	75
Figure 6.8. Developed plot for predicting steel section loss in Situation II	76
Figure 6.9. An example of how the crack details recorded during an inspection can be used to obtain the input required for the developed predictive models.....	78
Figure 7.1. Snapshot of the spreadsheet developed to predict the extent of section loss	80
Figure A.1. East face of Pier 12WB	1
Figure A.2. South end of east face of Pier 12WB	1
Figure A.3. Spalling on south end of east face Pier 12WB.....	2
Figure A.4. Rebar section loss in spalling, east face Pier 12WB, with rebar diameters approximately 1/2" and 3/8", respectively	2
Figure A.5. West face of Pier 12WB	3
Figure A.6. Spalling and delamination on north side of the west face of Pier 12WB.....	3
Figure A.7. Spalling on west face of Pier 12WB showing longitudinal and stirrup rebar	4
Figure A.8. Corroded stirrup rebar diameter 9/16" on west face of Pier 12WB.....	4
Figure A.9. North end of Pier 12WB showing significant spalling on corners and exposure of longitudinal and stirrup rebar	5

Figure A.10. East face of Pier 15EB showing significant areas of delamination on top of the pier between beams on south side of beam and on bottom of the pier on the north side of the beam	6
Figure A.11. Spalling and delamination on east face of Pier 15EB showing exposed longitudinal and stirrup rebars between piles 3 and 4.....	6
Figure A.12. Exposed rebar to the north of pile 3 on Pier 15EB	7
Figure A.13. West face of Pier 15EB showing notable spalling on south end of the pier, delamination on top of beam above pile 5.....	7
Figure A.14. Vertical and horizontal portions of exposed stirrup shown in Pier 15EB Figure A.3, with rebar diameters of 19/32" and 3/8", respectively	8
Figure A.15. West end of Pier 15EB showing two areas of spalling, with entire south corner having rebar exposed nearly to pile 6.....	8
Figure A.16. South end of Pier 15EB showing nine stirrups and all longitudinal rebar on the west face entirely or partially exposed, as well as delamination on top and bottom of pier, most notably on the top near the midpoint of the two piles	9
Figure A.17. North end of west face of Pier 15EB showing corner and face spalling as well as delamination on the top of the pier	9
Figure A.18. Exposed stirrups on south end of the west face of Pier 15EB, with rebar diameters of 3/8" and 7/16", respectively.....	10
Figure A.19. Top of Pier 15EB at north-most beam connection, with connections showing extreme deterioration and corrosion and spalling evident at top of pier.....	11
Figure A.20. Spalling and delamination at north end of Pier 15EB	11
Figure A.21. Underneath Pier 15EB at pile 1, with rust stains present and spalling exposing longitudinal and stirrup rebar	12
Figure A.22. West face of Pier 15EB showing multiple spalling and delamination areas at north side of the pier	12
Figure A.23. South end of west face of Pier 15EB showing spalling on face of the pier, delamination on top and bottom of pier	13
Figure A.24. Severely corroded rebar specimens from south end of Pier 15EB	13
Figure A.25. East face of Pier 21EB showing pier encapsulated in RC.....	14
Figure A.26. Northern side of the east face of Pier 21EB showing spalling where concrete has fallen off as well as areas where concrete was retained during spalling	14

Figure A.27. Area of spalling on east face of Pier 21EB where stirrup rebar is exposed.....	15
Figure 28. Exposed corroded rebar with diameter of 3/4"	15
Figure A.29. West face of Pier 21EB	16
Figure A.30. North end of west face of Pier 21EB showing one area of spalling with exposed rebar	16
Figure A.31. Spalling with exposed stirrups on west face of Pier 21EB.....	17
Figure A.32. Exposed corroded rebar with diameter of 1/2"	17
Figure A.33. West face of Pier 48EB showing delamination between multiple columns and on the columns themselves	18
Figure A.34. Close-up of delaminated area in the center of the west face of Pier 48EB	18
Figure A.35. Underneath angle showing severe delamination on Pier 48EB	19
Figure A.36. East face of Pier 48EB.....	19
Figure A.37. Delamination exposing corroded rebar on top of Pier 48EB from the east face at the north side of the pier	20
Figure A.38. Exposed longitudinal and stirrup rebar with minimal corrosion from section shown in Figure A. 37, with rebar diameters of about 1/2" and 1 1/2", respectively.....	20
Figure A.39. Severely corroded stirrups, broken over top of Pier 48EB, and diameter reduced to approximately 1/2" on the east side	21
Figure A.40. Connection on top of Pier 48EB showing corrosion on the connecting plates and bolts	21
Figure A.41. East face of Pier 48EB.....	22
Figure A.42. Corroded longitudinal bars in area shown in Figure A.37, with rebar diameters of about 1 1/2"	22
Figure A.43. Delaminated area shown in Figure A.37 from the east side of Pier 48EB.....	23
Figure A.44. Exposed longitudinal bars with little corrosion on the east face of Pier 48EB.....	23
Figure A.45. Exposed rebar with mild corrosion from area in Figure A.37, with rebar diameters of 1 1/2" and 1/2", respectively.....	24
Figure A.46. Additional delaminated area on the west face of Pier 48EB.....	24
Figure A.47. Exposed rebar in area from Figure A.46, showing both stirrups and longitudinal bars	25
Figure B.1. Original design reinforcement.....	1

Figure B.2. Pre-project inspection sketches.....	2
Figure B.3. Sample rebar collection sites during contract repairs	3
Figure B.4. Original design reinforcement.....	4
Figure B.5. Pre-project inspection sketches.....	5
Figure B.6. Sample rebar collection sites during contract repairs	6
Figure B.7. Original design reinforcement.....	7
Figure B.8. Pre-project inspection sketches.....	8
Figure B.9. Sample rebar collection sites during contract repairs	9
Figure B.10. Original design reinforcement.....	10
Figure B.11. Pre-project inspection sketches.....	11
Figure B.12. Sample rebar collection sites during contract repairs. Note that bar size for sample S9 exhibited larger than normal cross-sectional area for #5 rebar and therefore was assigned a #6 rebar designation in laboratory.....	12

LIST OF TABLES

Table 1.1. Overview of the benefit categories of the research investigation.....	1
Table 2.1. Probability of corrosion according to half-cell readings.....	4
Table 2.2. Rate of corrosion according to resistivity	5
Table 2.3. Rate of corrosion according to LPR measurements	6
Table 2.4. Mathematic models available in the literature for the prediction of corrosion rate.....	7
Table 2.5. Empirical models published in the past regarding the prediction of corrosion rate	8
Table 3.1. Main influential factors	15
Table 3.2. The constants in the model provided by Pour-Ghaz et al. (2009)	23
Table 4.1. Piers studied in this research project	29
Table 4.2. Notes and description with locations identified in Figure 4.5	32
Table 4.3. Notes and description with locations identified in Figure 4.6	33

Table 4.4. Notes and description with locations identified in Figure 4.9	35
Table 4.5. Notes and description with locations identified in Figure 4.10	35
Table 4.6. Notes and description with locations identified in Figure 4.15	38
Table 4.7. Notes and description with locations identified in Figure 4.16	39
Table 4.8. Notes and description with locations identified in Figure 4.19	41
Table 4.9. Notes and description with locations identified in Figure 4.20	42
Table 4.10. Survey results of general steel section loss based on visual assessment.....	43
Table 4.11. Survey results of local steel section loss based on visual assessment	44
Table 5.1. Rebar sample information	48
Table 5.2. Maximum section loss expressed in percentage (%) of full bar length from each specimen (based on worst section loss).....	59
Table 5.3. Average section loss expressed in percentage (%) for each specimen	61
Table 5.4. Comparison of laboratory test results to visually assessed and measured area losses.....	67
Table 6.1. Constants obtained for the power function based on the data from Vidal et al. (2004)	71
Table 6.2. Constants obtained for the power function based on the data from Zhang et al. (2010)	71
Table 6.3. Constants obtained for the power function based on the data from Khan et al. (2014)	72
Table 6.4. Constants obtained for the power function for Situation I model.....	73
Table 6.5. Constants obtained for the power function based on the data from Vidal et al. (2007)	74
Table 6.6. Constants obtained for the power function based on the data from Zhu et al. (2015)	75
Table 6.7. Constants obtained for the power function for Situation II model.....	76
Table 6.8. Mean section loss at 10-year increments.....	77

EXECUTIVE SUMMARY

Bridge structures in Minnesota are designed for a service life of (at least) 75 years. However, the strength and durability of reinforced concrete (RC) bridges are adversely affected by the deterioration of their structural members within this lifetime. When investigating bridges in need of maintenance and repair, deterioration caused by corrosion of steel rebars is commonly found as a primary source of structural degradation. Structural degradation may result in a reduced service life and is almost always associated with service interruption for maintenance and repair. Corrosion reduces the cross-sectional area of the original steel and forms expansive corrosion byproducts. These corrosion byproducts cause cracks, concrete spalling, delamination, and even bond loss in RC bridge elements.

Management of a bridge structure requires understanding the structural capacity of the bridge. An accurate assessment of reinforcement section loss (without underestimation or overestimation) is necessary for both structural evaluation and capacity determination. Furthermore, the structural capacity dictates any strengthening needs and associated temporary works in a repair effort. Therefore, an accurate estimate of the extent of reinforcement section loss has central importance for a wide spectrum of engineers and decision-making authorities. Reinforcement section loss estimates are key for safety assessments and programming repairs. These estimates can be achieved using available predictive models calibrated with condition-specific data and then validated through appropriate field investigations. Beyond immediate safety benefits, accurate reinforcement section loss estimates benefit the design and extent of strengthening. In particular, having accurate section loss estimates and structural evaluations reduces the risk of unforeseen revisions during contract repair work.

To quantify the extent of corrosion and reinforcement section loss in the bridge structures currently in service in Minnesota, this research project utilized in-service Bridge No. 27831 (I-394) near Dunwoody Institute in Minneapolis. This site provided direct access to several bridge piers scheduled for repair beginning in spring 2020. Upon the initiation of repair activities in the field, visual section loss assessments were performed. This was then followed by collecting samples of steel rebar from the bridge piers for a direct assessment of the extent of corrosion and quantification of cross section loss. Complementary laboratory tests were performed on the collected rebar samples to measure the mechanical properties of corroded rebars. With the first-hand information obtained regarding the extent of corrosion in real settings, a set of predictive models and their associated variables were identified for the prediction of rebar cross section loss.

The outcome of this research project led to the section loss guidance tables that will be ready for implementation after additional calibration. Due to the pandemic, the developed models had to be tested with limited data from only one bridge. Thus, despite the relative success of the guidance tables in capturing the overall condition of bridges in Minnesota, the range of section loss predictions remained relatively large. To narrow this range and tailor it to various exposure conditions, further data and sample collection from additional structural configurations and environmental exposures will be required. The developed rebar section loss guidance tables will improve bridge inspection value and reduce direct costs by right-sizing bridge repairs to the correct deterioration condition. Indirect costs due to bridge closure, disruption in traffic, and impact on the surrounding environment will also be

minimized. The section loss guidelines will help MnDOT better manage its bridge inventory and make more informed decisions about bridge safety, bridge repair, and ultimately optimization of bridge replacement timeframes.

CHAPTER 1: INTRODUCTION

To repair deteriorated reinforced concrete (RC) structures, an understanding of the extent of steel corrosion has a pivotal role in deciding on the best strengthening strategies and details. This understanding helps ensure that the remaining structural capacity is estimated without underestimation or overestimation. Such estimates can be achieved using available predictive models calibrated with region-specific data and then validated through appropriate field investigations. Accurate reinforcement section loss is necessary for structural evaluation and to determine load carrying capacity of affected members. This is essential for planning preventive and/or corrective actions tailored toward maintaining the bridges in a desired condition state. Beyond immediate safety benefits, sensible practical advantages are anticipated since the design of strengthening details will be based on a realistic condition assessment of bridges. Having accurate section loss estimates and structural evaluations will, in particular, reduce the risk of unforeseen revisions during contract repair work.

To quantify the extent of corrosion and reinforcement section loss in the bridge structures currently in service in Minnesota, this research project utilized in-service Bridge No. 27831 (I-394) near Dunwoody Institute in Minneapolis. This site provided direct access to several bridge piers scheduled for repair beginning in spring 2020. Upon the initiation of repair activities in the field, visual section loss assessments were performed. This was then followed by collecting samples of steel rebar from the bridge piers for a direct assessment of the extent of corrosion and quantification of cross section loss. Complementary laboratory tests were performed on the collected rebar samples to measure the mechanical properties of corroded rebars. With the first-hand information obtained regarding the extent of corrosion in real settings, a set of predictive models and their associated variables were identified for the prediction of rebar cross section loss. Table 1.1 summarizes the main benefits of this holistic research investigation.

Table 1.1. Overview of the benefit categories of the research investigation

Benefit category	How will these key benefits be quantified?
Construction savings	Saving in construction materials by a proper use of available structural capacity
Decrease engineering and administrative costs	Reducing discrepancies between the values assumed for design and those found in the field
Improved lifecycle costs	Minimizing both direct and indirect costs through realistic design assumptions
Operation and maintenance saving	Improving the effectiveness of maintenance and repair activities for bridge structures
Reduce risk and road user costs	Reducing the duration of repairs by minimizing the risk of discrepancies in rebar corrosion extents.

CHAPTER 2: LITERATURE REVIEW

Several corrosion measurement methods have been developed to date for assessing the corrosion of reinforcing steel embedded in concrete. Rodriguez et al. (1994) conducted a holistic review of methods for monitoring the corrosion in reinforced concrete (RC) and summarized the features of available measuring methods, i.e., the speed of a single measurement, the speed of response to changing conditions, the ability to provide quantitative corrosion data, and non-destructive characteristics. It was concluded that the linear polarization method and the polarization resistance method can be the most suitable quantitative electrochemical methods for the estimation of the corrosion current density, i_{corr} . In a similar review study, Song and Saraswathy (2007) summarized all the known electrochemical and nondestructive techniques for corrosion assessment and their applications to bridges and other civil engineering structures. It was found that, although each electrochemical measurement had certain benefits, many of them dealt with significant limitations. The performance of embedded sensors was also determined to be promising, resulting in reduced costs and allowing rational assessments of corrosion for reinforcing steel. A more recent review of the corrosion measuring methods was conducted by Gucunski et al. (2011 and 2012) to determine the extent of rebar corrosion in concrete bridge decks. This chapter provides an overview of various corrosion measurement methods (both direct and indirect) and the factors influencing them.

2.1 DIRECT MEASUREMENT FOR REBAR SECTION LOSS

2.1.1 Destructive Testing Methods

The cross-sectional area of corroded rebars along their length can be quantified by direct measurements in the field or laboratory tests (Alipour et al., 2011 and 2013). After necessary clean-ups, the weight loss ratio of reinforcement (due to corrosion) can be calculated by the following equation.

$$\eta_s = (m_0 - m_s)/m_0 \quad (2.1)$$

where η_s is the mass loss ratio, m_0 is the weight of an uncorroded rebar segment, and m_s is the weight of a corroded rebar segment after cleaning. Thus, the average corrosion penetration depth can be estimated by:

$$P_{ave} \approx \eta_s \cdot \frac{D_0}{4} \quad (2.2)$$

where P_{ave} represents the average corrosion penetration depth (section loss), and D_0 represents the diameter of the uncorroded rebar.

The destructive methods can be time-consuming and inefficient. Alternatively, the minimum cross-sectional area and maximum penetration depth of corrosion can be directly measured by an electronic Vernier caliper. However, such types of measurement lack accuracy due to the complexity of the corrosion topography, such as the nonuniform corrosion characteristic. Therefore, some research investigations have used other direct measurement techniques. For example, Zhang et al. (2014)

performed a study to investigate a probabilistic model for the cross-sectional area of corroded reinforcing steel bars. In this study, a three-dimensional laser scanning technique was used, to measure the shape of the corroded bar after acid cleaning and drying. The 3D scanning models appear very comparable to actual morphology.

2.1.2 Nondestructive Testing Methods

X-ray and digital image processing techniques are found in the existing studies to assess the steel corrosion in concrete. Lim et al. (2016) conducted an experimental study to investigate the steel weight loss along the corroded rebars using X-ray and digital image processing techniques. The specimen was first tested under X-ray radiography with different viewing angles. The recorded photos were then employed to estimate the steel volume loss. The use of X-ray at different angles, however, would have very limited applicability in the field and be available only for the steel that is accessible from different angles.

Another measurement technique is using ground-penetrating radar. Ground-penetrating radar is a geophysical testing method that uses a radiated electromagnetic wave from a transmitting antenna (Jol 2009). When the wave travels through a material and encounters an object with different dielectric properties, a scattered pulse that can be detected by a receiving antenna will be generated. GPR has been widely used in the detection of underground utilities and scanning of concrete structures, such as in assessing slab layer thickness, determining rebar location, and identifying deficiencies (i.e., debonding, voids, moisture, etc.). However, this technique has experienced some challenges in the detection of rebar section loss due to corrosion in concrete.

Chintakunta (2014) conducted a study to evaluate steel corrosion in concrete barriers using four different non-destructive evaluation (NDE) methods. Although GPR was found to be more promising than other methods, i.e., low-frequency ultrasonic tomography, infrared thermography, and digital radiography, it was concluded that the section loss in the rebars measured from GPR was not evident. Eisenmann and Margetan (2018) performed a study to detect material loss in reinforcing steel in concrete barriers using GPR and magnetic flux leakage (MFL). They reported that the results were not as promising as anticipated, primarily due to the difficulty of data interpretation caused by the signal reflection complexity. They also recommended that the capability of the GPR technique in evaluating rebar loss would require much future validation.

2.2 CORROSION ACTIVITY AND RATE

Direct corrosion measurements will provide only an instantaneous assessment of the current condition of corroded/uncorroded reinforcement in concrete, but current density measurement can be used to predict future rebar section loss in terms of metal loss based on Faraday's second law (Darwin et al., 2002; Khatami et al., 2021), as shown in Eq. 2.3. This section reviews the NDE methods for evaluating the corrosion rate of reinforcing steel in concrete, which can be subsequently used to estimate reinforcement section loss.

$$r = \frac{ia}{nFD} \quad (2.3)$$

where r is the corrosion rate ($\mu\text{m}/\text{yr}$), i is the corrosion current density (measured, amperes/ cm^2 or coulombs/ $\text{cm}^2\text{-sec}$), a is the atomic weight (55.84 g for iron), n is the number of equivalents exchanged (2 electrons transferred for Fe^{2+}), F is Faraday's Constant which (96,500 coulombs/mole), and D is the density of metal ($7.87 \text{ g}/\text{cm}^3$ for steel).

2.2.1 Half-Cell Potential (HCP)

Since corrosion can be described as an electrochemical reaction in which the reinforcing bar transfers electrons from an anode to a cathode, a potential difference and associated corrosion current can be generated during the corrosion process. The half-cell potential test, standardized as ASTM C876 (2016), has been used to determine the corrosion activity of reinforcing bars in concrete by estimating the electrical corrosion potential. Half-cell potential readings do not measure reinforcement section loss but will give indications of corrosion activity.

In general, the potential difference between the rebar and the reference electrode can be mapped as the measurement point moves on the concrete surface. According to ASTM C876 (2016), the probability of corrosion according to half-cell readings with Cu/CuSO₄ electrodes can be documented as in Table 2.1. Elsener and Böhni (1992) conducted a field study to assess rebar corrosion using this method. They found that a grid spacing of 100 cm provided sufficient accuracy in locating the corrosion zone. The primary limitation of the half-cell potential method is that the extent of past corrosion (i.e., rebar section loss due to corrosion) could not be directly measured. Also, some factors, such as the existence of high resistance layers in concrete, the conductivity of formed corrosion products, the age of concrete, the position of the reference electrode, cement type, and presence of cracks, all have great potential to affect measurement reliability (Shafei, 2011; Shafei and Alipour, 2015 a,b).

Table 2.1. Probability of corrosion according to half-cell readings

Half-cell potential reading vs. Cu/CuSO ₄	Corrosion activity
less negative than -200 mV	90% probability of no corrosion
between -200 mV and -350 mV	increasing the probability of corrosion
more negative than -350 mV	90% probability of corrosion

2.2.2 Electrical Resistivity (ER)

Electrical resistivity (ER) (ASTM G57 2015) can be used to determine corrosion activity for RC structures, especially the regions susceptible to moisture and chloride penetration. With increasing the ER of the concrete, the current passing between the anodic and cathodic areas of the reinforcement decreases, reflecting a reduced corrosion rate. For measuring concrete resistivity, a Wenner probe, which has four equally spaced probes, can be utilized.

Resistivity measurement can be used in conjunction with other corrosion assessment techniques to provide a more comprehensive assessment of corrosion (Gowers and Millard 1999). Table 2.2 presents the relationship between the resistivity of reinforced concrete and the corrosion rate. Rapid measurement, data reading, recording, and processing are the significant advantages of the ER method, although the interpretation of results can be challenging due to some of the concrete properties, such as moisture, salt content, and porosity. The reinforcing steel embedded in the concrete can also affect the resistivity measurements. This requires the knowledge of the reinforcement position for ER values to be fairly interpreted.

Table 2.2. Rate of corrosion according to resistivity

Resistivity [kohm.cm]	Corrosion rate
< 5	Very high
5-10	High
10-20	Moderate - low
> 20	Low

2.2.3 Galvanostatic Pulse Measurement (GPM)

Galvanostatic pulse measurement (GPM), an electrochemical NDE method using a current pulse, can be used to determine corrosion rate in reinforcing bars. GPM is based on rebar polarization. Since GPM is more reliable than the HCP method when concrete is wet or dense, a more realistic measurement of corrosion rate in reinforcing steel can be achieved (Elsener et al. 2003; Elsener and Böhni 1992; Gucunski et al. 2012).

Unlike the HCP and ER methods, the GPM method can be used to indirectly measure the corrosion rate. Bäßler et al. (2003) conducted a laboratory study to investigate the relationship between the GPM-measured results and the actual corrosion values. Additionally, based on a laboratory study by Sørensen and Frølund (2002), it was recommended that conducting supplementary investigations to identify the source of delamination of concrete cover, i.e., carbonated concrete or chloride-contaminated concrete, is important when measuring the corrosion rate using GPM. It was also pointed out that the corrosion rate measured using GPM could only reflect the current corrosion condition and the projected corrosion rate would be influenced by environmental factors, such as moisture, temperature, and oxygen concentration.

2.2.4 Linear Polarization (LPR)

Linear polarization resistance measurement is an electrochemical method that can be used to determine the corrosion rate of the reinforcing bars in concrete by scanning over the current–potential (i–E) domain. In this method, a direct current, needed to maintain a specific voltage shift (typically 10 mV), is passed through the system to excite the steel-concrete interface, and the corrosion rate can then be calculated. The primary advantage of this method is its speed of response to corrosion rate changes.

This method has been found to be more effectively used in tandem with other corrosion assessment techniques, such as HCP, through which a corrosion map can be determined. As previously mentioned, a current can be generated within a micro electrolytic cell by the potential difference resulting from corrosion. Thus, in this oxidation-reduction reaction, the ferrous ions tend to move into the adjacent concrete, leaving free electrons on the steel rebar and creating a negative charge that can be used to locate the corroded regions using the HCP method. The LPR can then be used to determine the rebar corrosion rate. Table 2.3 presents typical values of corrosion rates determined by LPR measurements (Andrade and Alonso 1996).

Table 2.3. Rate of corrosion according to LPR measurements

Corrosion classification	Corrosion current density	Corrosion penetration rate
Passive/Very low	Up to 0.2 $\mu\text{A}/\text{cm}^2$	Up to 2 $\mu\text{m}/\text{year}$
Low/Moderate	0.2 $\mu\text{A}/\text{cm}^2$ to 0.5 $\mu\text{A}/\text{cm}^2$	2 $\mu\text{m}/\text{year}$ to 6 $\mu\text{m}/\text{year}$
Moderate/High	0.5 $\mu\text{A}/\text{cm}^2$ to 1.0 $\mu\text{A}/\text{cm}^2$	6 $\mu\text{m}/\text{year}$ to 12 $\mu\text{m}/\text{year}$
Very high	> 1.0 $\mu\text{A}/\text{cm}^2$	> 12 $\mu\text{m}/\text{year}$

Pradhan and Bhattacharjee (2009) performed an experimental study of various corrosion rate techniques to investigate the corrosion performance of different types of rebar in chloride-contaminated concrete. Close agreement, with an average percentage variation of $\pm 6\%$, was obtained between the values of corrosion current density measured from the LPR method with a guard ring electrode and those estimated from gravimetric (mass loss) measurements. A detailed practical guide for using LPR to measure the corrosion rate of RC structures can be found in Millard and Broomfield (2003).

2.3 PREDICTION OF CORROSION RATE

The corrosion rate (i.e., i_{corr}) in the steel bars embedded in RC structures has been incorporated in various corrosion models. Tuutti (1982) developed a conceptual model for predicting the extent of corrosion in RC structures. In this model, reinforcement corrosion may be divided into two stages, i.e., an initiation stage and a propagation stage. In the initiation stage, the chloride ions diffuse toward steel bars through the concrete (Hajilar and Shafei, 2018 a,b). This initiation stage may be thought of as the chloride transport time. The length of the initiation period depends on several parameters, such as cover depth, water-to-cement (w/c) ratio, curing regime, cement type, and ambient temperature (Ranjith et al., 2016). In the second stage, however, the chloride ions are accumulated on the rebar surface to a level that exceeds the corrosion threshold (Shi et al., 2020 a,b). This destroys the protective film around the rebar and generates the voluminous rust materials.

There are a number of studies that develop models to predict the corrosion rate of reinforcement steel in concrete. The corrosion rate, i_{corr} , is dependent on many factors and can be expressed as follows (COIN, 2008):

$$i_{corr} = f(k_1, k_2, \dots, k_n) \quad (2.4)$$

where k_1, k_2, \dots, k_n represent several internal and external factors affecting the corrosion rate, e.g., the use of supplementary cementitious materials, moisture content, cyclic wetting and drying, sustained loading, loading history, concrete resistivity, concrete quality, cover depth, cover cracking, temperature, dissolved oxygen concentration, chloride concentration, and exposure condition. Overall, the predictive models have been established based on either a mathematical approach or an empirical approach, involving the electrochemical principles, statistical analyses, and experimental test results.

2.3.1 Mathematical Models

Mathematical models are mainly based on solving the corrosion-governing equations. A number of mathematical models for predicting the corrosion rate have been identified and presented in Table 2.4.

Table 2.4. Mathematic models available in the literature for the prediction of corrosion rate

Researchers	Proposed models	Comments
Bazant et al. (1979)	$t_{corr} = \rho_{corr} \frac{D\Delta D}{pj_r}$	This model is for the prediction of corrosion damage considering the volume expansion due to the formation of rust.
Morinaga (1988)	$Q_{corr} = 0.602D(1 + \frac{2C_V}{D})^{0.85}$	This model is to measure the corrosion of steel (Q_{corr}) when the concrete cover breaks due to the expansion of rust.
Molina et al. (1993)	$t_p = \frac{\Delta r}{i_{corr}}$	This model is to estimate the decrease of rebar radius, which produces 0.3 – 0.4 mm crack width.
Maruya et al. (2003)	$\phi_{ma,c} - \phi_{ma,a} = \rho L_{ac} i_{corr}$	Both the initiation and propagation stages of corrosion are included in this model.
Gulikers (2005)	$i_{corr} = \frac{F_G^{-0.8125} (98.696 \times 10^{-3})}{\rho^{0.8125}}$	This model is independent of the geometry of the RC structure but may vary substantially due to environmental effects.
Song et al. (2005)	$\log i_{corr} = 8.458 - 0.508\text{pH} + 0.5 \log i_{o,c} + 0.51 \log i_{o,a}$	This model is based on the state of the passive film.
Huet et al. (2007)	$i_{corr} = n_e F s_a \lambda k_{O_2} \varepsilon^2 S_r C_{O_2,liquid}(x_2)$ where $\lambda = \sqrt{\frac{D_{O_2,liquid}}{s_a k_{O_2} \varepsilon^2 S_r}}$	This model is based on the diffusion process of O_2 into concrete, causing steel corrosion.

Notes:

- t_{corr} - steady-state corrosion or propagation period (years).
- ρ_{corr} - combined density factor for steel and rust (3600 kg/m³).
- D - diameter of rebar (mm).
- ΔD - increase in diameter of rebar due to rust formation (cm).
- p - perimeter of bar (mm).
- j_r - instantaneous corrosion rate of rust (g/m²-s).
- Q_{cr} - amount of corrosion when concrete cracks (×10⁻⁴g/cm²).
- C_V - concrete cover thickness (mm).
- $\phi_{ma,c}$ and $\phi_{ma,a}$ - cathodic and anodic macro-cell potentials, respectively (V).
- ρ - concrete resistivity (Ω-m).
- L_{ac} - distance between the anode and cathode.

i_{corr} - corrosion rate (A/m²).

F_G - geometry factor (m⁻¹).

n_e - valence number.

F - Faraday's constant.

s_a - specific surface of the oxide layer per unit volume ($\approx 3.7 \times 10^7$ m²/m³).

k_{O_2} - kinetic constant of oxygen reduction ($\approx 10^{-1}$ ms⁻¹).

$C_{O_2,liquid}(x_2)$ - O₂ concentration in the pore solution per unit volume of concrete.

$D_{O_2,liquid}$ - diffusion coefficient of species in the concrete pore solution.

2.3.2 Empirical Models

Empirical models are established using the laboratory test results and are usually based on direct relationships assumed between the corrosion rate and various concrete parameters, including binder type, water-to-cement ratio, and environmental conditions (Bjegovic et al., 2006). A number of empirical models have been developed for predicting the corrosion rate, as presented in Table 2.5.

Table 2.5. Empirical models published in the past regarding the prediction of corrosion rate

Researchers	Proposed models	Comments
Alonso et al. (1988)	$i_{corr} = \frac{k_{corr}}{\rho_{ef}}$	This model is based on a statistical analysis of resistivity and accelerated carbonation-induced corrosion rate results. It was demonstrated that, in addition to concrete resistivity, the presence of cracks and concrete cover depth may significantly affect the corrosion rate (Otieno et al., 2010).
Morinaga (1990)	$i_{corr} = \frac{d_{st}}{d^2} (-0.51 - 7.60C_{Cl} + 44.97 (w/b)^2 + 67.95C_{Cl}(w/b)^2)$	This model is based on the chloride-induced corrosion prediction and does not incorporate environmental parameters.
	$i_{corr} = 2.59 - 0.05T - 6.89(h - 0.45) - 22.87C_{O_2}^{air} - 0.99C_{Cl} + 0.14(h - 0.45) + 0.51TC_{O_2}^{air} + 0.01TC_{Cl} + 60.81(h - 0.45)_{O_2}^{air} + 3.36(h - 0.45)C_{Cl} + 7.32_{O_2}^{air}C_{Cl}$	Even though this updated model includes the environmental parameters, the parameters relating to concrete material properties, such as binder type and water-to-binder ratio, are not considered.
Morinaga (1996)	$m_{corr} = B_{corr}t$	This model is based on the assumption that i_{corr} increases with increasing the moisture and O ₂ .
Liu and Weyers (1998)	$i_{corr} = 102.47 + 10.09 \ln(1.69Cl) - 0.0015\rho - \frac{39038.96}{T} + \frac{290.91}{t^{-0.215}}$	This model is based on a statistical analysis of experimental results, which were measured from a 5-year accelerated corrosion testing program. It was demonstrated that the corrosion rate is a function of the chloride content, temperature, resistivity of the concrete, and active corrosion time.
DuraCrete (1998)	$i_{corr} = \frac{k_{corr}}{\rho(t)} F_{Cl} F_{galv} F_{oxide} F_{oxy}$ $\rho(t) = \rho_0 f_{ef} t \left(\frac{t}{t_0} \right)^n$	This model is based on several factors, but there are no guidelines provided on how to obtain the values.

Researchers	Proposed models	Comments
Vu and Stewart (2000)	Corrosion initiation: $i_{corr(1)} = \frac{37.8(1-w/b)^{-1.64}}{c}$ Corrosion propagation: $i_{corr} = i_{corr(1)} 0.85 t_p^{-0.29} = \left(\frac{32.13(1-w/b)^{-1.64}}{c}\right) t_p^{-0.29}$	This model is proposed with the assumption that the availability of oxygen at the steel surface is the governing factor to predict the corrosion rate. However, it does not consider the factor of concrete quality.
Scott (2004)	$i_{corr} = \left(1.43 \frac{Cl_{90}}{f} + 0.02\right) \exp\left[\left(\frac{40-c}{20}\right) 1.2 \left(\frac{Cl_{90}}{f}\right)^3\right]$	This model is based on the experimental test results on the cracked specimens.
Martinez and Andrade (2009)	$i_{corr}^{rep} = \frac{i_{corr}^{sing} + i_{corr}^{max}}{2}$	Based on concrete resistivity, this model can predict the average annual corrosion rate. With the assumption of anodic- or resistivity-controlled, differences can be found due to the concrete quality.
Pour-Ghaz et al. (2009)	$i_{corr} = 100 \left\{ \frac{1}{\tau \rho^{\gamma}} [\eta T d^{\kappa} i_L^{\lambda} + \mu T \nu i_L^{\omega} + \theta (T i_L)^{\vartheta} + \chi \rho^{\nu} + \zeta] \right\}$	This model is based on a closed-form regression analysis, establishing the correlations between the corrosion rate and ambient temperature, kinetic parameter, concrete resistivity, and limiting current density.
Zhang et al. (2010)	$w_c = 0.1916 \Delta A_{SM} + 0.164$	This model correlates the crack width and average cross-sectional loss of corroded reinforcement.
Andrade et al. (2015)	$w_c = 15.683 \left(\frac{x_{ave}}{R_0} CT\right)^{0.928}$	This model provides the relationship between the crack width and other parameters.

Notes:

k_{corr} - a constant ($3 \times 10^4 \mu\text{A}/\text{cm}^2/\text{k}\Omega\text{-cm}$).

ρ_{ef} - resistivity of concrete at its actual degree of saturation.

d_{st} - diameter of the reinforcing steel (mm).

d - concrete cover (mm).

C_{Cl} - chloride content (% of NaCl by mass of mixing water).

T - temperature ($^{\circ}\text{C}$).

h - relative humidity (%).

$C_{O_2}^{air}$ - concentration of O_2 in the air (%).

m_{corr} - mass loss ($\times 10^{-4} \text{g}/\text{cm}^2$).

B_{corr} - corrosion rate coefficient, which is a function of exposure temperature and relative humidity.

t - exposure duration (year).

Cl - total chloride content at the steel level (kg/m^3).

F_{Cl} , F_{galv} , F_{oxide} , and F_{oxy} - factors of chloride content, galvanic effects, continuous formation and aging of oxides, and availability of oxygen.

f_e - the factor that modifies ρ_0 based on the influence of exposure environment.

f_t - the factor that affects the resistivity test method.

t_p - equal to $t - t_i$, where t is the time to be predicted, and t_i is the time to initiate corrosion.

f - a slag correction factor, $f = 10^{(0.5-S|-0.5+S)}$.

Cl_{90} - 90-day chloride conductivity index value (mS/cm) (Streicher, 1995).

$\tau, \gamma, \eta, \kappa, \lambda, \nu, \varpi, \theta, \chi,$ and ζ - constants.

ρ - concrete resistivity.

ΔA_{SM} - cross section loss.

w_c - crack width.

CT - a parameter defined as a function of the concrete's tensile strength.

2.3.3 Numerical Models

To investigate the corrosion of steel reinforcement in concrete, various numerical models have been developed on the basis of the mathematical analysis of the electrochemical process of steel corrosion in concrete. Molina et al. (1993) developed a numerical model to simulate the cracking of RC specimens and characterize the mechanical aspects of this phenomenon by the use of several types of load and material models. The load was modeled by a combination of initial strains and change of elastic properties, simulating the expansion and softening of steel elements at the rebar surface due to corrosion. In a separate effort, Shafei et al. (2012 and 2013) established a rigorous finite-element (FE) model to characterize the corrosion process for RC structures. In this FE framework, several parameters were examined, such as chloride diffusion coefficient, ambient temperature, relative humidity, carbon dioxide, and extent of crack propagation. Also, several processes, such as heat transfer, moisture transport, wetting/drying, carbonation, and the ingress of chloride ions in concrete, were investigated. This framework predicted the chloride content at different depths of the RC component in different time steps. A series of non-Gaussian stochastic fields were also generated, allowing a statistical assessment of the probability of corrosion.

2.4 FACTORS AFFECTING THE CORROSION RATE

2.4.1 Bridge Structure Environment

The location of the bridge structure can influence the corrosion rate of steel embedded in concrete by several effects, such as temperature and relative humidity. In particular, the corrosion rate is affected by temperature directly, as the chemical reaction rate of the corrosion process is increased with increasing the ambient temperature. Živica et al. (1997) conducted an experimental study to investigate the factors affecting the corrosion rate and their sensitivity under chloride-induced corrosion. It was found that the ambient temperature significantly influenced the corrosion rate, but only up to 104 °F (40 °C).

In addition, relative humidity can influence the corrosion rate by introducing the moisture to the electrochemical reaction as well as changing the electrical resistivity of concrete. A numerical study was performed by Yu et al. (2017) with the objective of investigating the effects of temperature and relative humidity on the corrosion rate of steel in concrete. It was concluded that when the temperature increased from 50 °F (10 °C) to 122 °F (50 °C), the corrosion rate increased significantly. It was also found that the corrosion rate increases as the relative humidity increased from 55% to 95%.

2.4.2 Concrete Quality

The concrete quality, such as binder type (i.e., the use of supplementary cementitious materials (SCMs), such as fly ash, slag, and silica fume) and water-to-cement ratio, can significantly influence the corrosion rate. Due to the improved durability and reduced permeability of concrete, the incorporation of SCMs

can delay the corrosion initiation of embedded steel bars (Alexander and Magee, 1999; Yuan et al., 2009).

The corrosion rate of steel was also influenced by the water-to-cement ratio (w/c) primarily because of refining the pore structure of the concrete. Pettersson (1995) demonstrated that the corrosion rate increased by using a higher w/c ratio (due to the reduced resistivity of concrete as well as the increased permeability). According to the experimental test results reported by Mangat et al. (1994), the lowest corrosion rate of $0.13 \mu\text{A}/\text{cm}^2$ was found for the w/c ratio of 0.45, while the corrosion rate was $2.16 \mu\text{A}/\text{cm}^2$ with the w/c ratio of 0.76. Thus, the binder type and the w/c ratio were both found to significantly influence the corrosion rate.

2.4.3 Depth of Concrete Cover

Based on the prior studies, the depth of concrete cover may significantly affect the corrosion rate, and may substantially affect the cracking potential and the spalling of concrete due to corrosion (Alonso et al., 1988; Ahmad, 2003; Otieno et al., 2010). A thick cover, where the pores may be permanently saturated, can control the corrosion rate by limiting the access of oxygen (Alonso et al., 1988; Bentur, 1997; Otieno, 2014). It was also reported that the corrosion rate can be reduced as the depth of concrete cover increased from 20 mm to 40 mm (Scott, 2007). Recently, Lopez-Calvo et al. (2018) performed a study to evaluate the effect of concrete cover depth on the corrosion rate of steel in high-performance concrete. It was found that both the half-cell potential and linear polarization readings decreased with the increase of the concrete cover depth from 25 to 45 mm.

2.4.4 Extent of Exposure to Water and Deicing Salts

The extent of exposure to water and deicing salts directly influences chloride ion concentrations, which consequently influences the corrosion rate. It was found that increasing the chloride concentration can lead to an increase in the corrosion current density, reduce the pitting potential, and increase the electrolyte conductivity (Otieno, 2014). Based on the study conducted by Foley (1970), the maximum corrosion rate was recorded with a NaCl concentration of approximately 0.5M. The corrosion rate, however, dropped with the increase of chloride concentration above 0.5M. This can be due to oxygen depletion, which can reduce the cathodic reactions in the corrosion process.

2.5 FACTORS AFFECTING DELAMINATION

Delamination is defined as the failure of concrete surrounding reinforcing bars caused by the expansion of corrosive materials formed in the rebar. The following literature review describes some of the currently proposed mechanisms for delamination failure, factors that influence delamination, and models to estimate the amount of corrosion products throughout the delamination process.

A study conducted by Du et al. (2013) described the delamination mechanism failure of a simply supported beam in three stages: (1) internal cracking, (2) internal penetration, and (3) external cracking. This study assumed uniform corrosion throughout the beam. Du et al. (2013) stated that delamination begins with internal cracking, i.e., small cracks formed perpendicular to the length of the bar. The

internal penetration stage begins as these cracks grow, eventually forming large internal cracks between reinforcing bars. Depending on the dimensions of the structural element, this stage can happen concurrently or before the next stage of external cracking. Horizontal cracks are commonly formed as the internal cracks grow outward, eventually reaching the concrete surface. Vertical cracks can also form toward the bottom of the beam.

Zhang and Su (2019) describe a slightly different delamination mechanism, focusing on uneven corrosion. The cited study assumed that most of the corrosion products form at the bottom of the rebar, closest to the external surface. The three stages of delamination were expressed as: (1) the elastic stage of concrete, (2) partial cracking stage, and (3) the stage in which delamination occurs in the concrete cover. In the elastic stage, concrete acts elastically, bending before any cracks occur. The cracking stage occurs as corrosion products apply pressure to the concrete that surrounds the embedded bars. Overstress occurs when the tensile stress exerted from the corrosion products is equal to (or higher than) the concrete's tensile strength. Next, the partial cracking stage begins as the tensile stress exerted by the corrosion products increases with the continuation of corrosion, making the cracks grow until there is no tensile strength along the delamination plane. When tensile strength is exceeded along the delamination plane, the third and final stage is reached, which signifies the development of delamination. In the last stage, the corrosion-induced tensile stress across the reinforcement layer has exceeded the tensile strength, causing the concrete to break off from the delamination plane.

Many parameters influence the delamination process. Rebar spacing is an important parameter, causing a significant impact on the delamination process. Du et al. (2013) completed laboratory tests to study this parameter and found that it does not affect the internal cracking stage but has significant impact on the internal penetration stage. The ratio of bar clear distance, s , to concrete cover, c , was correlated to the radial expansion needed to cause delamination; decreasing the s/c ratio decreases the amount of radial expansion to cause failure, meaning that delamination occurs faster with a smaller s/c ratio. When the s/c ratio was less than 2.2, internal penetration took place without external cracking, i.e., the failure was not recognizable. The study recommended s/c ratios greater than 2.2, as internal penetration and external cracking took place simultaneously, allowing maintenance crews to see the signs of failure and schedule the required repairs accordingly. The reported results were confirmed in Zhang et al. (2017), which assumed nonuniform corrosion.

Du et al. (2013) found that changing the concrete cover, and therefore the s/c ratio, was less effective at preventing internal penetration than changing the bar spacing when the s/c ratio was less than 2.2. For beams with s/c ratios larger than 2.2, increasing the concrete cover increased the chance of delamination. The study also noted that a thinner concrete cover would allow chlorides to reach the embedded steel bars faster, causing corrosion to begin at an earlier time. Zhang et al. (2017) found that a thicker concrete cover leads to a higher internal pressure before external cracks occur. The FE model used in the cited study did not show a correlation between the increased concrete cover and improved durability. Bar diameter also showed minimum effects on the delamination process. Du et al. (2013) found that the bar diameter most significantly impacts the initial internal cracking and the creation of cracks perpendicular to the length of the bar, especially as the bar diameter increases.

Zhu et al. (2016) analyzed concrete beams in artificial corrosion environments for over 20 years, partially focusing on recommended crack widths for beam safety. The study cites DuraCrete's recommendation for corrosion-induced cracks to be a maximum of 0.3 mm for aesthetic reasons and 1.0 mm for the beginning of delamination. The beams in the study did not begin spalling until corrosion cracks were over 3.0 mm wide after 26 years. The study also found that deflection due to corrosion was not accurate enough to determine the service life of a RC structure, as the deflection did not always increase as the reinforcement corrosion continued.

Zhang et al. (2017) created a model for rebar corrosion loss after experiencing delamination. The model is as follows:

$$\eta = \frac{d_s + 4\delta_0 \frac{d_s}{0.155} + 3d_{sd}}{2nR_b} \quad (2.5)$$

where η is the rebar corrosion loss ratio, d_s is the distance that the rust front has traveled toward the nearest free edge, δ_0 is the effective thickness of the porous zone, d_{sd} is the distance that the rust front has traveled perpendicular to d_s , n is the corrosion expansion coefficient, and R_b is the initial diameter of the bar. This model was validated with an FE model and a parametric study.

Zhang and Su (2019) completed a series of analytical models to describe corrosion and cracking at various stages in the delamination process described previously. These models can be used to correlate the crack size or displacement to corrosion quantities. In the elastic stage, the net maximum thickness, $d_{f,max}$, and bulging of the concrete cover, $d_{cs,A}$, can be calculated by the equations below:

$$d_{cs,A} = \frac{2d_{f,max}D(D+2c)}{D^2(1-\nu)+(1+\nu)(D+2c)^2} \quad (2.6)$$

$$W_E = \frac{\pi}{2} \left[\frac{3+(D+d_{f,max})}{2} - \sqrt{\frac{D}{2} \left(\frac{D}{2} + d_{f,max} \right)} - \frac{\pi D}{2} \right] \quad (2.7)$$

$$W_{Ec} = \frac{\pi D \varepsilon_{ct}}{2} \quad (2.8)$$

where D is the initial rebar diameter, c is the concrete cover, ν is the Poisson's ratio, W_E is the concrete's elongation, W_{Ec} is the concrete's critical tensile deformation rate, and ε_{ct} is the concrete's tensile strain at the critical tensile deformation. In the partial cracking stage, the bulging of the concrete cover at its highest point, $d_{cs,A}$, can be calculated using the following equations:

$$d_{cs,A} = \frac{2d_{f,max}D(D+2c)(1-\rho)}{D^2(1-\nu)+(1+\nu)(D+2c)^2} + \rho d_{f,max} \quad (2.9)$$

$$\rho = \frac{d_{f,max} - d_{f,max,Ec}}{d_{f,max,u} - d_{f,max,Ec}} \quad (2.10)$$

where $d_{f,max,u}$ is the net maximum thickness of rust when the cover delamination initiates. Finally, the following equation can be used to find $d_{f,max,u}$.

$$d_{f,max,u} = \frac{S_b - \sqrt{3}D}{2\sqrt{3}L} w_c + W_{x,Ec} \quad (2.11)$$

$$W_{x,Ec} = \varepsilon_{ct} \left(c + \frac{D}{2} \right) \quad (2.12)$$

where S_b is the spacing between rebars, L is the length of the crack, and w_c is the crack tip opening displacement.

2.6 OVERALL ASSESSMENT

From the existing literature review, there is only one nondestructive testing method to directly measure the actual remaining area/section loss of reinforcing steel in concrete, i.e., X-ray with digital image processing. Although GPR has great potential for fulfilling this purpose, further research and development are still required to gain confidence in the use of GPR for section loss evaluation. Destructive methods provide more accurate assessments but at the detriment of the structure and at greater expense, access, and laboratory processing. Future section loss may be predicted based on the corrosion rate, potential, and current density measured from a few available commercial NDE devices. Similarly, rebar diameter/location can be measured by a few available commercial NDE devices, both in-situ and in the laboratory. For the purpose of this research project, the most relevant in-situ measurements can be concrete electrical resistivity, concrete strength, and cover depth, while 3D laser scanning and rebar tensile strength measurements can be promising in the laboratory. A number of corrosion rate models were identified in the literature for the initiation and propagation stages of reinforcement corrosion. The delamination process was also reviewed, although it is still in need of further research. The current models are well crafted, but still are not able to fully grasp all the physical aspects observed in reality, such as rust entering the porous areas around the steel, into the cracks, and eventually leaking out of the concrete. The next chapter will examine the models for the propagation stage and compare how they predict the reinforcement section loss over time.

CHAPTER 3: COMPARISON AND FORMULATION OF PREDICTIVE MODELS

This chapter presents an investigation of predictive models to estimate the corrosion rate for reinforcement section loss prediction and the corrosion-induced crack initiation and propagation in the concrete cover of RC structures. The numerical models of concrete cracking due to the corrosion of reinforcing steel are included to further elaborate on the initiation and propagation process.

To infer the extent of section loss, a model that aligns with the structure of interest must be selected, along with the consideration of influential parameters. Predictive models fall into two broad categories: (i) empirical models calibrated to experimental test and/or field data, and (ii) numerical models developed based on finite-difference and/or finite-element simulations. Predictive models often result in a corrosion rate estimate or a reinforcement loss estimate, in terms of mils lost. Predictive models are primarily used for the assessment of the time of corrosion initiation due to chloride ingress. After cracking and subsequent failure of the concrete cover, the rate of corrosion-induced structural deterioration increases. The models can use a variety of factors dealing with the original construction materials, as well as the exposure condition (See Table 3.1 for potential influencing factors).

Table 3.1. Main influential factors

Factors concerning original RC details:	
	Bar diameter
	Spacing
	Bundled bars
	Concrete cover
	Concrete strength
	Concrete resistivity
	Reinforcement protection system
Factors concerning environment:	
	chloride concentration
	leaking joints
	humidity levels
	temperature exposure
	sealers and treatments
	crack opening or frequency

Predictive models are useful for determining corrosion rate prior to concrete failure. If the corrosion rate prior to cover spalling is known, there may be some benefit to estimating further loss. This can be achieved through a set of predictive models. Specifically, when an inspector detects cracking, by evaluating the width of the crack, the steel loss or corrosion degree can be estimated.

3.1 EMPIRICAL MODELS FOR CORROSION RATE PREDICTION

In this section, seven empirical models (i.e., Alonso et al., 1988; Morinaga, 1990; Liu and Weyers, 1998; Vu and Stewart, 2000; Li, 2004 a,b; Pour-Ghaz et al., 2009) are formulated for predicting the corrosion rate of steel reinforcement embedded in RC structures. The identified models will be later calibrated with the data from corroded bars collected from the field. It is important to note that the reliability of these models can vary, as they take into consideration a range of input parameters that can have inherent variability in the field. For comparison purposes, the results extracted from these empirical models are presented in the following sections.

3.1.1 Alonso et al. (1988)

$$i_{corr} = \frac{k_{corr}}{\rho_{ef}} \quad (3.1)$$

where k_{corr} is a constant ($3 \times 10^4 \mu\text{A}/\text{cm}^2/\text{k}\Omega\text{-cm}$) and ρ_{ef} is the resistivity of concrete at its actual degree of saturation. This model was originally based on a statistical analysis of resistivity and accelerated carbonation-induced corrosion rate results. It was demonstrated that, in addition to the concrete resistivity, the presence of cracks and concrete cover depth can significantly affect the corrosion rate (Otieno et al., 2010). Figure 3.1 shows the data of concrete resistivity measured from Piers 12WB, 30EB, and 27EB.

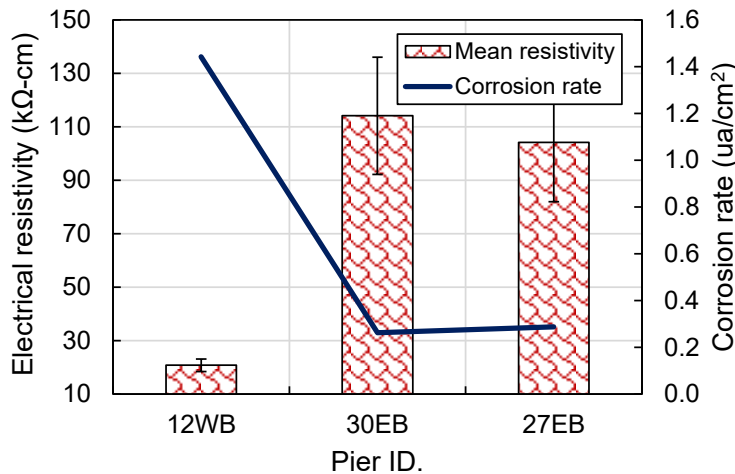


Figure 3.1. Concrete electrical resistivity and corrosion rate, following Alonso et al. (1988)

In addition to the measured currents, the corrosion rate was calculated based on Faraday's law, in terms of metal loss:

$$r = \frac{ia}{nFD} \quad (3.2)$$

where r represents the corrosion rate ($\mu\text{m}/\text{year}$); i is the corrosion current density (amp/cm^2 or $\text{coulombs}/\text{cm}^2\text{-sec}$); a is the atomic weight, 55.84 g for iron; n is the number of electrons exchanged, 2

for Fe^{2+} ; F is the Faraday's constant, 96,500 coulombs/mol; and D is the density of the metal, 7.87 g/cm³ for steel.

From the regular measurements of the corrosion current density, the corrosion rate is calculated for the bridge's service life. Figure 3.2 presents the predicted steel loss during the bridge's service life calculated based on Alonso et al. (1988).

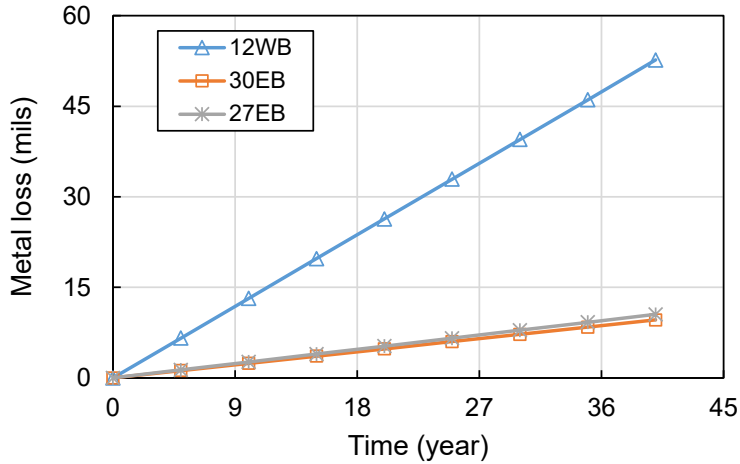


Figure 3.2. Predicted steel loss as a function of time, following Alonso et al. (1988)

3.1.2 Morinaga (1990)

$$i_{corr} = \frac{d_{st}}{d^2} (-0.51 - 7.60C_{Cl} + 44.97(w/b)^2 + 67.95C_{Cl}(w/b)^2) \quad (3.3)$$

where d_{st} is the diameter of the reinforcing steel (mm), which is 25.4 mm (#8 bar); d is the concrete cover (38.1 mm); C_{Cl} is the chloride content (% of NaCl by mass of mixing water), which is assumed 3%; and w/b is the water-to-binder ratio, which is assumed 0.45.

This model is developed based on chloride-induced corrosion and does not incorporate environmental parameters. Figure 3.3 presents the predicted steel loss as a function of time calculated based on Morinaga (1990).

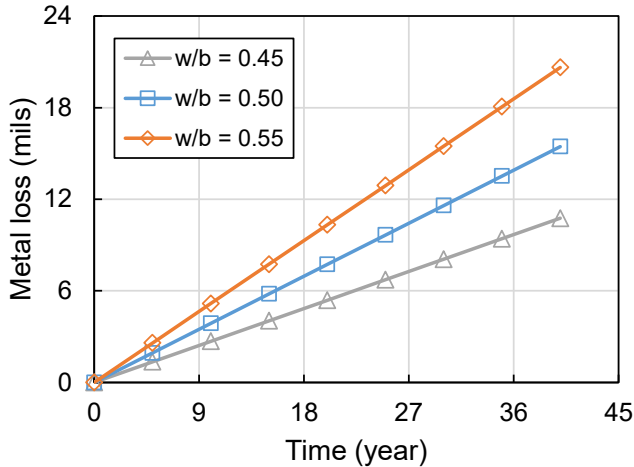


Figure 3.3. Predicted steel loss as a function of time, following Morinaga (1990)

Even though this model has been updated to include the environmental parameters, the parameters related to the concrete material properties, such as binder type, are still not considered. The updated model proposed by Morinaga (1990) has been expressed as follows:

$$q_{corr} = 2.59 - 0.05T - 6.89(h - 0.45) - 22.87C_{O_2}^{air} - 0.99C_{Cl} + 0.14(h - 0.45) + 0.51TC_{O_2}^{air} + 0.01TC_{Cl} + 60.81(h - 0.45)_{O_2}^{air} + 3.36(h - 0.45)C_{Cl} + 7.32_{O_2}^{air}C_{Cl} \quad (3.4)$$

where q_{corr} is the corrosion rate (10^{-4} g/cm² per year), which needs to be converted to $i_{corr} = 109.26q_{corr}$; T is the temperature (i.e., 0, 5, 10 and 20 °C); h indicates the relative humidity (70%); and $C_{O_2}^{air}$ is the concentration of O₂ in the air (0.21%).

Figure 3.4 presents the updated predictions, incorporating the environmental parameters, as a function of ambient temperature.

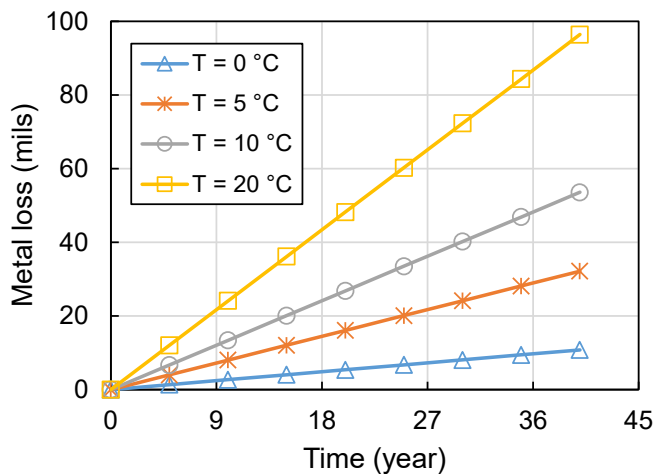


Figure 3.4. Predicted steel loss over time, including the environmental parameters, following the modified model provided by Morinaga (1990)

3.1.3 Liu and Weyers (1998)

$$i_{corr}(t) = 0.926 \times \exp \left[7.98 + 0.7771 \ln(1.69 Cl) - \frac{3006}{T} - 0.000116\rho + 2.24t^{-0.215} \right] \quad (3.5)$$

$$\rho = e^{8.03 - 0.549 \ln(1 + 1.69Cl)} \quad (3.6)$$

where Cl indicates the total chloride content at the steel level (0.2 kg/m^3). ACI 318-14 prescribes limits on the range of chloride concentration, which can vary from 0.05 to 0.10% of the weight of concrete. ρ is concrete resistivity and t is exposure duration (year). The cited range represents the typical threshold suggested for chloride concentration at the reinforcing bars when the corrosion initiation occurs.

This model is time-dependent and based on the statistical analyses of experimental results measured from a 5-year accelerated corrosion testing program. It must be noted that the corrosion rate is a function of the chloride content, temperature, resistivity of the concrete, and active corrosion time. Figure 3.5 presents the predicted steel loss over time calculated based on Liu and Weyers (1998).

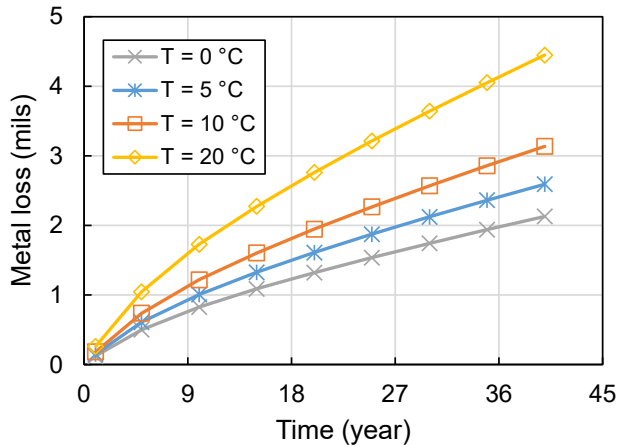


Figure 3.5. Predicted steel loss as a function of time, following Liu and Weyers (1998)

3.1.4 Vu and Stewart (2000)

Corrosion initiation:

$$i_{corr(1)} = \frac{37.8(1-w/b)^{-1.64}}{c} \quad (3.7)$$

Corrosion propagation:

$$i_{corr} = i_{corr(1)} 0.85 t_p^{-0.29} = \left(\frac{32.13(1-w/b)^{-1.64}}{c} \right) t_p^{-0.29} \quad (3.8)$$

where t_p is equal to $t - t_i$, where t is the time of interest and t_i is the time to initiate corrosion.

This model is time-dependent and assumes that the availability of oxygen at the steel surface is the governing factor to predict the corrosion rate. However, it does not consider the concrete quality aspect. The predicted corrosion rate and steel loss over time are shown in Figures 3.6 and 3.7.

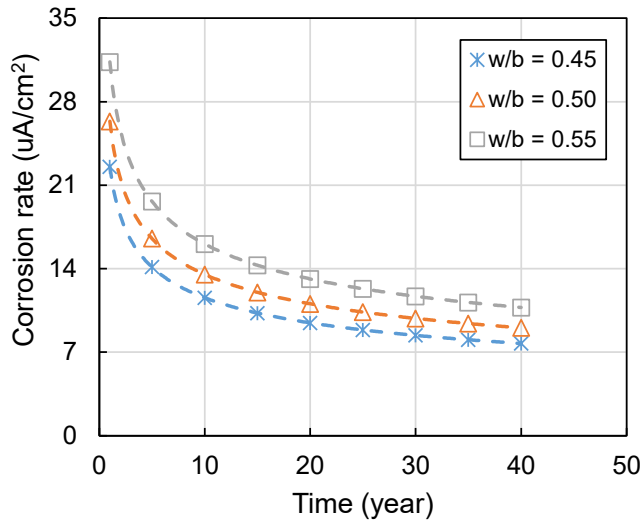


Figure 3.6. Predicted corrosion rate, following Vu and Stewart (2000)

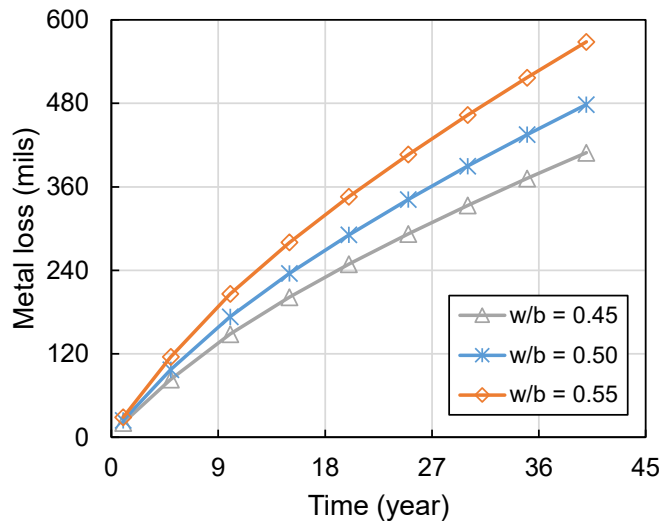


Figure 3.7. Predicted steel loss, following Vu and Stewart (2000)

3.1.5 Li (2004a)

$$i_{corr} = 0.3683 \ln(t) + 1.1305 \quad (3.9)$$

where t is time in years.

This model was proposed based on experimental test data, in which only the influence of corrosion duration was considered. Therefore, the model lacks a set of relevant parameters (e.g., concrete resistivity and chloride content) required to reflect the corrosion process of reinforcing bars. Figures 3.8

and 3.9 present the predicted corrosion rate and steel loss as a function of time calculated based on Li (2004a).

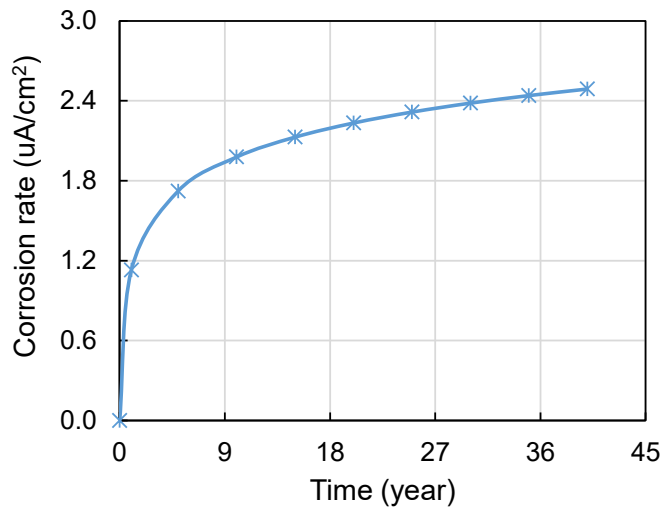


Figure 3.8. Predicted corrosion rate, following Li (2004a)

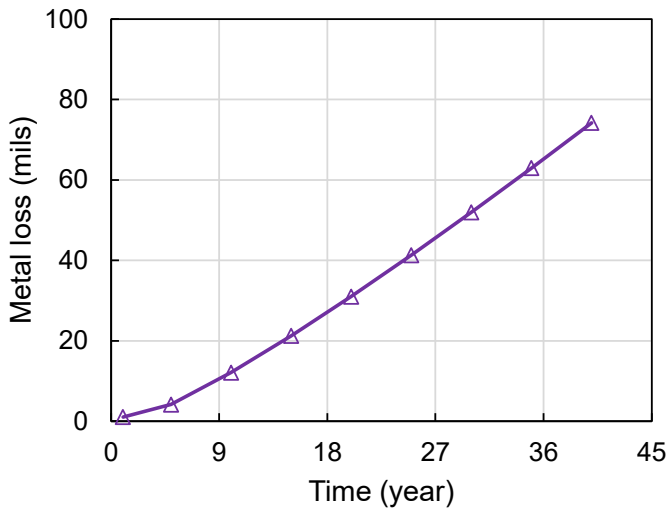


Figure 3.9. Predicted steel loss, following Li (2004a)

3.1.6 Li (2004b)

$$i_{corr} = 2.486 \left(\frac{RH}{45}\right)^{1.6072} \left(\frac{T}{10}\right)^{0.3879} \left(\frac{w/b}{0.35}\right)^{0.4447} \left(\frac{d_c}{10}\right)^{-0.2761} (k_{Cl})^{1.7376} \quad (3.10)$$

This model considers both internal (concrete cover, d_c , and w/b ratio) and external (relative humidity, RH , temperature, T , and chloride content, k_{Cl}) factors. However, this model does not consider the time-dependent corrosion rate.

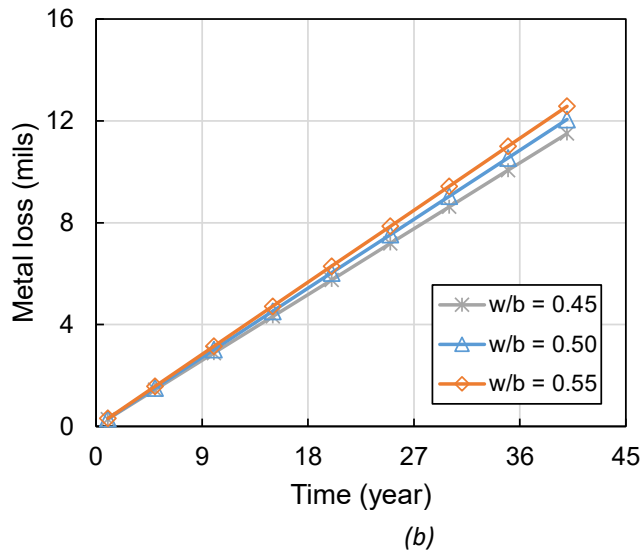
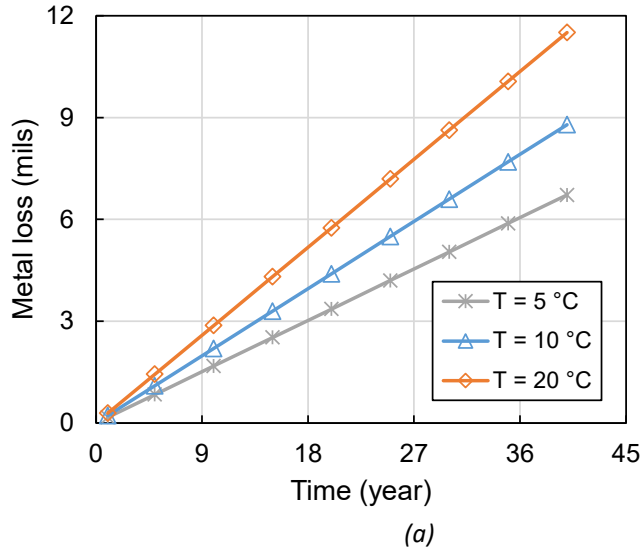


Figure 3.10. Predicted steel loss, following Li (2004b): (a) different temperatures with $w/b = 0.45$ and (b) different w/b with $T = 10^\circ\text{C}$

3.1.1.7 Pour-Ghaz et al. (2009)

$$i_{corr} = 100 \left\{ \frac{1}{\tau \rho^\gamma} \left[\eta T d^\kappa i_L^\lambda + \mu T \nu i_L^\omega + \theta (T i_L)^\theta + \chi \rho^\gamma + \zeta \right] \right\} \quad (3.11)$$

where i_{corr} represents the corrosion rate (mA/cm^2); T is the ambient temperature (ranging from 10°C to 60°C); $\tau, \gamma, \eta, \kappa, \lambda, \nu, \omega, \theta, \chi,$ and ζ are constants, summarized in Table 3.2, and ρ is the concrete resistivity.

Table 3.2. The constants in the model provided by Pour-Ghaz et al. (2009)

Constant	Value
τ	1.18E-03
η	1.41E-05
ζ	-0.221212
κ	0.0847693
λ	0.1300252
γ	0.8005059
μ	1.23E-11
θ	-0.000103
χ	0.4752581
ν	5.03E-07
ϖ	90487

The concrete resistivity under a specific ambient temperature (T) can be calculated by

$$\rho = \rho_0 e^{\frac{\Delta U_\rho}{R} \left(\frac{1}{T} - \frac{1}{T_0} \right)} \quad (3.12)$$

where

$$\Delta U_\rho = \frac{26.753349}{1 - 4.3362256 \times \exp(-5.2488S_r)} \quad (3.13)$$

where R is the universal gas constant, i.e., 8.314 J/(mole K); ρ_0 is the resistivity at the reference temperature, T_0 (K); ΔU_ρ (KJ/mole) is the activation energy of the Arrhenius relationship (Chrisp et al., 2001); and S_r is the degree of concrete saturation. If w/c is less than 0.4 and S_r is greater than 0.75, ρ is equal to 200 Ωm , but if w/c is less than 0.4 and S_r is less than 0.75, ρ is equal to 600 Ωm .

This model was established based on electrochemical theory. Due to the fact that the referenced model requires a large number of input parameters, each of which has significant variation, it was not considered further in the current study.

3.2 EMPIRICAL MODELS FOR PREDICTING STRUCTURAL DETERIORATION

While predictive corrosion rate models are useful for service life analyses, models that correlate section loss to a state of distress are equally helpful. The relationship between the concrete crack and corrosion products has been investigated by both accelerated and natural corrosion tests. The following models can establish the relationship between corrosion propagation and bar diameter loss.

3.2.1 Rodrigues et al. (1996)

$$w = 0.05 + \beta(x - x_{cr}) \quad (3.14)$$

where w is the cracking width; β is the coefficient depending on the position of the rebar, where $\beta = 0.01$ for top cast bars and $\beta = 0.0125$ for bottom cast bars; x is the corrosion penetration (in μm); and x_{cr} is the corrosion penetration after cover cracking (in μm) that can be obtained using $x_{cr} = 83.8 + 7.4 \frac{c}{d} - 22.6f_{ct}$, where c is the cover depth, d is the rebar diameter, and f_{ct} is the concrete's tensile strength.

3.2.2 Vidal et al. (2004)

Vidal et al. (2004)'s model is based on two naturally corroded RC beams, 14 and 17 years old. The model predicts the local cross-section loss of reinforcement from the crack width following two steps of the cracking process: crack initiation and crack propagation. The following equation relates the amount of corrosion to the width of concrete cover cracks.

$$w = 0.0575(\Delta A_{steel} - \Delta A_{steel,cr}) \quad (3.15)$$

where ΔA_{steel} is the part of rebar cross section consumed by corrosion (in mm^2), $\Delta A_{steel,cr}$ is the consumed part of rebar cross section (in mm^2) at cover cracking. The amount of rebar cross section consumed by corrosion is equal to $\Delta A_{steel} = 0.25\pi\alpha_v x(2d - \alpha_v x)$, where $\alpha_v (= 2)$ is the volumetric expansion ratio of corrosion products; x is the corrosion penetration (in μm); and d is the intact rebar radius (in mm). The Δ formula calculates the consumed part of rebar cross section at crack initiation: $A_{steel,cr} = A_s[1 - (1 - 0.001\alpha_v x_{cr}/d)^2]$, where A_s is the cross-sectional area of reinforcing steel (in mm^2).

3.2.3 Zhang et al. (2010)

$$w_c = 0.1916\Delta A_{SM} + 0.164 \quad (3.16)$$

where ΔA_{SM} is the cross-sectional loss and w_c is the crack width.

This model relates the crack width to the average cross-sectional loss of corroded reinforcement. Figure 3.11 shows the predictions for #6, #8, and #10 bars. As reflected in the referenced figure, the crack width prediction seems to be unrealistically high for the larger bar diameters. It is also important to note that this model does not consider the concrete characteristics, e.g., concrete tensile strength and porosity.

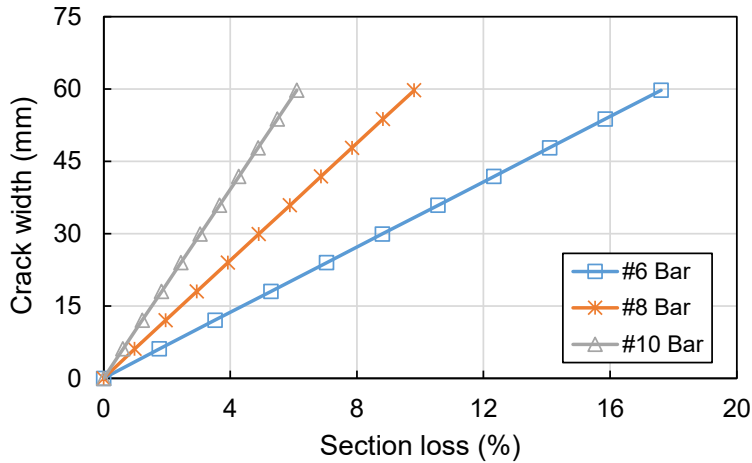


Figure 3.11. Predicted crack width for concrete with different rebar section losses, following Zhang et al. (2010)

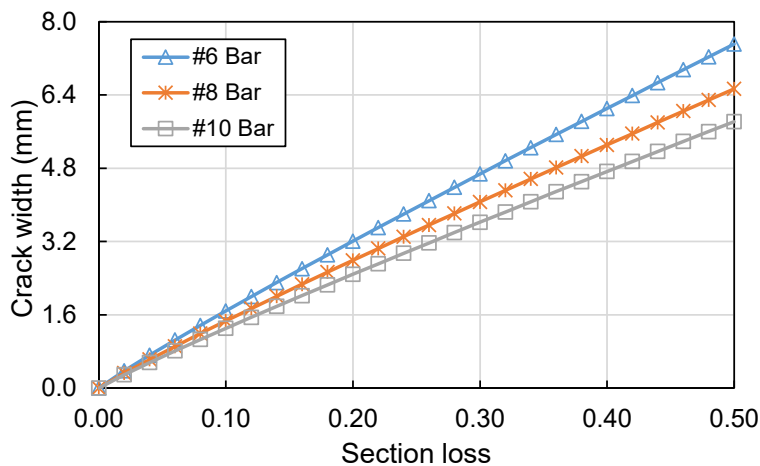
3.2.4 Andrade et al. (2015)

$$w_c = 15.683 \left(\frac{x_{ave}}{R_0} CT \right)^{0.928} \quad (3.17)$$

where ΔA_{SM} is the cross section loss; w_c is the crack width; and CT is a parameter defined by $CT =$

$\alpha_a \left(\frac{c_c}{\phi_0} \right)^{-\frac{\beta_a}{f_{ct}}}$, where f_{ct} is the tensile strength of concrete, C_c is the cover depth, ϕ_0 is the rebar radius, and α_a and β_a are the parameters from data fitting.

This model was proposed to investigate the relationship between the crack opening and the amount of corrosion in the reinforcing bars. Figure 3.12 shows the predicted crack width for concrete with respect to C_c/ϕ_0 and different rebar diameters, i.e., #6, #8, and #10 for a cover depth of 1.5 in (38.1 mm). This model is an improvement in the prediction of the relationship between the crack width and other contributing parameters.



The section loss axis represents the fraction of loss of the bar diameter.

Figure 3.12. Predicted crack width, as a function of bar diameter, following Andrade et al. (2015)

3.3 NUMERICAL MODELS FOR PREDICTING STRUCTURAL DETERIORATION

3.3.1 Qiao et al. (2016)

In the referenced study, an experimental program and corresponding FE modeling of a single rebar scenario were performed to investigate the effects of corrosion distribution, specifically nonuniform and localized corrosion, on crack propagation in concrete. The results demonstrated that the nonuniform corrosion degree, θ , can play a significant role in the surface cracking patterns. In particular, under the same section loss area (corrosion degree), when θ equals 180° , a surface crack can develop more rapidly than that for uniform corrosion ($\theta = 360^\circ$). The reason was found to be due to the change of the internal crack pattern. For example, the occurrence of the inclined lateral cracks would form more rapidly with $\theta = 45^\circ$ than that of $\theta = 180^\circ$ under the same section loss percentage.

3.3.2 Cheng et al. (2018)

In this study, a 2D FE analysis was performed to predict the concrete cover cracking due to reinforcement corrosion. The time-dependent nonuniform corrosion of multiple reinforcing bar scenarios was considered, focusing on adjacent rebars' influence on crack propagation. The results demonstrated that for the rebar spacing of 1.5 in (40 mm), only the internal cracks and side surface cracks occur. When the spacing increases to 2.3 in (60 mm) and 5.6 in (150 mm), the top surface cracks also occur and propagate toward the reinforcing bars. The reason was due to the rust expansion behavior, which deforms the surrounding concrete. However, if the rebar spacing is too close, the expansion stresses act as compressive stresses on the concrete surrounding the adjacent reinforcements, restraining the top concrete's surface deformation. In general, the results indicated that the crack width decreases with an increase in rebar spacing.

3.3.3 Castorena-González et al. (2020)

In this study, a 3D FE analysis was conducted using a corrosion damage model to assess the concrete cover's crack width. The literature test data, two corrosion tests performed in natural environments, and one performed in the laboratory test were used to validate the results. The relation between the crack width, which is after the crack appears on the surface, and the corrosion penetration depth was proposed as follows:

$$w^{0.08634} = \frac{(x_p^{0.20} + 1.3565)}{1.8673} \quad (3.18)$$

where w is the crack width (in mm) in the concrete cover and x_p is the penetration depth (in mm) for corrosion in the steel rebar after the first crack is formed (Figure 3.13).

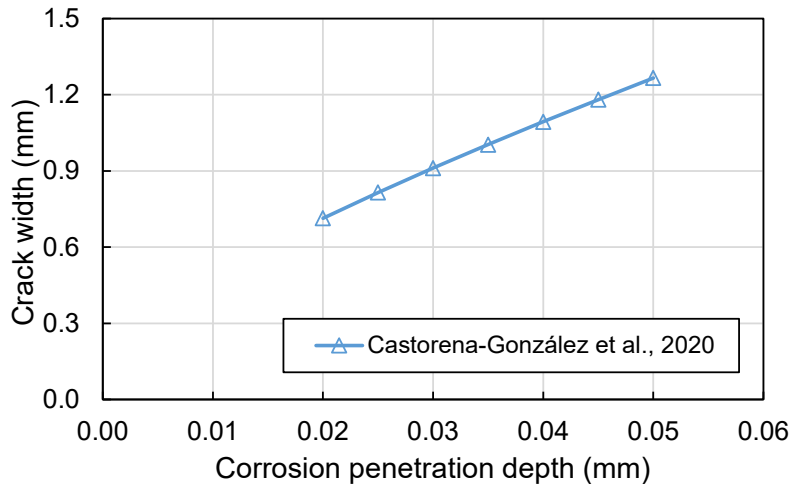


Figure 3.13. Crack width analysis as a function of x_p (steel corroded cross-section after surface cracking)

3.4 SUMMARY OF MODELING APPROACHES

The models included in this chapter represent a variety of predictive models developed and used for corrosion-related studies. These models may be based on empirical equations or numerical simulations. Predictive models may also be based on theoretical properties or based on actual measurements. There may be one model that shows a strong correlation for smaller diameter rebar and concrete cover less than 1 inch while others are more suited to larger diameter bars. Comparisons with the field data are expected to enable observations toward selection of models for best results in the typical reinforcing, concrete cover, and concrete properties common to MnDOT substructure inventory.

After careful consideration, the numerical models were decided to be discarded. This decision was based on a set of finite-element simulations, which reflected (1) strong dependency of the simulation results to a wide range of initial physical and modeling assumptions, many of which are not fully known, and (2) excessive computational time/demand required when the scope of modeling is extended from individual bars embedded in concrete to a complete RC bridge element. The computational limitations can be further realized when the aim is to accurately capture cracking, delamination, and spalling. Thus, it was decided to proceed with a subset of relevant empirical models. As discussed in Chapter 6, the selected empirical models have been further evaluated and calibrated based on the section loss data obtained from the bars collected from the field. This was to ensure that site-specific material and environmental parameters are properly taken into consideration.

CHAPTER 4: FIELD INVESTIGATION PRIOR TO REPAIR

4.1 BRIDGE DETAILS

Bridge 27831 serves eastbound and westbound traffic via I-394 in Minneapolis, MN, as shown in Figure 4.1. The bridge is divided into eastbound (EB) and westbound (WB) sections. Piers 1 through 29 consist of cast-in-place steel pile bents with reinforced concrete caps, and Piers 30 through 49 are reinforced concrete caps on reinforced concrete columns. The referenced bridge was inspected in 2018 by Collins Engineers in preparation for a 2020 bridge repair contract. The Collins Engineers’ inspector’s hammer sounded most of the concrete faces and used marking paints to identify unsound or spalled concrete. These defects were transferred to “sounding maps” for each pier and each face, which were in turn given to a bridge engineer to analyze further. There are multiple purposes to such a sounding map and structural analysis:

- To determine if the conditions would warrant bridge shoring during repair
- To assess if additional reinforcement would be required as part of repair
- To determine if supplemental strengthening would be necessary due to reinforcement section loss or the loss of the pier cap capacity.



Figure 4.1. Location of Bridge 27831 (highlighted area)

In addition to the sounding maps, pictures were provided by the inspectors, showing the delaminated areas and causal sources of deterioration—in most cases, leaking joints and drainage systems. From the collected data, the bridge engineer is often faced with estimating reinforcement section loss to assume in their pier cap capacity calculation. In some cases, the estimation of repair area and rebar

deterioration leads the bridge engineer to abandon the original flexural and shear capacity of the pier cap and to fill in the space between columns and outside columns with an infill wall. This is a common strategy where the pier’s remaining structural capacity is not well defined or where the concrete repair’s durability would be questionable. Infill walls provide direct bearing to footings and take away the beam action of the original pier cap. This, however, causes additional dead load applied to the foundation, which must be considered.

In this chapter, the pictures and sounding maps from 2018 are provided to illustrate the challenge of estimating section loss with limited information. In fact, the information gathered by Collins Engineers in their project was much more than traditionally obtained ahead of repair contract. From limited information, rebar section loss estimates are often provided only based on engineering judgment. These estimates are later subject to verification for giving them a degree of accuracy. After all, an estimate is only worthwhile when quality control is employed to improve later estimates.

In the bridge under consideration, the piers have been numbered west to east and named by the pier number followed by EB or WB, designating which side of the bridge it serves. Table 4.1 is a summary of piers selected by the MnDOT for investigation through this research project. Photos of the piers as of June–August 2020 are in the appendix, as well as the pier maps, providing a close look at each of the deteriorated areas on the piers.

Table 4.1. Piers studied in this research project

Pier 12EB	Pier 21EB
Pier 46WB	Pier 48EB
Pier 15EB (Bridge 27831A)	

The original bridge plans were issued in August 1967, and the bridge substructures were designed prior to the release of ASTM A615 specifications. Accordingly, the plans state that the reinforcement design used an allowable stress of 20,000 psi for intermediate grade reinforcement (See Figure 4.2). This allowable stress translates to a 40 ksi yield strength. However, it should be noted that the minimum yield strength assumed for design is often exceeded by the actual reinforcing materials provided.

DESIGN DATA
1965 A.A.S.H.O. DESIGN SPECIFICATIONS
DESIGN LOADING HS 20 AND ALTERNATE
LOADING DESIGNATED IN PPM 20-4
SECTION 4C

$f_c = 1,600$ P.S.I. $n = 8$
 $f_s = 20,000$ P.S.I. INTERMEDIATE GRADE REINFORCEMENT
 $f_s = 20,000$ P.S.I. STRUCTURAL STEEL - M.H.D. 3306
DECK AREA = 178,274 SQ. FT.

Figure 4.2. Design information from 1967 plans for Bridge No. 27831

4.2 PIER MAPS

In this section, the pictures taken from both the 2018 and 2020 inspections were analyzed to obtain the latest condition of the bridge piers before repair. The delaminated locations were indicated with hatching areas.

4.2.1 Pier 12WB

Figure 4.3 presents the delamination map produced in 2018. Face bars are smaller diameter and have a smaller concrete cover. Pitting may also be present in localized areas in the vertical rebars located near the front face of the pier cap. Deterioration is estimated to be from 5% to 10% where concrete did not spall, while up to 75% where spalls were observed. The section loss of the longitudinal steel bars embedded deeper into the pier cap is estimated to be from 5% to 10% where no concrete spalling was noted.

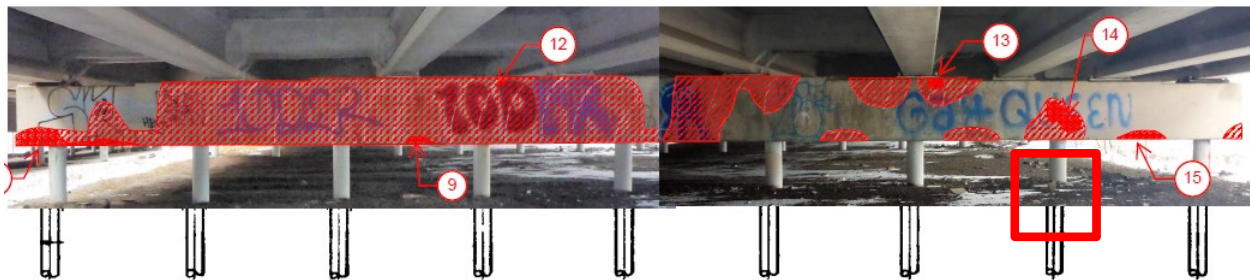


Figure 4.3. Pier 12WB mapping diagrams (photo taken in 2018)

Location 14 is presented as an example site, with a detailed image shown in Figure 4.4. The hammer sounding reveals a spall in the upper right and shallower delamination in the bottom of the pier cap. Based on the obtained data, it is estimated that the #5 vertical stirrups witness a section loss between 10% in the spalled, dark red area and a section loss as low as 5% in the delaminated, diagonally hatched area. Longitudinal reinforcement is of a larger diameter and buried deeper into the pier cap. As a result, the longitudinal reinforcement is estimated to have a relatively low section loss of 5% (or less) in the absence of concrete spalling. Large diameter bars produce much higher volumes of corrosion byproducts for the same section loss compared to small diameter bars. Consequently, concrete

delamination would be realized when large reinforcement bars have relatively low section loss. Very limited stirrup exposure is observed, but delamination extends from discrete spalls laterally, as if a form tie had acted as a corrosion initiator with leaking water from joints. Reinforcement may have some pitting section loss, but low general section loss is noted.



Figure 4.4. Location 14 of Pier 12WB

Figures 4.5 and 4.6, taken prior to repair in 2020, present the pier maps, detailing cracks, spalls, delamination, and locations of unsound concrete. Tables 4.2 and 4.3 document the detailing descriptions of selected locations.



Figure 4.5. East face of Pier 12WB (photo taken in 2020)

Table 4.2. Notes and description with locations identified in Figure 4.5

Location	Description of locations during repair
①	Repair excavation stopped before reinforcement.
②	Repair excavation in this area with exposed stirrups extending to the top of the pier.
③	Minor corrosion on exposed stirrups.
④	Repair excavation with exposed stirrups and spalling towards the top of the pier. Minor staining.
⑤	Repair excavation area ranging from top to bottom of the pier. Some exposed stirrups with minor corrosion.
⑥	Repair excavation towards the top of the pier cap. Some exposed stirrups with minor corrosion.
⑦	Repair excavation with no exposed rebar.
⑧	Repair excavation exposing longitudinal bars with minor corrosion extending underneath the pier.
⑨	Repair excavation and exposed longitudinal bars with minor corrosion.
⑩	Repair excavation on the south end of the pier extending underneath the pier. Some exposed longitudinal and stirrup rebar with minor corrosion.

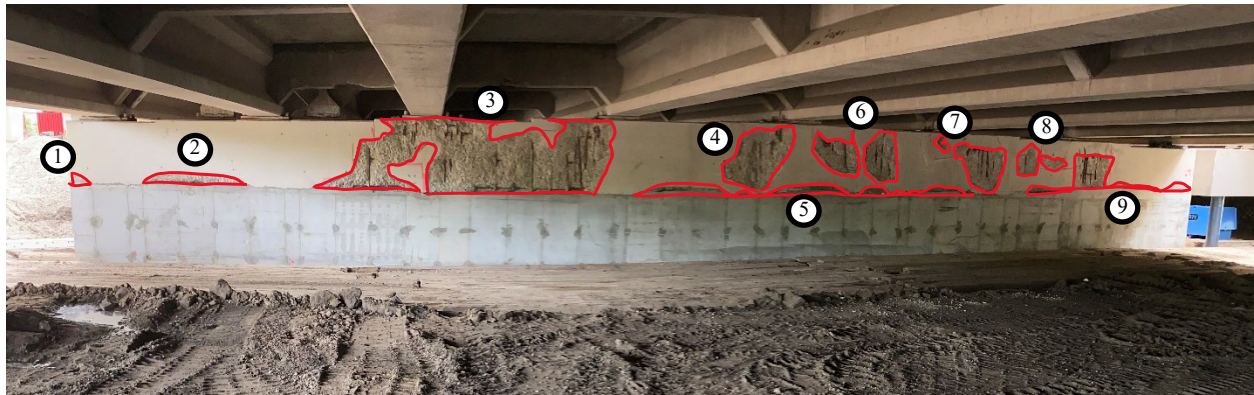


Figure 4.6. West face of Pier 12WB (photo taken in 2020)

Table 4.3. Notes and description with locations identified in Figure 4.6

Location	Description
①	Minor repair excavation on bottom corner of south edge on the west face.
②	Repair excavation on the bottom of the pier. One exposed longitudinal rebar with minor corrosion.
③	Most extensive area of repair excavation on the west face of the pier. Some exposed longitudinal and stirrup rebar with mild corrosion.
④	Repair excavation similar in extent to areas 3, 6, and 7. Some exposed stirrups with minor corrosion.
⑤	Continuous repair excavation along the bottom edge of the pier. Some exposed rebar with minor corrosion.
⑥	Repair excavation similar in extent to areas 3, 4, and 7. Exposed stirrups with minor corrosion.
⑦	Repair excavation. Some exposed stirrups with minor corrosion.
⑧	Minor repair excavation. One exposed stirrup with no corrosion.
⑨	Extended area of repair excavation on the bottom edge of the pier extending to the north end. One larger area of repair excavation with exposed stirrups and longitudinal bars showing minor corrosion.

4.2.2 Pier 21EB

Figure 4.7 presents the delamination map of Pier 21EB prepared in 2018. Pitting could be present in localized areas in the vertical rebars located near the front face of the pier cap. Reinforcement section loss estimated by engineering judgement is between 5% and 20%. The section loss of the longitudinal steel bars embedded deeper into the pier cap is estimated to be from 0% to 10% where no concrete spalling was noted.

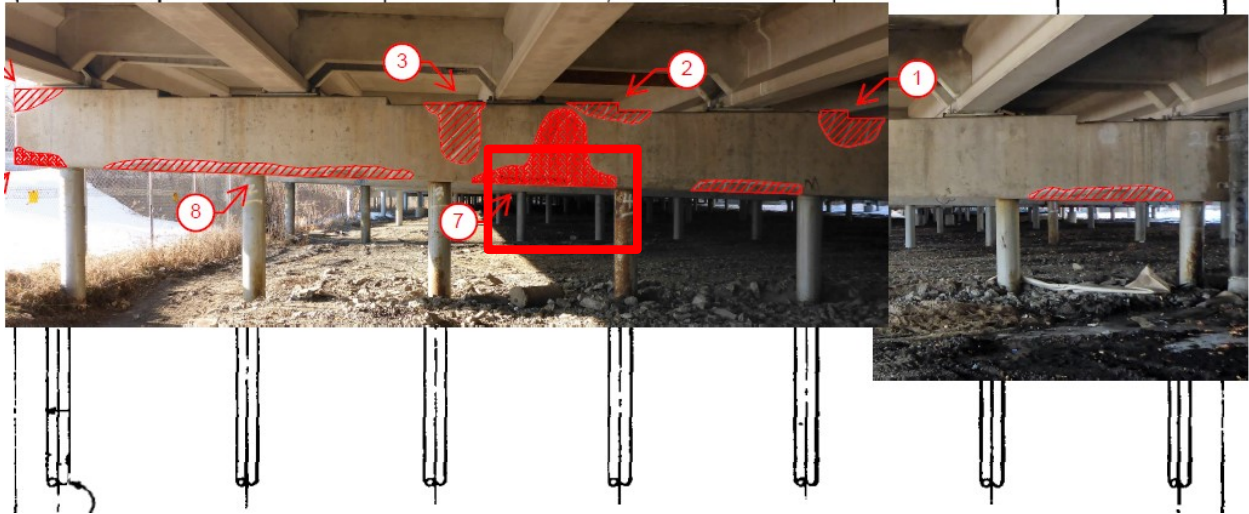


Figure 4.7. Pier 21EB mapping diagrams (east face, photo taken in 2018)

A zoomed-in picture of Location 7 is used as an example site, as shown in Figure 4.8. In the area diagonally hatched, the #5 vertical stirrups section loss is estimated to be from 10% to 20%. The larger, deeper longitudinal reinforcement in the spall area is estimated to have a section loss from 5% to 20%, due to the extent of concrete spalling.



Figure 4.8. Location 7 of Pier 21EB

Figures 4.9 and 4.10, taken prior to repair in 2020, present the pier maps, detailing cracks, spalls, delamination, and locations of unsound concrete. Tables 4.4 and 4.5 provide detailed descriptions of selected locations.



Figure 4.9. East face of Pier 21EB (photo taken in 2020)

Table 4.4. Notes and description with locations identified in Figure 4.9

Location	Description
①	Spalling along top edge of the pier on the east face.
②	Spalling exposing stirrups with mild corrosion.
③	Delamination on the upper portion of the pier on the east face.



Figure 4.10. West face of Pier 21EB (photo taken in 2020)

Table 4.5. Notes and description with locations identified in Figure 4.10

Location	Description
①	Delamination correlating with area 3 on the east face diagram.
②	Spalling extending from the base of the pier to nearly the top. Some exposed stirrups with minor corrosion.
③	Delamination correlating with area 1 on the east face diagram.
④	Delamination at the top of the pier.
⑤	Delamination on the bottom edge of the pier towards the north side, no exposed rebar.

4.2.3 Pier 46WB

Figure 4.11 presents the delamination map of Pier 46WB prepared in 2018. Section loss of vertical rebar is estimated to be from 5% to 10%. The section loss of the longitudinal steel bars embedded deeper into the pier cap and pier columns is estimated to be from 0% to 10%, as no concrete spalling is noted.



Figure 4.11. Pier 46WB mapping diagrams (east face, photo taken in 2018)

Figure 4.12 shows a zoomed-in picture of Location 9 as an example site. It is believed that the #3 column confinement hoop witnesses a section loss of 25% (or less) in the diagonally hatched area. There is no spalling observed, but general delamination is present. Because the hoop bars are small-diameter #3 bars, a greater percentage of the bar area in mass loss would be needed than for larger-face bars in order to get sufficient pressure to delaminate the concrete. The larger, deeper vertical reinforcement is estimated to have a relatively low section loss of 3% (or less) in the absence of concrete spalling, which would be more likely in larger-size bars, which experience a higher accumulation of corrosion products.



Figure 4.12. Location 9 of Pier 46WB

4.2.4 Pier 48EB

Figure 4.13 presents the delamination map of Pier 48EB prepared in 2018. Section loss of vertical rebar is estimated to be from 5% to 10%. The section loss of the longitudinal steel bars embedded deeper into the pier cap is estimated to be between 0% and 5% based on engineering judgement, as no concrete spalling was noted.



Figure 4.13. Pier 48EB mapping diagrams (east face, photo taken in 2018)

A zoomed-in picture of Location 8 is used as an example site, as shown in Figure 4.14. It is estimated that the #5 vertical stirrups witness a section loss as low as 5% in the diagonally hatched area. The larger, deeper longitudinal reinforcement is estimated to have a relatively low section loss of 5% (or less) because the delamination area shown is not overly large and large-size radius bars have a relatively low section loss. Longitudinal bar corrosion products cause greater longitudinal strips of delamination areas when corrosion is significant.

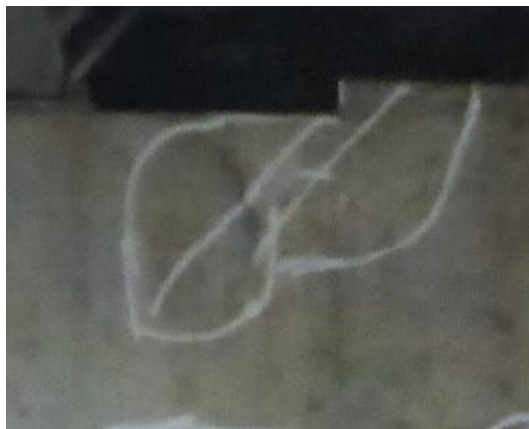


Figure 4.14. Location 8 of Pier 48EB

Figures 4.15 and 4.16, taken prior to repair in 2020, present the pier maps, detailing cracks, spalls, delamination, and locations of unsound concrete. Tables 4.6 and 4.7 document detailed descriptions of selected locations.



Figure 4.15. East face of Pier 48EB (photo taken in 2020)

Table 4.6. Notes and description with locations identified in Figure 4.15

Location	Description
①	Repair excavation to several inches below the exposed steel. Some exposed longitudinal and stirrup rebar with minor to mild corrosion.
②	Rust stains
③	Mild delamination on the bottom edge of the pier between columns 1 and 2. No corrosion present.
④	Repair excavation on the bottom edge of the pier close to column 2. Some exposed rebar with minor to mild corrosion.
⑤	Repair excavation on the top of the pier above column 2. Some exposed rebar with moderate corrosion.
⑥	Repair excavation on the bottom edge of the pier between columns 2 and 3. Some exposed longitudinal bars and stirrups with mild to moderate corrosion.
⑦	Repair excavation with no exposed rebar next to column 3.
⑧	Repair excavation on the top edge of the pier, reaching over to the west side. Some exposed bars with mild to moderate corrosion.



Figure 4.16. West face of Pier 48EB (photo taken in 2020)

Table 4.7. Notes and description with locations identified in Figure 4.16

Location	Description
①	Repair excavation extending from area 8 on the east face diagram. Some exposed bars with mild corrosion.
②	Repair excavation spanning most of the pier. Repair excavation extends to column 2. Some exposed bars with mild to moderate corrosion.
③	Repair excavation extending from area 3 on the east face diagram.
④	Repair excavation extending from column 1 to the north end of the pier. Some exposed rebar with mild to severe corrosion.

4.2.5 Pier 15EB

Figure 4.17 presents the delamination map of Pier 15EB prepared in 2018. Approximate vertical bar deterioration is estimated to be up to 90% because the entire face has delaminated within the hatched region (left end of figure, as shown in Figure 4.18). The section loss of the longitudinal steel bars embedded further deep into the pier cap is estimated to be between 0% and 10% because there are no outward spalls.



Figure 4.17. Pier 15EB mapping diagrams (west face, photo taken in 2018)



Figure 4.18. Very thin bars between Beams 7 and 8 in Pier 15EB

A zoomed-in picture of Location 5 is used as an example site, as shown in Figure 4.19. It is estimated that the #5 vertical stirrups witness a section loss of 15% in the spalled, dark red area and section loss as low as 10% in the diagonally hatched area. The larger, deeper longitudinal reinforcement is estimated to have a relatively low section loss of 5% (or less) in the absence of concrete spalling, which would be more likely with the corrosion products of large-size bars.



Figure 4.19. Location 5 of Pier 15EB

Figures 4.20 and 4.21, taken prior to repair in 2020, present the pier maps, detailing cracks, spalls, delamination, and locations of unsound concrete. Tables 4.8 and 4.9 document detailed descriptions of selected locations.



Figure 4.20. East face of Pier 15EB (photo taken in 2020)

Table 4.8. Notes and description with locations identified in Figure 4.19

Location	Description
①	Delamination with no exposed rebar next to pile 1.
②	Minor spalling on the bottom edge of the pier between piles 1 and 2. No exposed rebar.
③	Minor spalling on the bottom edge of the pier between piles 2 and 3. No exposed rebar.
④	Repair excavation between piles 3 and 4 extending up from the bottom edge. Some exposed longitudinal and stirrup rebar with minor corrosion.
⑤	Repair excavation at the top of the pier above pile 4. One exposed stirrup with minor corrosion.
⑥	Repair excavation above pile 5 exposing longitudinal and stirrup bars with moderate corrosion. Concrete is removed by a couple inches from the rebars.
⑦	Repair excavation on top of the pier between piles 6 and 7 exposing longitudinal and stirrup bars with moderate corrosion.
⑧	Repair excavation on the south end of the pier is spalled off, exposing the longitudinal bar. Mild corrosion present.



Figure 4.21. West face of Pier 15EB (photo taken in 2020)

Table 4.9. Notes and description with locations identified in Figure 4.20

Location	Description
①	Repair excavation extending from areas 7 and 8 from the east face diagram. Some exposed longitudinal and stirrups with corrosion ranging from mild to moderate.
②	Delamination on top edge of the pier extending from area 6 from the east face diagram. No exposed rebar on this side.
③	Repair excavation extending from the bottom towards to the top. Some exposed stirrups and longitudinal bars between piles 3 and 4 with minor corrosion.
④	Repair excavation underneath the pier extending from area 3 from the east face diagram. Some exposed longitudinal and corrosion bars with moderate corrosion of.
⑤	Repair excavation between piles 2 and 3. No exposed rebar.
⑥	Repair excavation between piles 1 and 2. Some exposed rebar with mild corrosion.

4.3 REBAR SAMPLE COLLECTION AND VISUAL ASSESSMENTS

Stirrup bars from the identified pier caps generally consist of #5 reinforcing bars. Longitudinal reinforcement typical of these pier caps ranged between #8 rebar and #11 reinforcement. Column spirals of this era consisted of #3 reinforcement or smooth bar, with #8 to #10 vertical reinforcement.

Visual assessment is the most common and convenient way to estimate reinforcement section loss because direct measurement is difficult with pitting, and caliper measurement is subject to limitations with rebar exposure and a limited number of measurement points. On the other hand, visual assessment is believed to be the least accurate means of measurement because it is very subjective and depends on both the judgment experience and the quality of observation. To generalize the section loss, a survey using photographs was circulated to MnDOT engineers for visual assessment. This was done in lieu of a site visit due to COVID restrictions in place at this time. Tables 4.10 and 4.11 summarize the

survey results received from two participants based on their review of the delamination survey and pier cap photos prior to repair, as well as knowledge of pier cap reinforcing configuration. The engineers did not have direct data on concrete cover thickness.

Table 4.10. Survey results of general steel section loss based on visual assessment

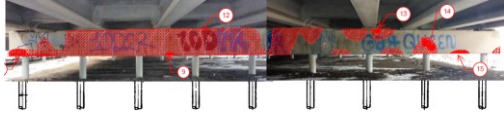
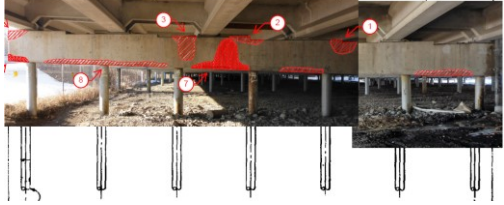
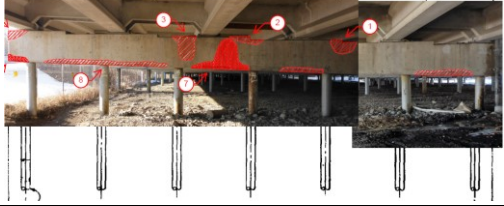





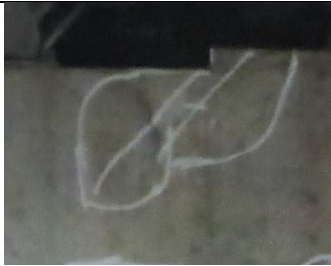

Pier ID.	Photo	Face bar section loss			Longitudinal bar section loss
		Engineer 1	Engineer 2	Engineer 1	Engineer 2
Pier 12EB		10-75%	5-25%	5-20%	5-10%
Pier 21EB		20%	5-10%	5-10%	5-20%
Pier 46WB		NA	5-10%	NA	5-10%
Pier 48EB		NA	5-10%	NA	5-10%
Pier 15EB		NA	5-90%	NA	5-10%

Table 4.11. Survey results of local steel section loss based on visual assessment

Pier ID.	Photo	Vertical stirrups section loss		Deep longitudinal bar section loss	
		Engineer 1	Engineer 2	Engineer 1	Engineer 2
Location 14 of Pier 12EB		5%	10%	0%	5%
Location 7 of Pier 21EB		20%	10%	5-10%	20%
Location 8 of Pier 46WB		25%	5%	<5%	<5%
Location 8 of Pier 48EB		5%	8%	<5%	5%
Location 5 of Pier 15EB		5%	15%	0%	5%

In addition to general assessments based on photos, individual reinforcement samples were obtained for laboratory measurements. The collected bars were labeled, and a visual assessment of sample section loss was performed by a MnDOT engineer. The reinforcement samples showed various states of corrosion and were primarily representatives of shear stirrups, which were nearest to the faces of pier caps. The purpose of this visual assessment was to form a basis for the visual assessment method and later compare it to more accurate methods. The samples were mostly obtained from rebar stirrup

locations, which are often the first points of corrosion due to leaking expansion joints. The samples and visual assessment photos are provided in Figure 4.22.



(a) S1 sample, #5 bar (5% section loss)



(b) S2 sample, #5 bar (75% section loss)



(c) S3 sample, #5 bar (90%-100% section loss)



(d) S4 sample, #5 bar (30% section loss)



(e) S5 sample, #5 bar (5% section loss)



(f) S6 sample, #5 bar (15% total section loss, 90% pitted end)



(g) S7 sample, #5 bar (5% section loss)



(h) S8 sample, #5 bar (50%-75% section loss)



(i) S9 sample, #6 bar (10% section loss for the straight portion, 100% near the bend diameter)



(j) S10 sample, #11 bar, taken from P46WB, west face, south overhang

Figure 4.22. Rebar samples extracted from the studied piers

CHAPTER 5: SAMPLE COLLECTION AND LABORATORY TESTS

A substructure repair contract for Bridge 27831 was initiated between MnDOT and a contractor in 2019. Upon the initiation of repair activities in the field, the research team coordinated with field inspectors and collected samples of corroded steel bars from the bridge piers for a direct assessment of the extent of corrosion and quantification of cross-sectional loss. Photographs of the exposed rebar conditions after excavations to sound concrete were obtained to document general reinforcement corrosion conditions. Laboratory tests and measurements were performed on corroded rebar samples to measure their tensile capacity and elongation characteristics.

5.1 SAMPLE COLLECTION

To assess the section loss due to corrosion and evaluate the remaining tensile capacity, nine rebar samples were extracted from the piers selected for this project (Table 5.1). As shown in this table, the section loss assessment was conducted initially by visual observation. It should be noted that these visual section loss assessments were estimated at the steel's worst spot right after the extraction. After the samples were delivered to the lab, the rebar rust was removed using a high-pressure wire brush. Their largest remaining diameters and weights were then measured using a caliper and a scale, respectively. Photos of the reinforcement bars after cleaning the corrosion products are presented in Figure 4.22.

Table 5.1. Rebar sample information

Rebar ID	Nominal diameter	Location description	Visual loss assessment	Measured diameter (in.)	Weight (lb.)	Length (in.)
S1	#5	P21WB, pier wall, south side	5% section loss	0.625	1.3510	19.0
S2	#5	P46WB, pier cap, west face, south overhang	75% section loss	0.625	1.2750	27.3
S3	#5	P46WB, pier cap, west face, south overhang	90-100% section loss	0.603	0.7360	18.4
S4	#5	P12WB, pier cap, south side	30% section loss	0.597	1.4900	22.6
S5	#5	P21WB, pier wall, south side	5% section loss	0.617	1.2031	17.0
S6	#5	P46WB, pier cap, west face, south overhang	15% total section loss, 90% pitted end	0.579	1.7265	24.1
S7	#5	P12WB, pier cap, south side	5% section loss	0.602	1.7475	23.8
S8	#5	P46WB, pier cap, west face, south overhang	50-75% section loss	0.603	1.9075	29.0
S9	#6	Bridge 27831A – P15A, pier cap, east face	10% section loss for the straight portion, 100% near the bend diameter	0.750	2.8235	33.5 (straight) + 13.5 (bend)
S10	#11	P46WB, pier cap, west face, south overhang	5-10% section loss	1.410	22.7050	64.0

5.2 SECTION LOSS MEASUREMENT

5.2.1 3D Scanning

In this project, the remaining section of the extracted bars was measured using the 3D scanning technique. Figure 5.1 shows the 3D laser scanner used in this project. The scanning speed was 37 mm/s, and the positioning accuracy was 0.02 mm. Upon completing the laser scanning, the 3D coordinates of each point of the corroded steel bars were first obtained, generating a point cloud file by the scanning

system software. These points were then connected and formed a very fine mesh of triangular surface polygons, the number of which in each scanning was between 200,000 and 400,000 elements, depending on the geometry complexity.



Figure 5.1. 3D laser scanner

Figure 5.2 shows a representative specimen, S1, along with its 3D scan. As can be seen, the high resolution of the surface mesh allows a detailed description of the rebar's geometry, including length, ribs, pit distribution, and loss of cross-sectional area along the bar's length.



(a)



(b)

Figure 5.2. 3D scanning for S1 sample: (a) before scanning, and (b) after scanning

A solid model of corroded steel bars was established after the 3D scanning. Reverse engineering software (Geomagic) was used to treat the scanned data, such as polygon spikes removing and mesh holes closing due to the natural characteristics of scanning, as shown in Figure 5.3.



Figure 5.3. Scanned rebar model treatment: (a) original model obtained from the 3D scanning; and (b) model treated using Geomagic software

After obtaining and treating the 3D scanned rebar models, the corrosion level was determined based on the scanning measurements. A complete description of the steps taken, beginning from the initial 3D mesh to the graph showing the cross-sectional variation, is provided below:

- Step 1: The scanned bar geometry was post processed, cleaned, and repaired, as shown in Figure 5.3.
- Step 2: The bar was plotted, and the rebar shape was modified in Matlab to avoid the inclined and/or bent effects, as shown in Figure 5.4.

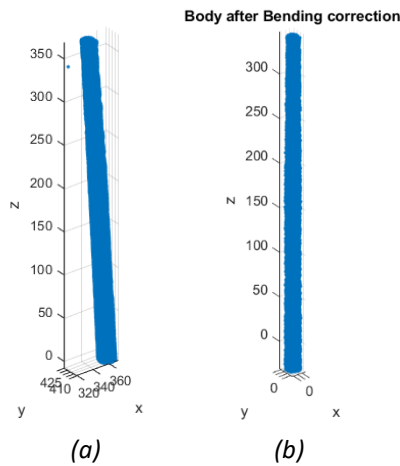


Figure 5.4. Model modification in Matlab: (a) before modification and (b) after modification

- Step 3: The coordinates of the obtained points were transformed into a polar coordinate system. The cross-sectional area at a series of sections uniformly spaced was obtained by the integration of the coordinates, following equation 5.1:

$$A(x') = \int_{-\pi}^{\pi} \frac{r'(\theta, x')^2}{2} d\theta' \quad (5.1)$$

To eliminate the effect of ribs on the cross-sectional variation along the bar, a smoothing fit was applied, resulting in cross-sectional area shown in Figure 5.5.

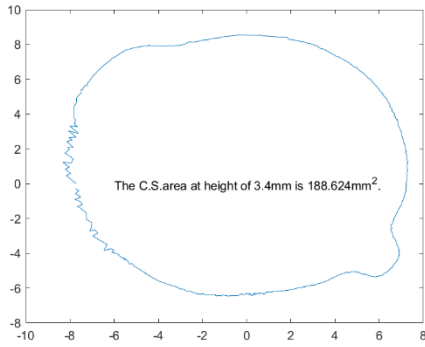


Figure 5.5. Typical corrosion sectional area at a specific height

- Step 4: The cross-sectional area along the bar was calculated and plotted, as shown in Figure 5.6.

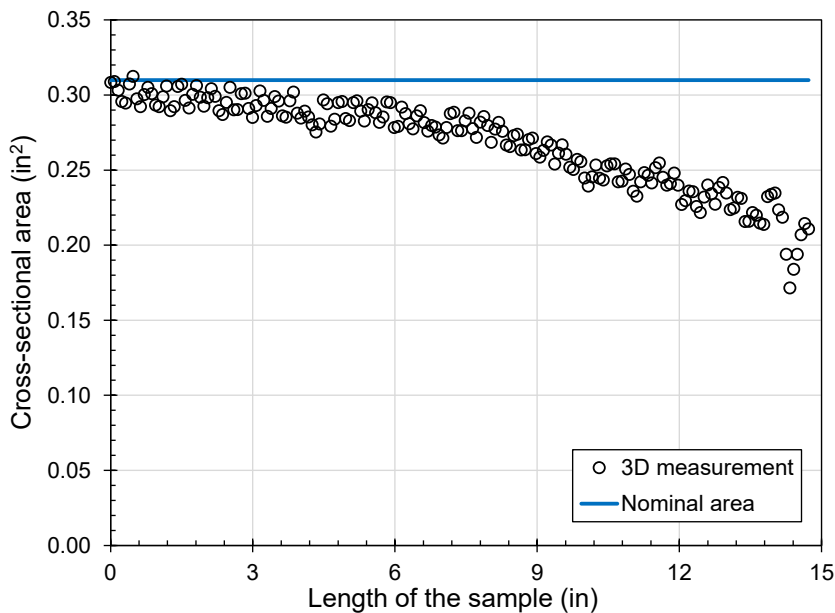


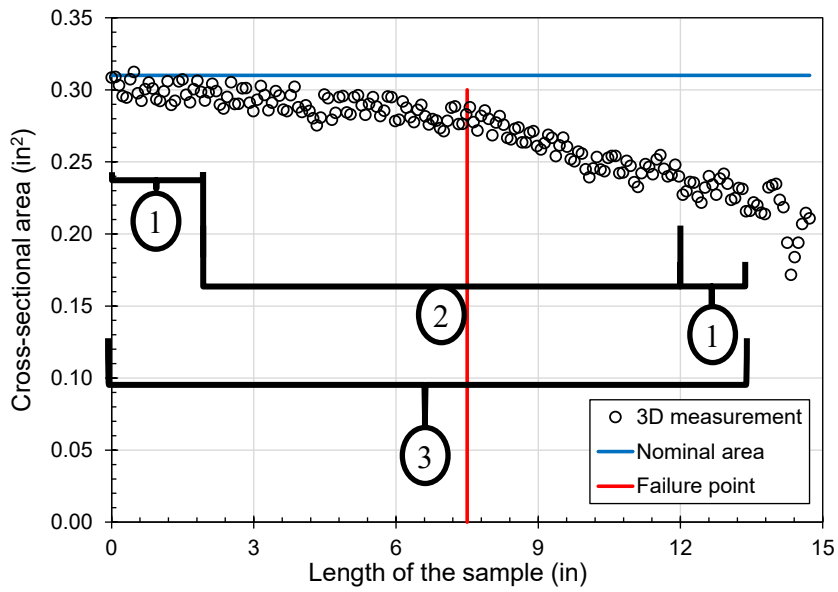
Figure 5.6. Measured cross-sectional area along the S1 bar

- Step 5: The corrosion level variation (as a percentage) was determined by first identifying the nominal cross-sectional area, e.g., 0.31 in² for a #5 bar, as reference. The ratio of the mean cross-sectional area (calculated in Matlab) for the corroded rebar sample to its nominal cross-sectional area was used for finding the section loss.

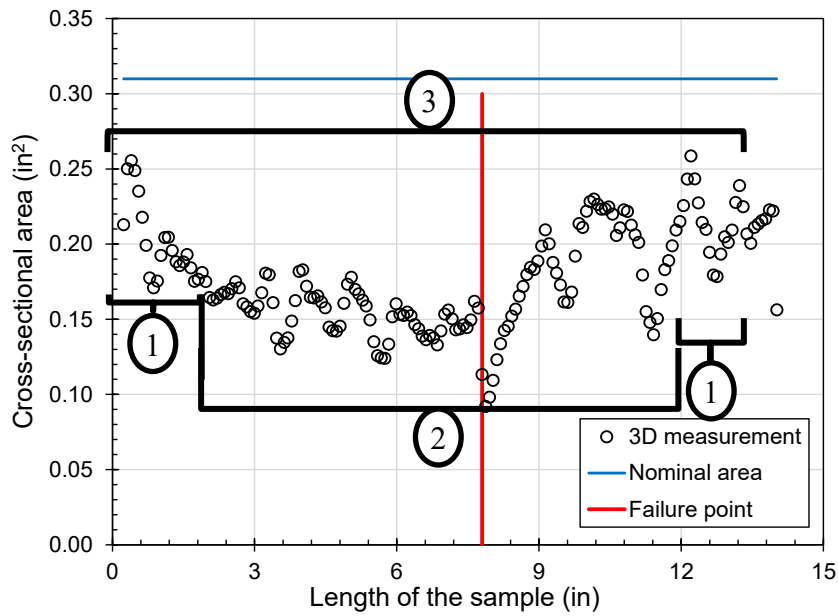
Figure 5.7 presents the obtained cross-sectional area variations along the length of the rebar samples (with an interval of 2 mm). It should be noted that the original size of S10 was 68 in. To perform 3D scanning on this sample, it was cut into two sections of equal length, labeled as S10 and S11.

Figure 5.7 also designates sample segments where the reported section loss calculations are taken as follows:

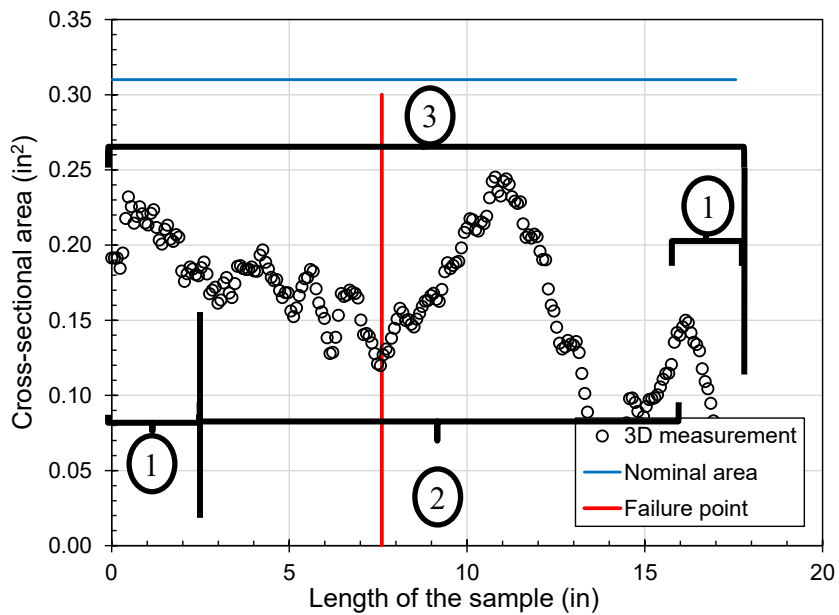
1. Grip area for tensile tests; some tests broke close to grips
2. Approximate region between grips for tensile tests
3. Segment used to compute average section loss



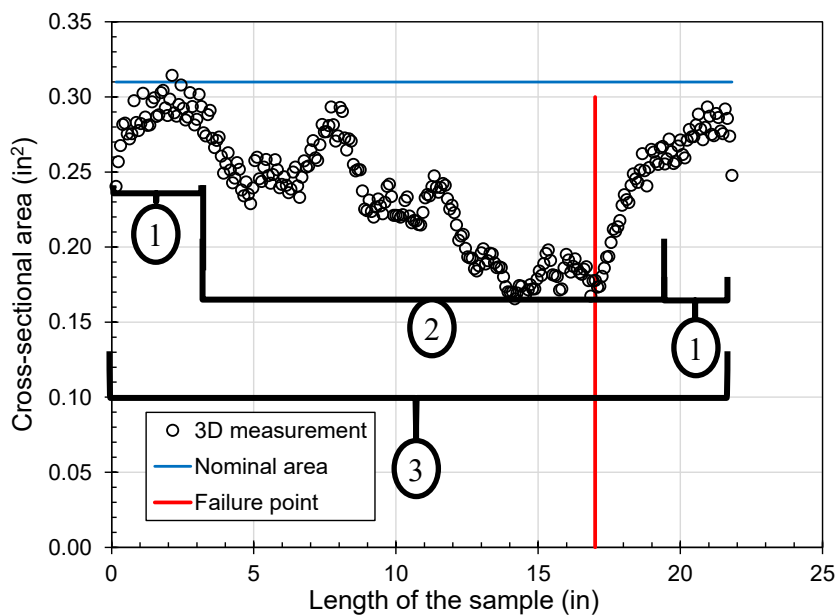
S1



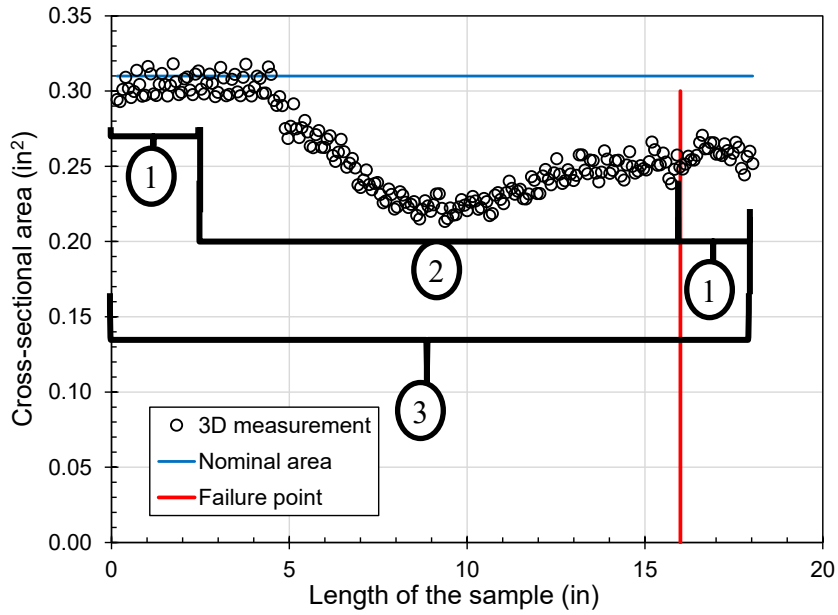
S2



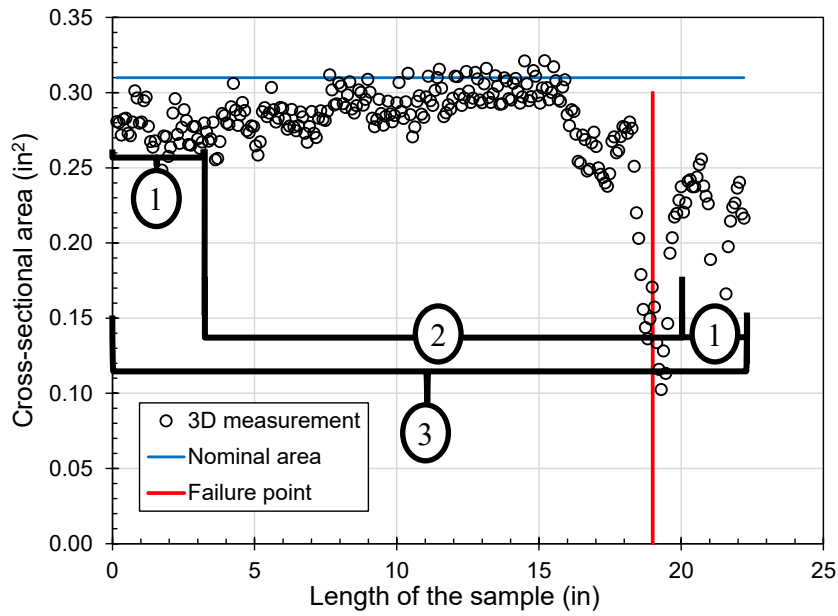
S3



S4

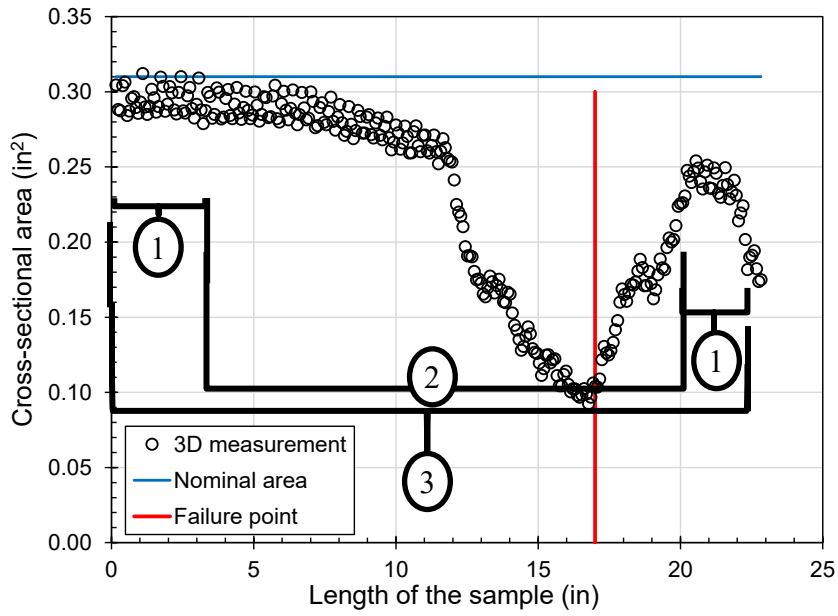


S5

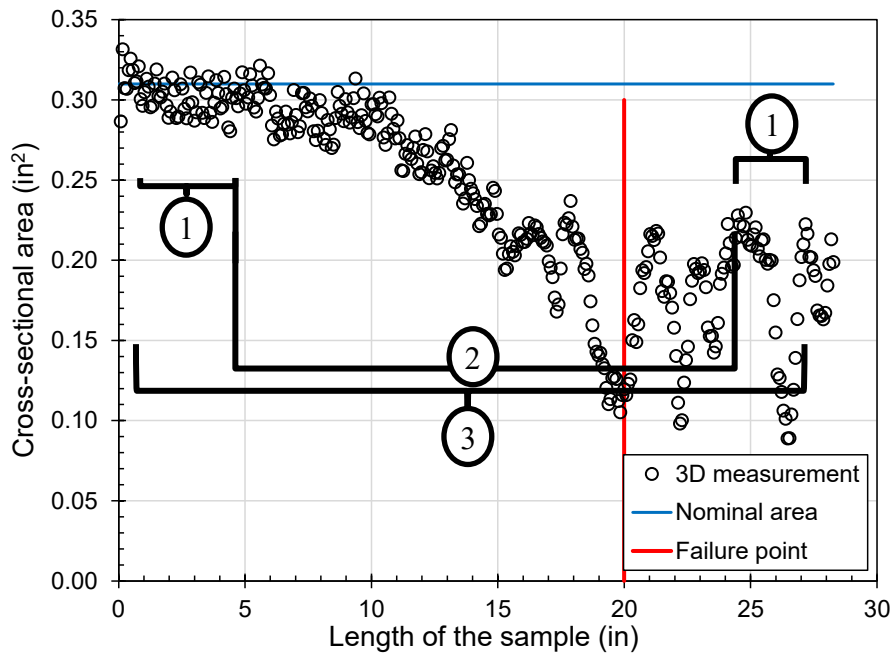


S6*

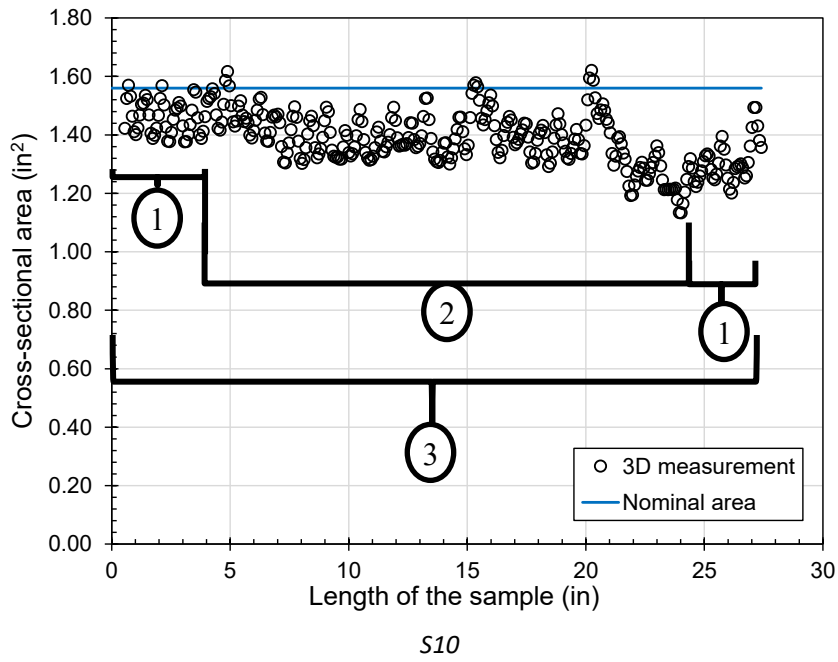
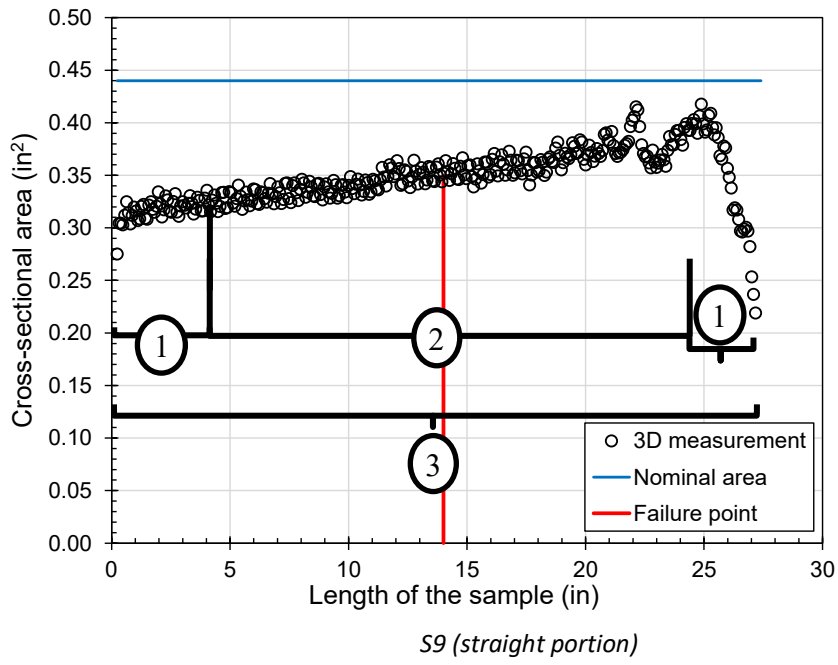
* The exceedance of the nominal cross-sectional area can be due to the rust accumulation on the rebar surface.

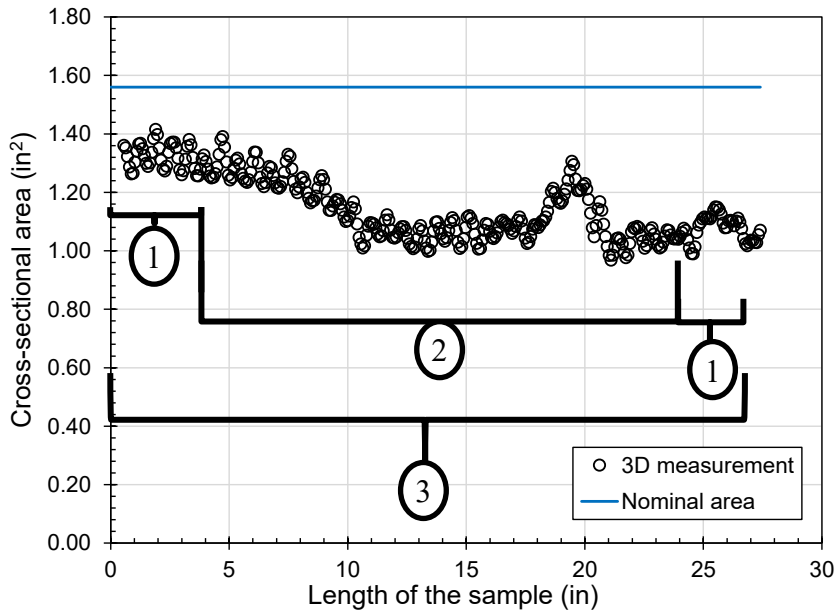


S7



S8





S11

Figure 5.7. Cross-sectional area variation along the length of the rebar samples

5.2.2 Comparison of Corrosion Level

A direct comparison between the visual section loss assessment and the maximum section loss measurement by 3D scanning is documented in Table 5.2. All the extracted bars presented in this table were from delaminated locations but not open spalls. The maximum section loss measured by 3D scanning is calculated as the ratio between the minimum remaining cross-sectional area along the entire length of the rebar to the nominal cross-sectional area. As reflected in this table, the two methods are in good agreement when the visual section loss assessment is relatively large, i.e., above 75%. The noted variations, however, significantly increase when the visual assessment estimated small section losses. This is mainly due to the natural characteristic of the visual inspection, which is not capable of making precise measurements, especially for the reinforcement steel covered with rust and/or partially embedded in concrete, as shown in Figure 5.8, which presents photos of extracted rebar samples without cleaning. Similarly, Figure 5.9 illustrates the photos taken from Pier 46WB during the inspection in 2018 and repair in 2020. As reflected in this figure, which represents several similar situations in the field, the visual assessment and direct measurement of rebar section loss are difficult to perform on site. Therefore, to achieve the expected accuracy, employing a proper methodology for rebar section loss assessment is critical.

Table 5.2. Maximum section loss expressed in percentage (%) of full bar length from each specimen (based on worst section loss)

Rebar ID	Nominal diameter (in.)	Maximum section loss (%)		Average section loss (%)
		Visual assessment	3D scanning	3D scanning
S1	#5	5	45	14
S2	#5	75	70	43
S3	#5	90	86	49
S4	#5	30	47	23
S5	#5	5	31	16
S6	#5	15	67	13
S7	#5	5	70	26
S8	#5	50-75	71	24
S9	#6	10 (straight) + 100 (bend)	32 (straight portion only)	21 (straight portion only)
S10	#11	5-10	67	12
S11	#11	5-10	38	14



Figure 5.8. Rebar samples extracted from the bridge piers under consideration



(a)



(b)



(c)

Figure 5.9. Rebar visual assessment for Pier 46WB: (a) 2018 inspection photo, (b) 2020 photo during repair, and (c) bar sample extracted from the pier

In addition, the average corrosion loss for each bar was calculated using both weight (lb/ft.) measurement and 3D scanning. It should be noted that weight loss is an approximate method because the exact initial weight of each bar before corrosion is not known. Thus, the nominal reinforcement bar’s unit weight was used as a reference and the section loss calculated from weight measurement, as expressed in Equation 5.2.

$$\text{Measured weight loss} = (1 - \text{Measured unit weight} / \text{Nominal unit weight}) \times 100\% = \quad (5.2)$$

A direct comparison between the two section loss measurement methods is shown in Table 5.3. As reflected in Table 5.3, the results from the weight loss method were overall consistent with those obtained from 3D scanning measurements. It should be noted that, instead of maximum section loss, Table 5.3 reports the average section loss measured from 3D scanning along the whole rebar length.

Table 5.3. Average section loss expressed in percentage (%) for each specimen

Rebar ID	Nominal diameter (in.)	Average section loss (%)		Difference (i) - (ii)
		Weight measurement (i)	3D measurement (ii)	
S1	#5	18	14	4
S2	#5	46	43	3
S3	#5	54	49	5
S4	#5	24	23	1
S5	#5	19	16	3
S6	#5	18	13	5
S7	#5	15	26	-11
S8	#5	24	24	0
S9	#6	52 (straight and bent portion)	21 (straight portion only)	-
S10	#11	13	12	1
S11	#11	27	27	0

Note that sample S9 appeared as an anomaly when assigned as a #6 rebar size. The rebar had the appearance of very low section loss yet was clearly larger than a #5 rebar. There is uncertainty if rebar S9 was conforming to English standards.

5.3 TENSILE TESTING

Upon completing rebar section loss measurements, corroded steel bars were subjected to the tensile tests using an electro-hydraulic servo MTS machine, as shown in Figure 5.10. The loading rate followed the standard test method, i.e., ASTM E8 (2018). For each specimen, an extensometer (clipped on the sample) was used to determine the strain during the test. Figure 5.11 shows the failure points in the corroded rebars under tension. The load-deformation relationships recorded by the data acquisition system during the tensile tests are plotted in Figure 5.12.

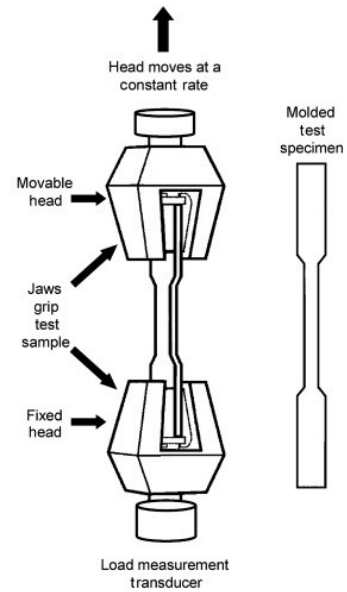
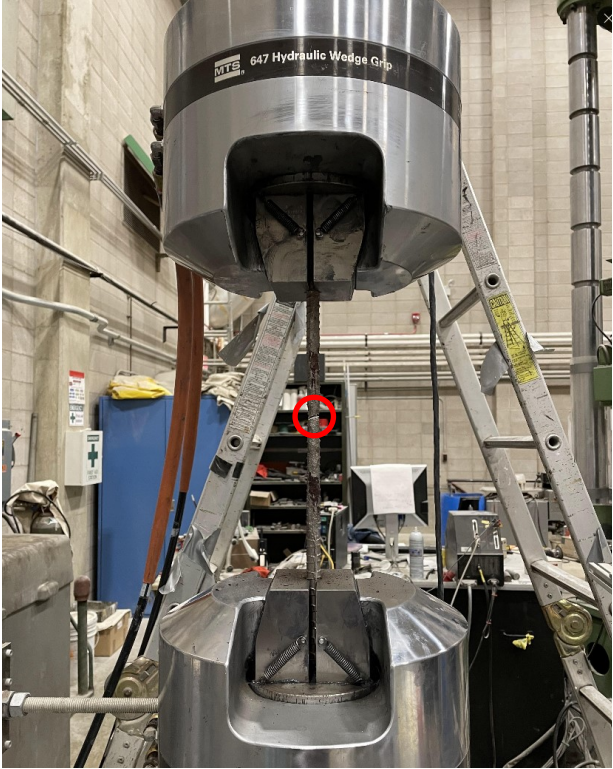
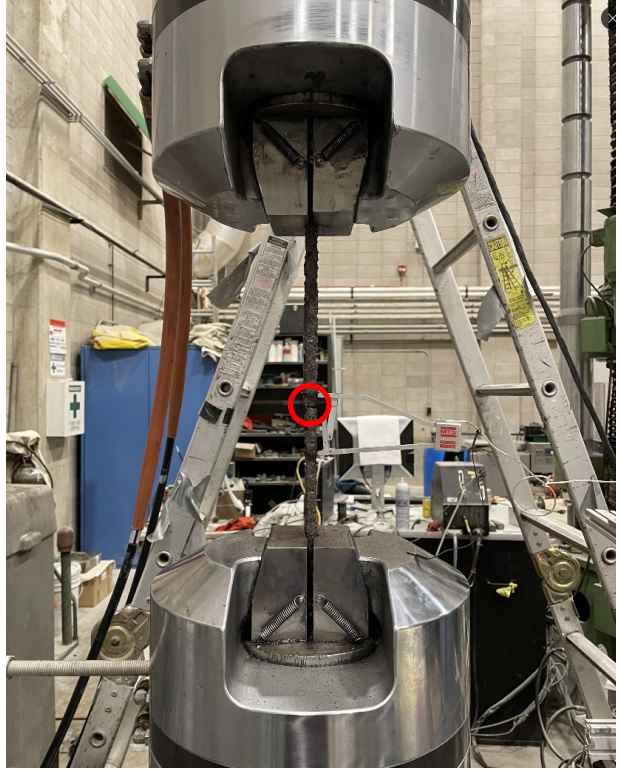


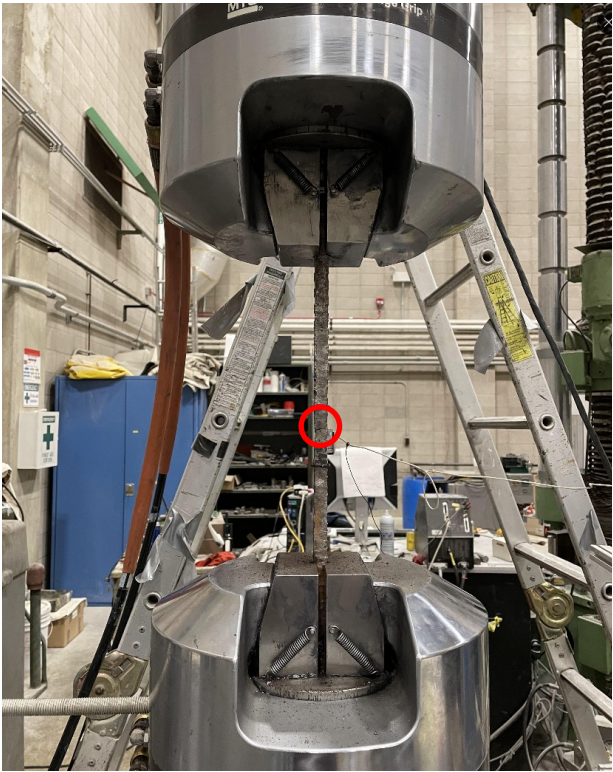
Figure 5.10. Tensile test setup used for the corroded steel bars



S1



S2



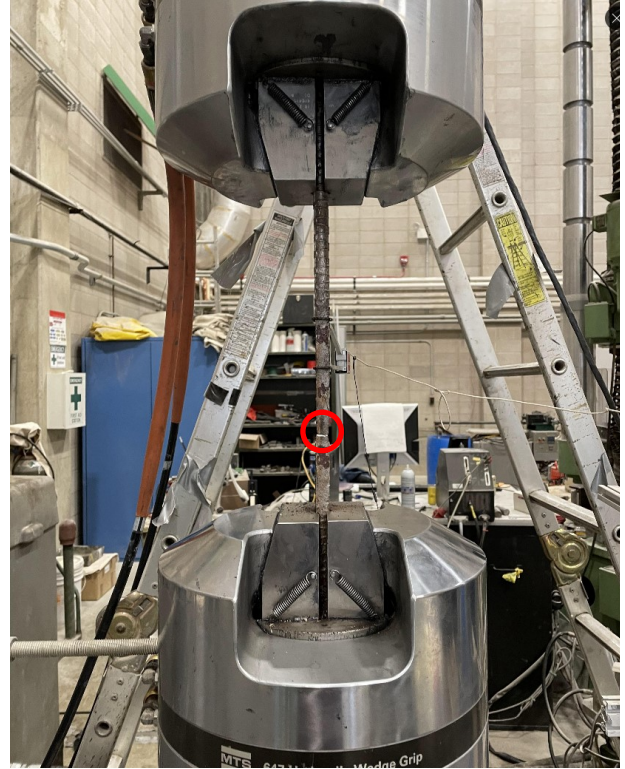
S4



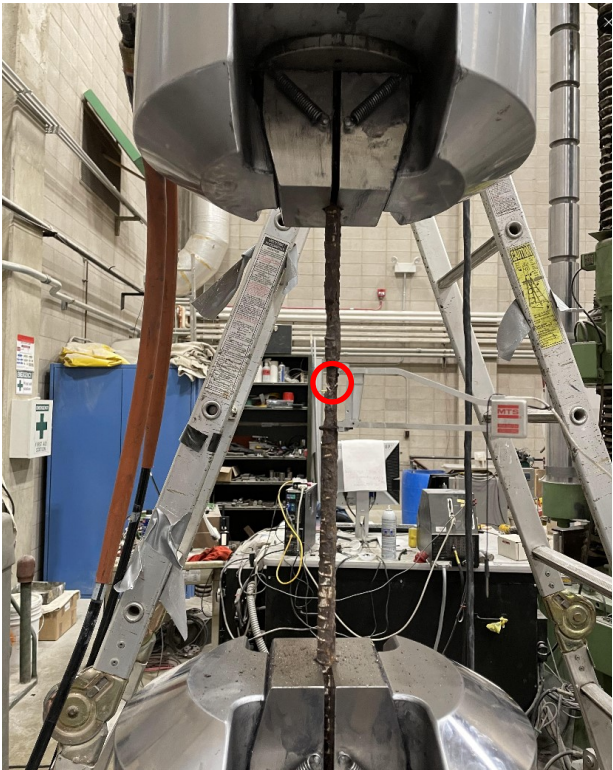
S5



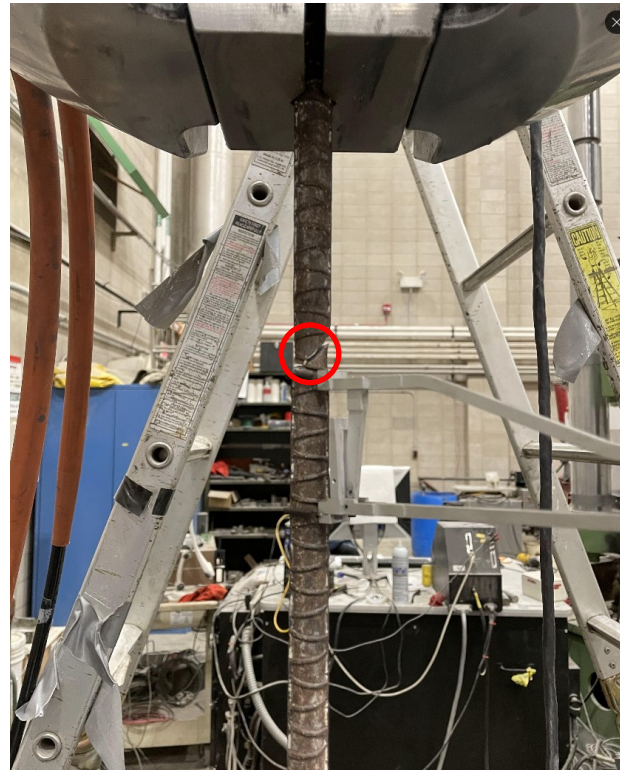
S6



S7

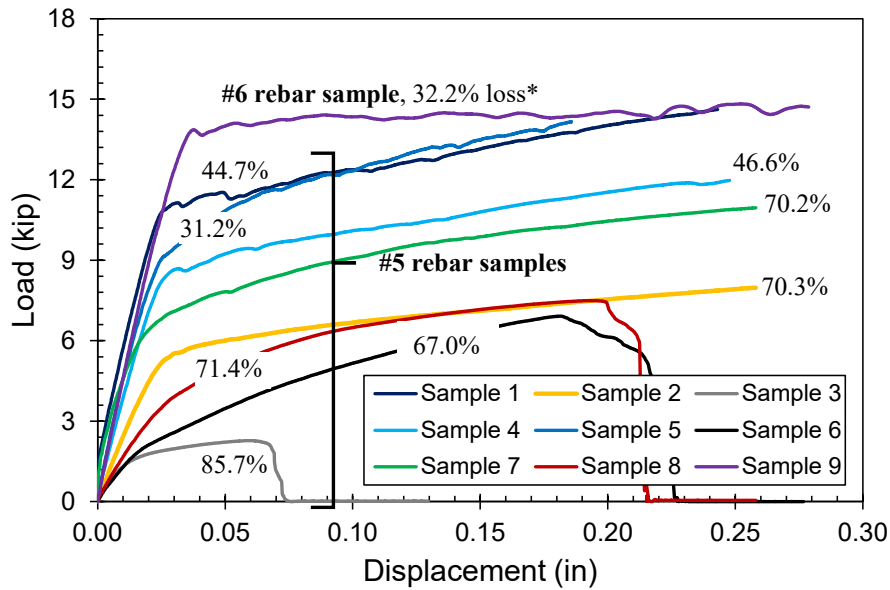


S8

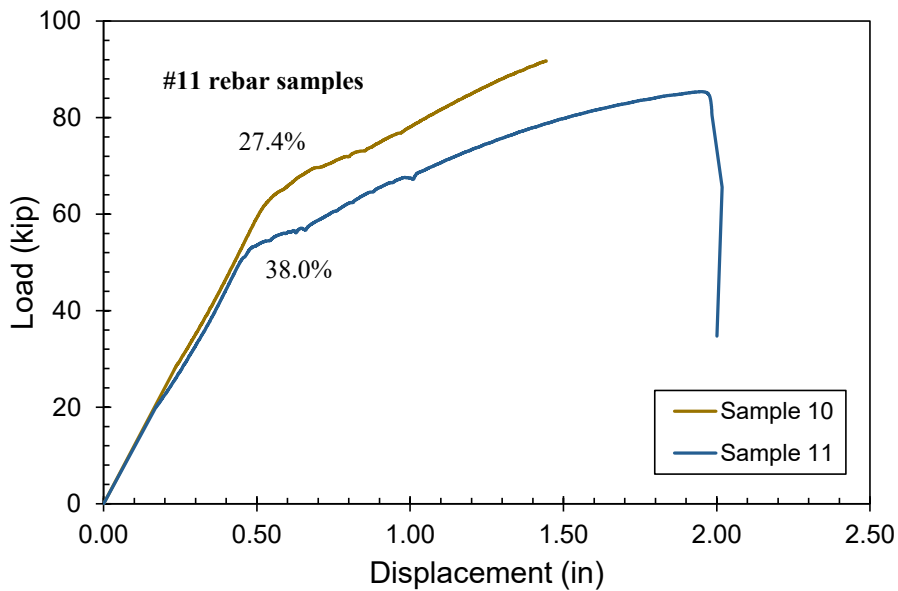


S9

Figure 5.11. Failure points in the corroded rebars under tensile tests



(a)



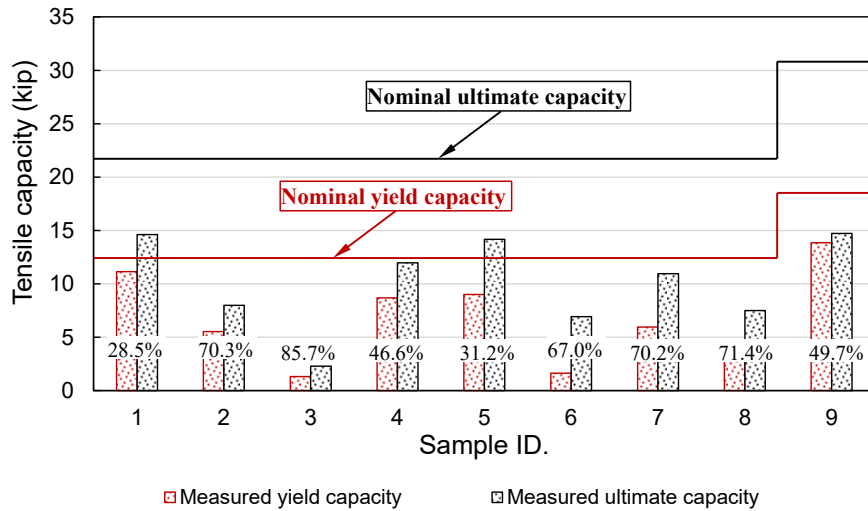
(b)

*The section loss listed for each curve is the maximum section loss recorded at the bar's middle portion (i.e., the portion between the two gripping ends). This is to avoid extreme section losses recorded at the ends, as reflected in the 3D scanning measurements.

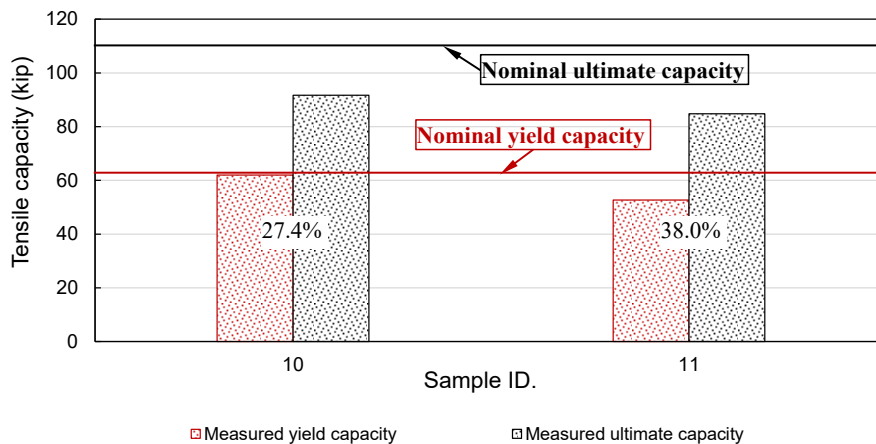
Figure 5.12. Load versus displacement curve for the corroded steel bars

Figure 5.13 documents the average yield and ultimate tensile capacity for each rebar specimen. The percentage included for each sample reflects the maximum section loss recorded at the bar's middle portion. As reflected in Figure 5.13, both the yield and ultimate tensile capacity of the rebar samples were significantly affected. It must be noted that the bridge design plans followed 1965 specifications and stated that some rebars are "intermediate grade." This refers to reinforcement with a yield strength

of 40 ksi and an ultimate tensile strength of 70 ksi. However, it is common for contractors to provide materials that meet or exceed specifications, and the minimal strength of the reinforcement may be up to 60 ksi without section loss. Therefore, the yield and ultimate tensile capacity of #5 intermediate grade rebar are found to be 12.4 kip and 21.7 kip, respectively. The yield and ultimate tensile capacity of #6 intermediate grade rebar are determined to be 17.6 kip and 30.8 kip, respectively. Similarly, the yield and ultimate tensile capacity of #11 intermediate grade rebar are found to be 62.4 kip and 109.2 kip, respectively.



(a)



(b)

Figure 5.13. Summary of tensile test results

Table 5.4 presents a direct comparison of laboratory-tested strength loss as compared to visual and measured area losses. As reflected in this table, it appears that the visual loss assessments may overestimate the remaining strength for lower section losses. In contrast, the maximum section loss estimated by the 3D scanning method had a good agreement with the measured strength loss. This is because the fracture in a tensile test specimen often initiates at its weakest point, usually where there is an impurity or at its smallest cross-sectional area. Thus, as mentioned earlier, the measurement

performed by 3D scanning allows detailed and very accurate quantity calculations, resulting in a better agreement with test results than visual assessments.

Table 5.4. Comparison of laboratory test results to visually assessed and measured area losses

Rebar ID	Nominal diameter (in.)	Design yield strength* (kip)	Measured yield strength (kip)	Strength loss (%)	Maximum section loss (%)	
					Visual assessment	3D scanning
S1	#5	12.4	11.1	10	5	45
S2	#5	12.4	5.5	55	75	70
S3	#5	12.4	1.3	89	90	86
S4	#5	12.4	8.7	30	30	47
S5	#5	12.4	9.0	27	5	31
S6	#5	12.4	1.6	87	15	67
S7	#5	12.4	5.9	52	5	70
S8	#5	12.4	3.7	70	50-75	71
S9	#6	17.6	13.8	21	10	32
S10	#11	62.4	62.0	1	5-10	27
S11	#11	62.4	52.7	16	5-10	38

* Assuming a 40 ksi yield strength

5.4 OVERALL ASSESSMENT

With the activities reported in this chapter, first-hand information was obtained regarding the extent of corrosion of embedded steel bars. The surface morphology of extracted steel samples was scanned with 3D scanning technology, and a three-dimension model was established. The scanned samples' minimum and average cross-sectional area were then determined along their entire length and compared to the other two estimated methods: visual assessment and weight measurement. In addition, tensile tests were performed on the collected rebar samples to measure their remaining tensile capacity.

3D-scanning was used to characterize the corroded rebar morphology and evaluate the maximum local corrosion level of extracted rebars. From the assessments of the maximum cross-sectional area, the two methods, i.e., 3D scanning and visual assessment, were found to be in good agreement when the visual section loss assessment is relatively large, i.e., above 75%. The noted variation, however, significantly increases when the visual assessment targets small section losses. As previously noted, this is mainly due to the natural characteristics of visual inspection, which is not capable of making precise measurements, especially for the reinforcement covered with rust and/or partially embedded in concrete. For the estimation of average cross-sectional area, the results from the weight loss method were overall consistent with those obtained from average 3D scanning measurements. Based on the tensile test results, the visual loss assessments may overestimate the remaining strength for small section losses. In contrast, the section loss estimated by 3D scanning method closely captured the measured strength losses.

CHAPTER 6: PREDICTIVE MODELS FOR REBAR SECTION LOSS

6.1 INTRODUCTION

Corrosion of steel reinforcement embedded in concrete is known to adversely affect the strength and durability of RC structures subjected to harsh environmental stressors (Khatami et al., 2016; Kulkarni and Shafei, 2018; Cui et al., 2019; Alipour and Shafei, 2022). Steel corrosion commonly takes place in a two-stage process, i.e., initiation and propagation. In the first stage, water and aggressive agents penetrate into the concrete's pore structure toward embedded steel rebars. Once the concentration of ions accumulated on the rebar surface reaches a critical threshold, the pH level decreases and the protective passive film surrounding the rebar is disrupted. By the end of the initiation stage, a set of electrochemical reactions begin to take place, leading to the second stage of corrosion, in which the formation and propagation of corrosion products (also known as rust) occur. Noting that the rust has a higher volume than the consumed steel, the second stage of corrosion causes excessive stresses to the surrounding concrete, resulting in various levels of structural deterioration, ranging from individual concrete cracks to cover delamination and spalling.

In this research project, several empirical models have been identified and reviewed, especially to evaluate the deterioration of RC structural elements. The available empirical models, however, should be used with caution, as many of them have been developed for specific structural components and exposure conditions, which prevent their immediate use for other scenarios without appropriate calibration and validation. Thus, during this research project, data was collected regarding the extent of steel corrosion in real settings through various direct measurements and visual assessments. This information has been employed in the current chapter to develop and calibrate a set of predictive models identified for rebar cross-sectional loss assessment.

To assess the extent of rebar section loss, a two-situation predictive model has been developed: (1) Situation I: The concrete cover has maintained its overall integrity, despite some individual cracks, and (2) Situation II: The concrete cover has experienced delamination or is completely lost, exposing the embedded steel rebars. Given the two introduced situations, which cover most of structural deterioration scenarios in RC structures, the main scope of this chapter is twofold: (1) to establish a correlation between the corrosion-induced crack width and the rebar section loss in Situation I and (2) to estimate the progress of corrosion and rebar section loss over time in Situation II. Figure 6.1 provides a schematic illustration of various stages of corrosion.

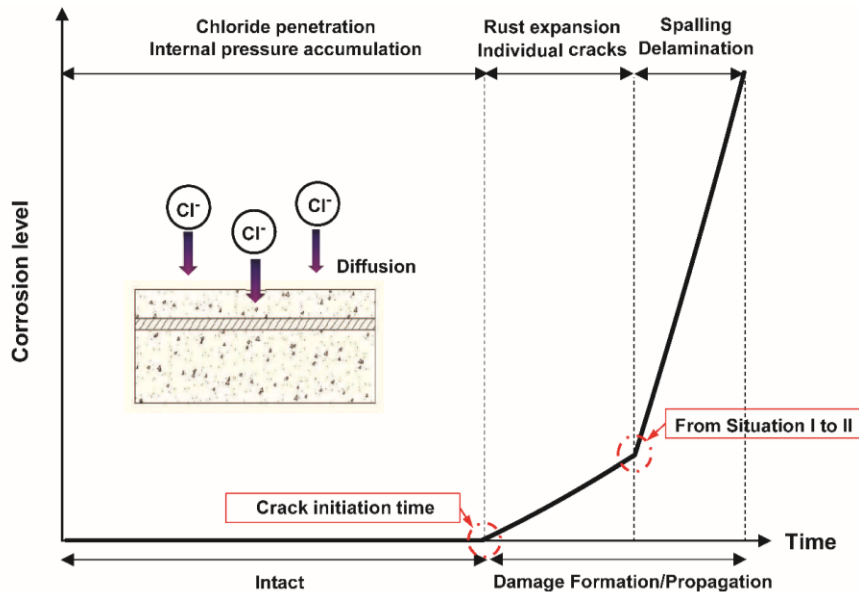


Figure 6.1. Schematic illustration of various stages of corrosion

6.2 MODELS FOR PREDICTING STEEL SECTION LOSS

To develop a set of predictive models that can offer both accuracy and flexibility, a power function is considered as the base model. Such power function has been widely employed in the literature, owing to the advantage that it can be directly calibrated for the structural components and exposure conditions of interest. Among the oldest studies that have employed a power function for corrosion-related studies, Pourbaix (1980) and Albrecht and Naeemi (1984) can be highlighted. The first cited study has reported that a power law is appropriate for corrosion predictions in different atmospheres and for different types of steel materials. Similarly, the second cited study shows how the corrosion of carbon steel can be successfully assessed in different exposure conditions, including marine, urban, and rural.

The general form of the power function can be expressed as follows:

$$C = Ax^n \quad (6.1)$$

where C is the extent of steel section loss, x is the most critical contributing factor, and A and n are two constants. To accurately utilize Equation 6.1, it needs to be first fitted to the field data collected for a given structural component and exposure condition. The fitting process determines the two constants, making the equation appropriate for similar structural components and exposure conditions. The following sections present the details of how the introduced power function is utilized for Situations I and II.

- Situation I for individual cracks, the widths of which can be determined from map cracking by site measurement and/or visual assessment

- Situation II for advanced corrosion-induced damage, which is often characterized by (1) delamination (determined by hammer sounding) or (2) concrete spalling (determined by visual assessment)

6.3 SITUATION I – INDIVIDUAL CRACKS

The studies available in the literature for Situation I were thoroughly reviewed. The predictive models that relate the crack width, as the most notable sign of steel corrosion, to the rebar’s mass loss were then established. For this purpose, the outcome of Vidal et al. (2004), Zhang et al. (2010), and Khan et al. (2014) was employed.

6.3.1 Vidal et al. (2004)’s Model

Based on the investigation of naturally corroded, reinforced concrete components, Vidal et al. (2004)’s model predicts the loss of reinforcement based on the crack width. According to Vidal et al. (2004), the crack width during the propagation stage of corrosion is proportional to the volume of oxides, which is, in turn, proportional to the cross-sectional loss of steel rebars. Figure 6.2 shows the comparison of Vidal et al. (2004)’s experimental test data with the predictive model developed based on Equation 6.1. For the upper and lower bounds in the predictive model, the values obtained for parameters A and n are given in Table 6.1.

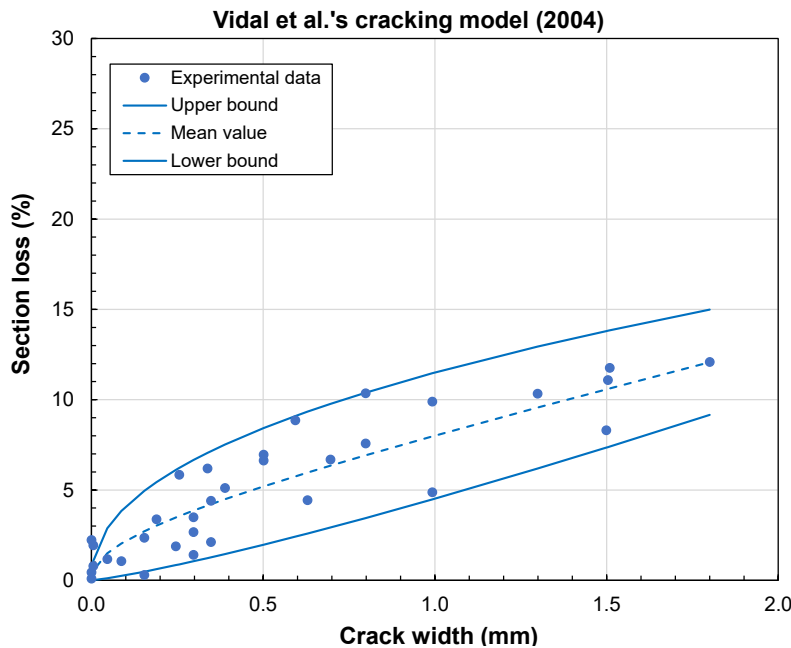


Figure 6.2. Comparison of the developed predictive model with the experimental test data from Vidal et al. (2004)

Table 6.1. Constants obtained for the power function based on the data from Vidal et al. (2004)

Scenario	$A/\mu\text{m}$	n
Upper bound	11.50	0.45
Lower bound	4.52	1.20

6.3.2 Zhang et al. (2010)'s Model

For the crack propagation stage, when corrosion spreads over the rebar's length, Zhang et al. (2010) investigated the average cross-sectional loss. Figure 6.3 shows the comparison of Zhang et al. (2010)'s experimental test data with the predictive model developed based on Equation 6.1. For the upper and lower bounds in the predictive model, the values obtained for parameters A and n are given in Table 6.2.

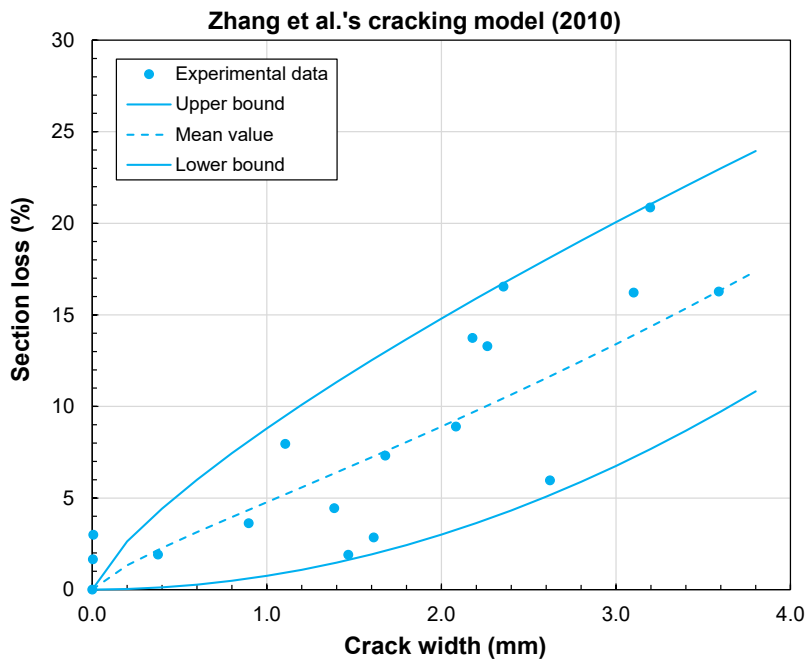


Figure 6.3. Comparison of the developed predictive model with the experimental test data from Zhang et al. (2010)

Table 6.2. Constants obtained for the power function based on the data from Zhang et al. (2010)

Scenario	$A/\mu\text{m}$	n
Upper bound	8.80	0.75
Lower bound	0.75	2.00

6.3.3 Khan et al. (2014)'s Model

Khan et al. (2014) investigated the progress of reinforcement corrosion in a heavily corroded reinforced concrete component with a focus on corrosion-induced crack width. To study the corrosion pattern and assess the mass loss of steel reinforcement, crack and corrosion maps were prepared and compared. Figure 6.4 shows the comparison of Khan et al. (2014)'s experimental test data with the predictive model developed based on Equation 6.1. For the upper and lower bounds in the predictive model, the values obtained for parameters A and n are given in Table 6.3.

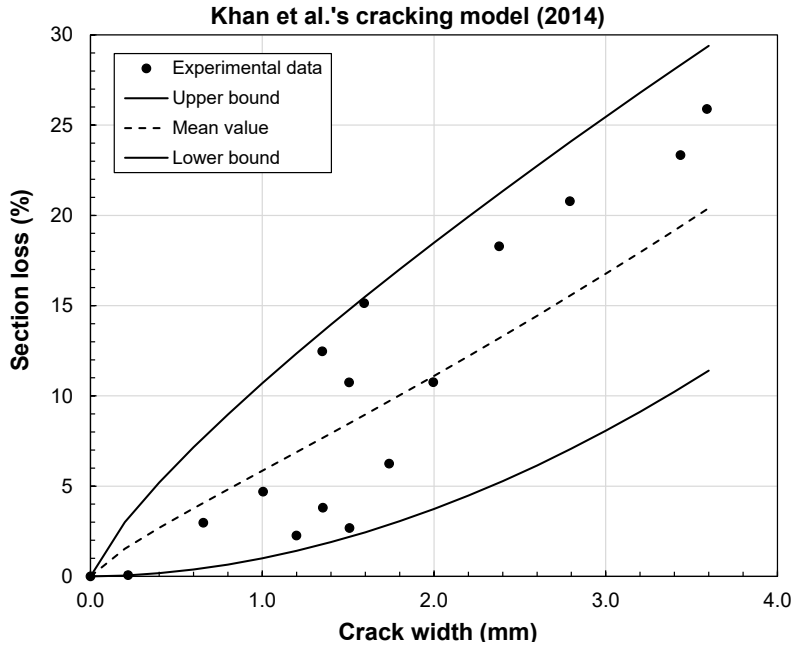


Figure 6.4. Comparison of the developed predictive model with the experimental test data from Khan et al. (2014)

Table 6.3. Constants obtained for the power function based on the data from Khan et al. (2014)

Scenario	$A/\mu\text{m}$	n
Upper bound	10.7	0.79
Lower bound	1.00	1.90

6.3.4 Final Model for Situation I

Based on the most relevant data collected and processed for Situation I, along with the identified upper and lower bounds for each of the data sets, a predictive model has been developed for assessing a rebar's section loss using the upper bound from Vidal et al. (2004)'s model and the lower bound was from Zhang et al. (2010)'s model.

Specifically, the variables shown in Table 6.4 are proposed.

Table 6.4. Constants obtained for the power function for Situation I model

Scenario	$A/\mu\text{m}$	n
Upper bound	11.50	0.45
Lower bound	0.75	2.00

Figure 6.5 presents the proposed power function and illustrates how data from prior research would fall within the bounds. To utilize this model for real practical applications, the following, easy-to-follow steps are suggested to be taken:

- Step 1: Photos of the cracked structural component should be taken with an appropriate scale included. Alternatively, field measurement can be performed using a crackmeter.
- Step 2: Determinate the crack width.
- Step 3: Input the crack width into the predictive model.
- Step 4: Calculate the mean rebar section loss, in addition to upper and lower bounds.

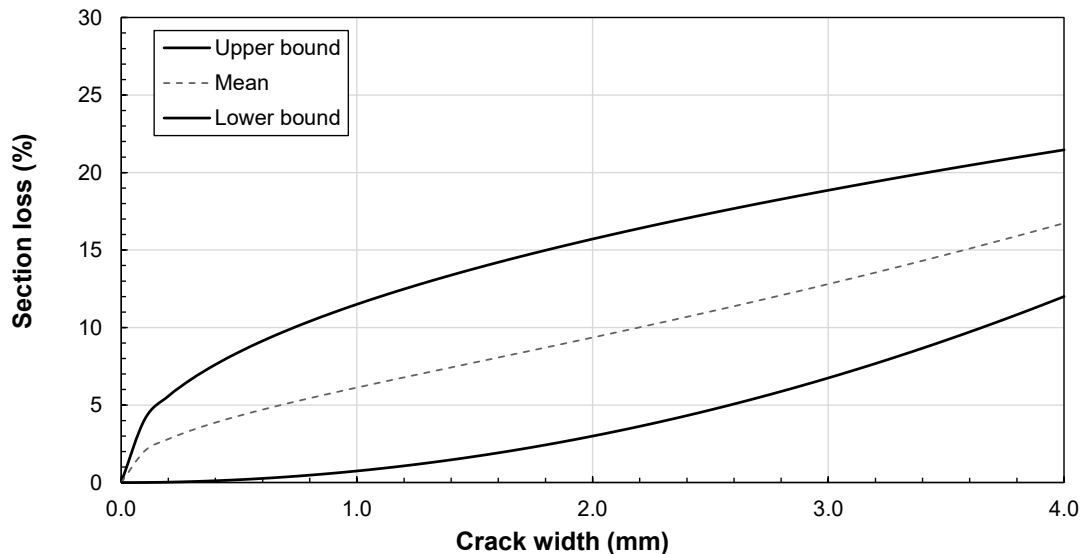


Figure 6.5. Developed plot for predicting steel section loss in Situation I

6.4 SITUATION II – DELAMINATION AND SPALLING

Similar to Situation I, the studies most relevant to the advanced stage of damage, i.e., delamination and spalling, were thoroughly reviewed for Situation II. Considering the extent of damage incurred in Situation II, the crack width is not an appropriate measure of corrosion progress anymore. Thus, given the fact that the rebar section loss in Situation II is primarily governed by the electrochemical process of corrosion in an exposed steel rebar, exposure time is deemed one of the most important contributing factors. For the purpose of developing an appropriate predictive model for Situation II, the outcome of two studies, i.e., Vidal et al. (2007) and Zhu et al. (2015), was employed.

6.4.1 Vidal et al. (2007)'s Model

Vidal et al. (2007) investigated the reinforced concrete structural components that had been naturally exposed to corrosion. At different time intervals, corrosion-induced structural damage was recorded, and the percentage of steel section loss was estimated over time. Figure 6.6 shows the comparison of Vidal et al. (2007)'s experimental test data with the predictive model developed based on Equation 6.1. For the upper and lower bounds in the predictive model, the values obtained for parameters A and n are given in Table 6.5.

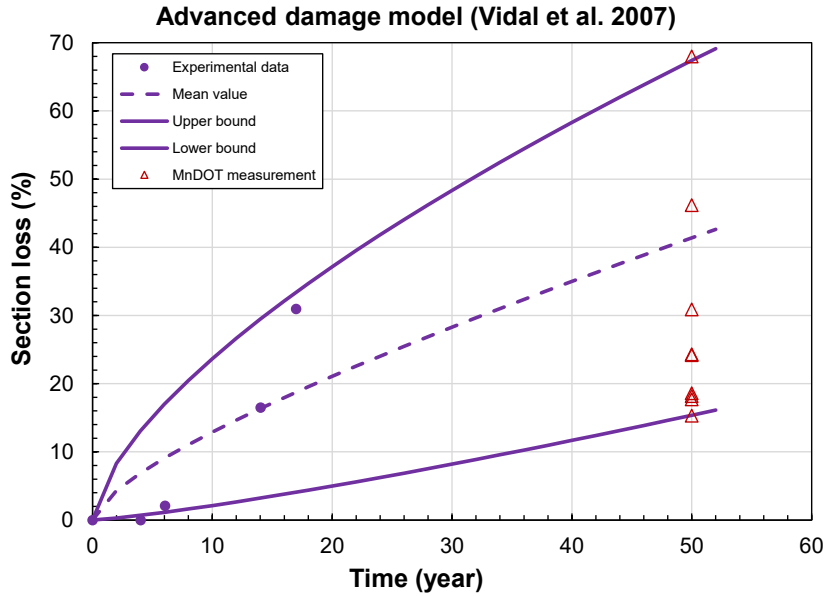


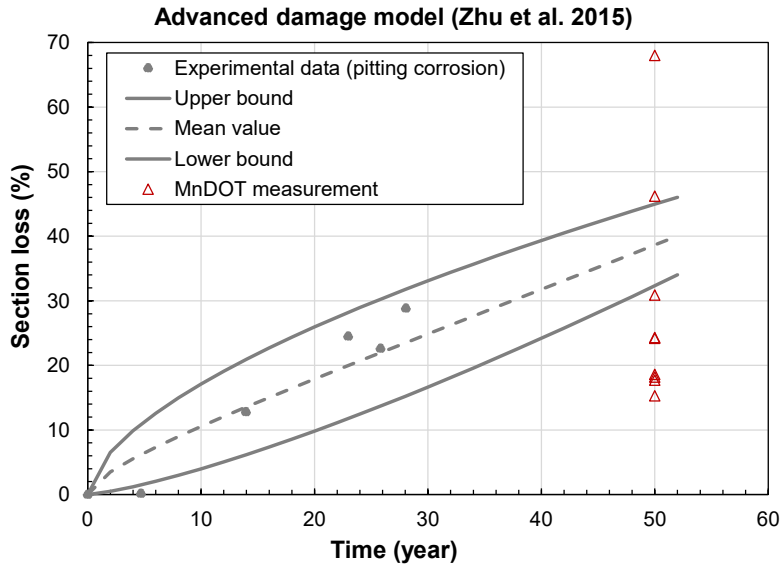
Figure 6.6. Comparison of the developed predictive model with the experimental test data from Vidal et al. (2007)

Table 6.5. Constants obtained for the power function based on the data from Vidal et al. (2007)

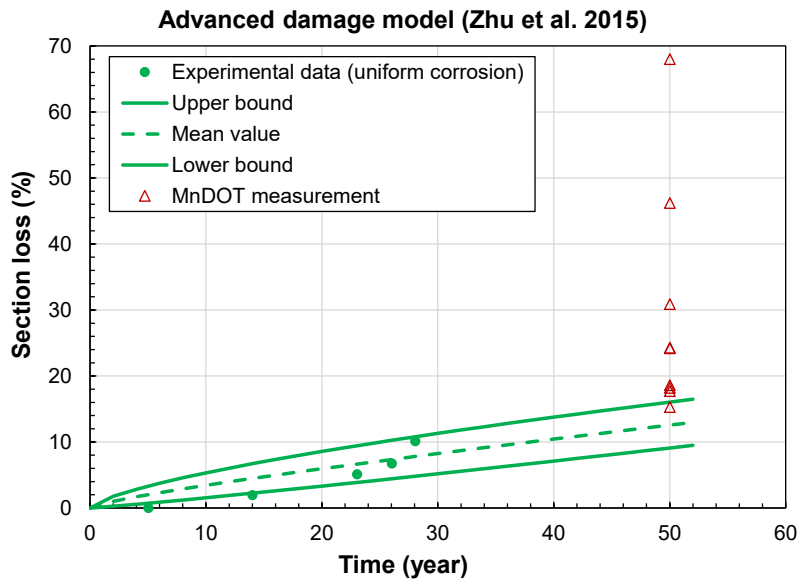
Scenario	$A/\mu\text{m}$	n
Upper bound	10.70	0.79
Lower bound	1.00	1.90

6.4.2 Zhu et al. (2015)'s Model

Zhu et al. (2015) investigated the remaining cross-section of embedded reinforcement after corrosion, as a function of time. One of the features of Zhu et al. (2015)'s model was to examine both pitting corrosion (i.e., maximum mass loss) and uniform corrosion (i.e., average mass loss). Figure 6.7 show the comparison of Zhu et al. (2015)'s experimental test data with the predictive model developed based on Equation 6.1. For the upper and lower bounds in the predictive model, the values obtained for parameters A and n are given in Table 6.6.



(a)



(b)

Figure 6.7. Comparison of the developed predictive model with the experimental test data from Zhu et al. (2015) for (a) pitting corrosion and (b) uniform corrosion

Table 6.6. Constants obtained for the power function based on the data from Zhu et al. (2015)

Corrosion Type	Scenario	$A/\mu\text{m}$	n
Pitting corrosion (maximum)	Upper bound	4.30	0.60
	Lower bound	0.20	1.30
Uniform corrosion (average)	Upper bound	1.10	0.69
	Lower bound	0.12	1.10

6.4.3 Final Model for Situation II

Based on the most relevant data collected and processed for Situation II, along with the identified upper and lower bounds for each of the data sets, a predictive model has been developed for assessing a rebar's section loss over time, as presented in Figure 6.8. In this figure, the upper bound was selected from Vidal et al. (2007)'s model and the lower bound was selected from Zhu et al. (2015)'s model. Specifically, the following variables are proposed:

Table 6.7. Constants obtained for the power function for Situation II model

Scenario	$A/\mu\text{m}$	n
Upper bound	5.30	0.65
Lower bound	0.12	1.10

To utilize this model for real practical applications, the following, easy-to-follow steps are suggested to be taken:

- Step 1: Evaluate and confirm that the bridge component of interest suffers from an advanced corrosion-induced damage, in the form of delamination and/or spalling.
- Step 2: Determinate the age of the bridge component.
- Step 3: Input the age into the predictive model.
- Step 4: Calculate the mean rebar section loss, in addition to upper and lower bounds.

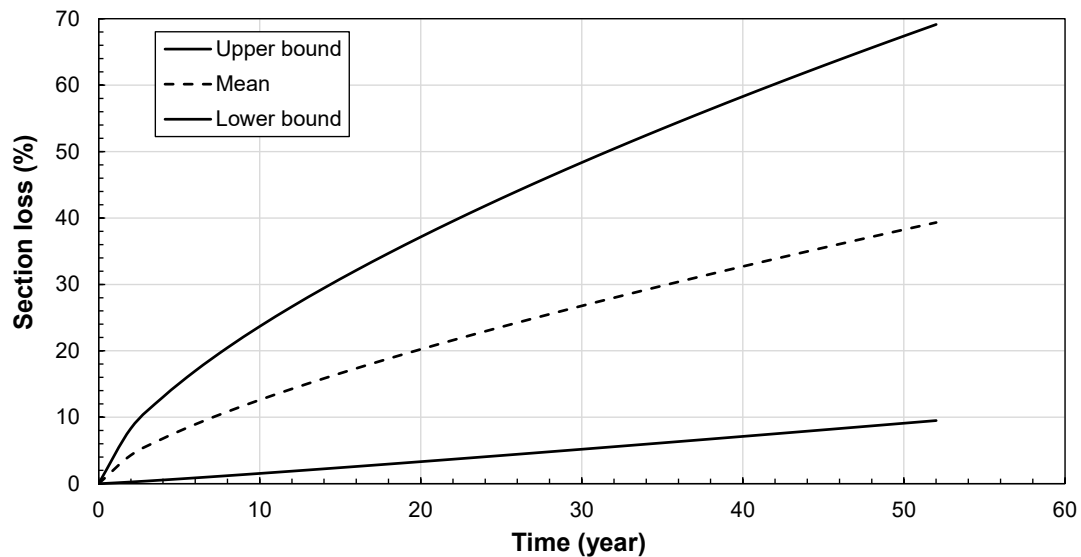


Figure 6.8. Developed plot for predicting steel section loss in Situation II

The capability of the presented models in capturing the real-world rebar section losses has been validated using the field data obtained from Bridge 27831. The mean cross-sectional area losses determined from the 3D scanning of a set of rebars collected from the referenced bridge have been presented with red triangular shapes in Figures 6.6 and 6.7. As anticipated, the field data demonstrate significant variation, depending on locations and/or exposure conditions. Despite this variation,

however, the models presented for uniform corrosion are found to successfully capture not only the mean but also the upper and lower bounds of steel section losses. With utilizing the developed predictive model from the beginning of the corrosion propagation stage (i.e., immediately after crack initiation), the mean, as well as the upper and lower bounds, of section loss can be obtained at the target bridge age. Table 6.8 summarizes the section losses obtained from the Situation II model at 10-year increments.

Table 6.8. Mean section loss at 10-year increments

Age (year)	10	20	30	40	50	60
Section loss (%) - Upper bound	23.7	37.2	48.4	58.3	67.4	75.9
Section loss (%) - Mean	12.6	20.2	26.7	32.7	38.2	43.5
Section loss (%) - Lower bound	1.5	3.3	5.2	7.1	9.1	11.1

The predictive models can certainly be further refined and validated by exploring additional bridges, which add to the diversity of ages, locations, and exposure conditions considered. This will also narrow down the range of predictions, while contributing to improving their accuracy.

Upon adequate calibration and validation, the real-world use of the developed predictive models can span a variety of capacity loss and load rating applications. In particular, when cracks are documented during an inspection, the potential for embedded steel reinforcement corrosion can be quantified using the developed predictive models. Figure 6.9 shows an example of how cracks can be recorded in the field, providing a simple yet practical input to assess the extent of rebar section loss.



Figure 6.9. An example of how the crack details recorded during an inspection can be used to obtain the input required for the developed predictive models

CHAPTER 7: CONCLUSIONS AND IMPLEMENTATION STEPS

Bridge structures in Minnesota are designed for a service life of (at least) 75 years. However, strength and durability of reinforced concrete (RC) bridges are adversely affected by the deterioration of their structural members within this lifetime. When investigating bridges in need of maintenance and repair, deterioration caused by corrosion of steel rebars is commonly found as a primary source of structural degradation. Structural degradation may result in reduced service life and is almost always associated with service interruption for maintenance and repair. Corrosion reduces the cross-sectional area of the original steel and forms expansive corrosion byproducts. These corrosion byproducts cause cracks, concrete spalling, delamination, and even bond loss in RC bridge elements.

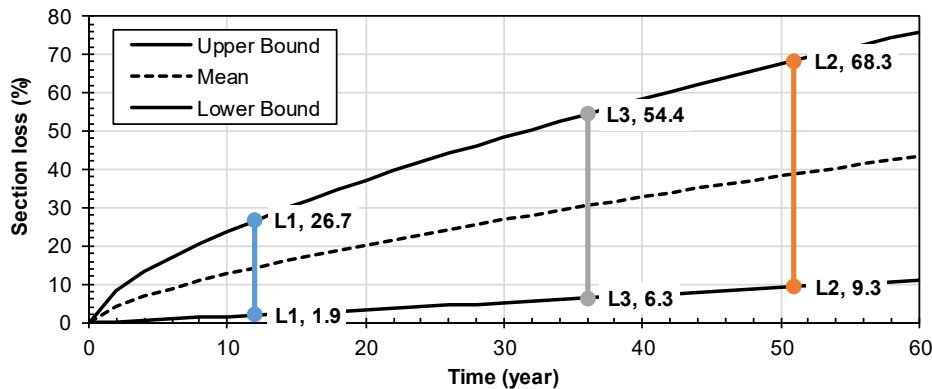
Management of a bridge structure requires understanding the structural capacity of the bridge. An accurate assessment of reinforcement section loss (without underestimation or overestimation) is necessary for both structural evaluation and capacity determination. Furthermore, the structural capacity dictates any strengthening needs and associated temporary works in a repair effort. Therefore, an accurate estimate of the extent of reinforcement section loss has central importance for a wide spectrum of engineers and decision-making authorities. Reinforcement section loss estimates are key for safety assessments and for programming repairs. These estimates can be achieved using available predictive models calibrated with condition-specific data and then validated through appropriate field investigations. Beyond immediate safety benefits, accurate reinforcement section loss estimates benefit the design and extent of strengthening. In particular, having accurate section loss estimates and structural evaluations reduces the risk of unforeseen revisions during contract repair work.

To quantify the extent of corrosion and reinforcement section loss in the bridge structures currently in service in Minnesota, this research project utilized in-service Bridge No. 27831 (I-394) near Dunwoody Institute in Minneapolis. This site provided direct access to several bridge piers scheduled for repair beginning in spring 2020. After the initiation of repair activities in the field, visual surveys were performed for an initial quantification of cross section loss. Complementary 3D scanning, mass measurements, and mechanical tests were then performed on the rebar samples collected from the field. This was to accurately assess the section loss and mechanical properties of corroded rebars. With the first-hand information obtained regarding the extent of rebar corrosion in real settings, a set of predictive models and their associated variables were identified for the prediction of rebar cross section loss. This led to the section loss guidance tables (Figure 7.1) that can be a starting point for future implementation.

Prediction of Rebar Section Loss	
Project:	Date:
Bridge ID:	
Prepared by:	

The table below provides an initial section loss prediction based on the age of the bridge component(s).

No.	Location	Additional Information	Input	Section Loss Estimate (%)			Comment
			Age (Year)	Min.	Mean	Max.	
1	Detail	P46WB pier cap, west face	12	1.9	14.3	26.7	See Next Table!
	Crack Width Available	Yes					
2	Location	51	9.3	38.8	68.3	Use with Caution!
	Crack Width Available	No					
3	Location	36	6.3	30.4	54.4	See Next Table!
	Crack Width Available	Yes					



The table below provides a more refined section loss prediction if the crack width is available/known.

No.	Location	Additional Information	Input	Section Loss Estimate (%)			Comment
			Crack Width (in)	Min.	Mean	Max.	
1	Detail	P46WB pier cap, west face	0.130	8.2	13.9	19.7	Still Use with Caution!
	Picture ID	IMG0001					
2	Location	0.080	3.1	9.5	15.8	Still Use with Caution!
	Picture ID					
3	Location	0.160	N/A	N/A	N/A	Crack is Too Wide!
	Picture ID					

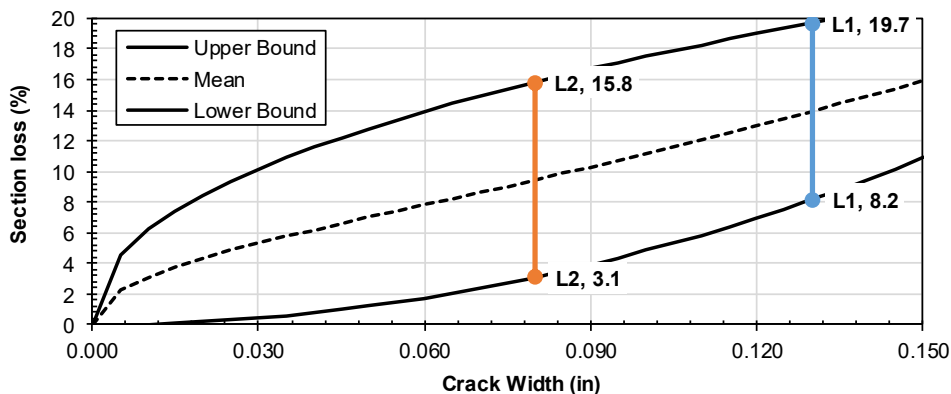


Figure 7.1. Snapshot of the spreadsheet developed to predict the extent of section loss

After predictive model development, calibration and validation were performed based on the existing literature and original data collected from the field. Specifically, estimates from various methods of field-estimating section loss (e.g., use of calipers, visual assessment, and engineering judgment) were compared to those made by 3D scanning and weight measurements, as well as mechanical testing. It should be noted that, due to the pandemic, the developed models had to be tested with limited rebar samples from only one bridge in Minnesota. Thus, despite the relative success of these tables, the range of section loss predictions remains relatively large.

To improve prediction accuracy and reduce the range of section loss estimates, additional calibration and validation efforts will be required. Such efforts will make further model validation, calibration, and refinement possible by extending the current study to target a large sample set (beyond the 10-rebar set used in the current project). It is anticipated that sample collection with at least 20 No. 4 bars, 20 No. 5 bars, and 20 No. 8 bars or more will greatly improve the accuracy of the predictive models. For this purpose, an additional set of three to four bridges will be selected to include a diversity of structure ages, rebar locations, and exposure conditions. Furthermore, a limited collection of rebars with epoxy coating will be planned to determine how epoxy-coated reinforcement experiences section loss over time. The outcome will lead to a robust dataset for the steel reinforcement section loss guidance tables that can be implemented by MnDOT and other agencies with the expected accuracy and uniformity.

REFERENCES

- Ahmad, S. (2003). Reinforcement corrosion in concrete structures, its monitoring and service life prediction—a review. *Cement and Concrete Composites*, 25(4-5), 459–471.
- Albrecht, P., & Naeemi, A. H. (1984). *Performance of weathering steel in bridges* (NCHRP Report 272). Washington, DC: National Cooperative Highway Research Program.
- Alexander, M. G., & Magee, B. J. (1999) Durability performance of concrete containing condensed silica fume. *Cement and Concrete Research*, 29(6), 917–922.
- Alipour, A., Shafei, B., & Shinozuka, M. (2011). Performance evaluation of deteriorating highway bridges in high seismic areas. *Journal of Bridge Engineering*, 16(5), 597-611.
- Alipour, A., Shafei, B., & Shinozuka, M. (2013). Capacity loss evaluation of reinforced concrete bridges located in extreme chloride-laden environments. *Journal of Structure and Infrastructure Engineering*, 9(1), 8-27.
- Alipour, A., & Shafei, B. (2022). An overarching framework to assess the life-time resilience of deteriorating transportation networks in seismic-prone regions. *Journal of Resilient Cities and Structures*, 1(2), 87-96.
- Alonso, C., Andrade, C. & Gonzalez, J. A. (1988). Relation between resistivity and corrosion rate of reinforcements in carbonated mortar made with several cement types. *Cement and Concrete Research*, 18(5), 687-698.
- Alonso, M. C., & Sanchez, M. (2009). Analysis of the variability of chloride threshold values in the literature. *Materials and Corrosion*, 60(8), 631–637.
- Andrade, C., Alonso, C., & Molina, F. J. (1993). Cover cracking as a function of bar corrosion: Part I — Experimental test. *Materials and Structures*, 26(8), 453–464.
- Andrade, C., & Alonso, C. (1996). Corrosion rate monitoring and on-site. *Science*, 10(5), 315–328.
- Andrade, C., Cesetti, A., Mancini, & G., Tondolo, F. (2016). Estimation of corrosion attack in reinforced concrete by means of crack opening. *Structural Concrete*, 17(4), 533-540.
- Angst, U. M. (2019). Predicting the time to corrosion initiation in reinforced concrete structures exposed to chlorides. *Cement and Concrete Research*, 115, 559–567.
- Angst, U., Elsener, B., Larsen, C. K., & Vennesland, Ø. (2009). Critical chloride content in reinforced concrete — A review. *Cement and Concrete Research*, 39(12), 1122–1138.
- Ann, K. Y., & Song, H.-W. (2007). Chloride threshold level for corrosion of steel in concrete. *Corrosion Science*, 49(11), 4113–4133.

- ASTM C876. (2016). ASTM C 876 standard test method for corrosion potentials of uncoated reinforcing steel in concrete. *Annual Book of ASTM Standards*, 1–8.
- ASTM G57. (2015). Standard test method for field measurement of soil resistivity using the Wenner four-electrode method. *ASTM standards*, 6 (Reapproved), 1–6.
- Bäßler, R., Burkert, A., Frølund, T., & Klinghoffer, O. (2003). Usage of GPM-portable equipment for determination of corrosion stage of concrete structures. *NACE - International Corrosion Conference Series*, March 16-20, San Diego, CA.
- Bentur, A., Diamond, S., & Berke, N. (1997). Steel corrosion in concrete. *Fundamentals and civil engineering practice* (pp. 41-43). London: E & FN Spon.
- Bjegovic, D., Krstic, V., & Mikulic, D. (2006). Design for durability including initiation and propagation period based on the fuzzy set theory. *Materials and Corrosion*, 57(8), 642-647.
- Castorena-González, J. H., Martin, U., Gaona-Tiburcio, C., Núñez-Jáquez, R. E., Almeraya-Calderón, F. M., Bastidas, J. M., & Bastidas, D. M. (2020). Modeling steel corrosion failure in reinforced concrete by cover crack width 3D FEM analysis. *Frontiers in Materials*, 7, 1-7.
- Cheng, X., Su, Q., Ma, F., Liu, X., & Liang, X. (2018). Investigation on crack propagation of concrete cover induced by non-uniform corrosion of multiple rebars. *Engineering Fracture Mechanics*, 201, 366-384.
- Chintakunta, S. (2014). *Non-destructive inspection protocol for reinforced concrete barriers and bridge railings* (FHWA Publication No. HRT-14-071). Washington, DC: FHWA.
- COIN – Concrete Innovation Centre. (2008). *Modeling of reinforcement corrosion in concrete – State of the art* (Gro Markeset and Roar Myrdal, COIN Project Report 7-2008). Oslo, Norway: COIN.
- Cox, D. R. (1992). *Planning of experiments*. New York: Wiley.
- Cui, Z., Alipour, A., & Shafei, B. (2019). Structural performance of deteriorating reinforced concrete columns under multiple earthquake events, *Engineering Structures*, 191, 460-468.
- Darwin, D., Browning, J., van Nguyen, T., & Carl Locke, J. (2002). *Mechanical and corrosion properties of a high-strength, high chromium reinforcing steel for concrete* (SD2001-05-F). Pierre, SD: South Dakota Department of Transportation.
- Du, Y. G., Chan, A. H., Clark, L. A., Wang, X. T., Gurkalo, F., & Bartos, S. (2013). Finite element analysis of cracking and delamination of concrete beam due to steel corrosion. *Engineering Structures*, 56, 8-21.
- DuraCrete. (1998). *Probabilistic performance-based durability design: Modeling of degradation* (Document No. BE95-1347/R4-5). Amsterdam, The Netherlands: DuraCrete.
- Eisenmann, D., & Margetan, F. (2018). *Validation study for detection and quantification of corrosion in bridge barrier rails* (InTrans Project 15-538). Ames, IA: Institute for Transportation.

- Elsener, B., & Böhni, H. (1992). Electrochemical methods for the inspection of reinforcement corrosion in concrete structures — Field experience. *Materials Science Forum*, 111–112, 635-646.
- Elsener, B., Andrade, C., Gulikers, J., Polder, R., & Raupach, M. (2003). Half-cell potential measurements — Potential mapping on reinforced concrete structures. *Materials and Structures*, 36(261), 461-471.
- Foley, R. (1970). Role of the chloride ions in iron corrosion. *Corrosion*, 26(2), 58-70.
- Gowers, K. R., & Millard, S. G. (1999). Measurement of concrete resistivity for assessment of corrosion severity of steel using Wenner technique. *ACI Materials Journal*, 96(5), 536-541.
- Gucunski, N., Imani, A., Romero, F., Nazarian, S., Yuan, D., Wigggenhauser, H., Shokouhi, P., Taffe, A., & Kutrubes, D. (2012). *Nondestructive testing to identify concrete bridge deck deterioration* (SHRP 2 Report No. S2-R06A-RR-1). Washington, DC: Transportation Research Board.
- Gucunski, N., Romero, F., Kruschwitz, S., Feldmann, R., & Parvardeh, H. (2011). *Comprehensive bridge deck deterioration mapping of nine bridges by nondestructive evaluation technologies* (Project SPR-NDEB [90]—8H-00, January). Ames, IA: Iowa Department of Transportation.
- Gulikers, J. (2005). Theoretical considerations on the supposed linear relationship between concrete resistivity and corrosion rate of steel reinforcement *Mater. Corros.*, 56, 393.
- Hajilar, S., & Shafei, B. (2018a). Atomic-scale investigation of physical adsorption of water molecules and aggressive ions to ettringite's surfaces. *Journal of Colloid and Interface Science*, 513, 104-116.
- Hajilar, S., & Shafei, B. (2018b). Structure, orientation, and dynamics of water-soluble ions adsorbed to basal surfaces of calcium monosulfoaluminate hydrates. *Journal of Physical Chemistry Chemical Physics*, 20, 24681-24694.
- Henriksen, C. F. (1993). Chloride penetration into concrete. *Proceedings of the International RILEM Workshop*, Chalmers Tekniska Högskola, Göteborg.
- Huet, B., L'hostis, V., Santarini, G., Feron, D., & Idrissi, H. (2007). Steel corrosion in concrete: Determinist modeling of cathodic reaction as a function of water saturation degree. *Corrosion Science*, 49(4), 1918-1932.
- Jol, H. M. (2009). *Ground penetrating radar theory and applications*. Oxford, UK: Elsevier.
- Katwan, M. J., Hodgkiess, T. & Arthur, P. D. (1996). Electrochemical noise technique for the prediction of corrosion rate of steel in concrete. *Materials and Structures*, 29(5), 286-294.
- Khan, I., Francois, R., & Castel, A. (2010). Prediction of reinforcement corrosion using corrosion induced cracks width in corroded reinforced concrete beams. *Cement and Concrete Research*, 56, 84–96.
- Khatami, D., Shafei, B., & Smadi, O. (2016). Management of bridges under aging mechanisms and extreme events: A risk-based approach. *Transportation Research Record: Journal of the Transportation Research Board*, 2550(1), 89-95.

- Khatami, D., & Shafei, B. (2021). Impact of climate conditions on deteriorating reinforced concrete bridges in the U.S. Midwest region. *Journal of Performance of Constructed Facilities*, 35(1), 04020129, 1-11.
- Khatami, D., Hajilar, S., & Shafei, B. (2021). Investigation of oxygen diffusion and corrosion potential through a cellular automaton framework. *Journal of Corrosion Science*, 187, 109496, 1-10.
- Kulkarni, A., & Shafei, B. (2018). Impact of extreme events on transportation infrastructure in Iowa: A Bayesian network approach. *Transportation Research Record: Journal of the Transportation Research Board*, 2672(48), 45-57.
- Lim, S., Akiyama, M., Frangopol, D. M., & Jiang, H. (2016). Experimental investigation of the spatial variability of the steel weight loss and corrosion cracking of reinforced concrete members: Novel X-ray and digital image processing techniques. *Structure and Infrastructure Engineering*, 13(1), 118-134.
- Mangat, P. S., El-Khatib, J. M., & Molloy, B. T. (1994). Microstructure, chloride diffusion and reinforcement corrosion in blended cement paste and concrete. *Cement and Concrete Composites*, 16(2), 73-81.
- Martínez, I., & Andrade, C. (2009). Examples of reinforcement corrosion monitoring by embedded sensors in concrete structures. *Cement and Concrete Composites*, 31(8), 545-554.
- Millard, S. G., & Broomfield, J. (2003). Measuring the corrosion rate of reinforced concrete using linear polarization resistance. *Concrete (London)*, 37(3): 36-38.
- Molina, F. J., Alonso, C., & Andrade, C. (1993). Cover cracking as a function of rebar corrosion: Part 2— Numerical model. *Materials and Structures*, 26(9), 532–548.
- Morinaga, S. (1988). *Prediction of service lives of reinforced concrete buildings based on rate of corrosion of reinforcing steel* (Report No. 23). Tokyo, Japan: Shimizu Corp.
- Morinaga, S. (1990). Prediction of service lives of reinforced concrete buildings based on rate of corrosion of reinforcing steel. *Proceedings of the 5th International Conference on Durability of Building Materials and Components*, November 7-9, Brighton, UK.
- Morinaga, S. (1996). Remaining life of reinforced concrete structures after corrosion cracking. *Proceedings of the 7th International Conference on the Durability of Building Materials*, 1, 127-136. May 19-23, Stockholm, Sweden.
- Otieno, M. (2014). The development of empirical chloride-induced corrosion rate prediction models for cracked and uncracked steel reinforced concrete structures in the marine tidal zone (Doctoral dissertation), University of Cape Town, Cape Town.
- Otieno, M. B., Beushausen, H.-D. & Alexander, M. G. (2010). Corrosion propagation in reinforced concrete structures — State of the art review and way forward. *Proceedings of the 6th international*

Conference on Concrete Under Severe Conditions — Environment and Loading, CONSEC'10, 1, 461-469. June 7-9, Merida, Yucatan, Mexico.

Otieno, M., Beushausen, H., & Alexander, M. (2011). Prediction of corrosion rate in reinforced concrete structures — A critical review and preliminary results. *Materials and Corrosion, 63*(9), 777-790.

Pettersson, K. (1995). Chloride threshold value and the corrosion rate in reinforced concrete. *Proceedings of Nordic Seminar on Corrosion of Reinforcement: Field and Laboratory Studies for Modelling and Service Life*. Lund, Sweden: Lund University.

Pourbaix, M. (1980). The linear bilogarithmic law for atmospheric corrosion. *Atmospheric corrosion* (pp. 107–121). New York: John Wiley and Sons.

Pour-Ghaz, M., Isgor, O. B., & Ghods, P. (2009). The effect of temperature on the corrosion of steel in concrete. Part 1: Simulated polarization resistance tests and model development. *Corrosion Science, 51*(2), 415-425.

Pradhan, B., & Bhattacharjee, B. (2009). Performance evaluation of rebar in chloride contaminated concrete by corrosion rate. *Construction and Building Materials, 23*(6), 2346-2356.

Qiao, D., Nakamura, H., Yamamoto, Y., & Miura, T. (2016). Crack patterns of concrete with a single rebar subjected to non-uniform and localized corrosion. *Construction and Building Materials, 116*, 366-377.

Ranjith, A., Rao, K. B., & Manjunath, K. (2016). Evaluating the effect of corrosion on service life prediction of RC structures – A parametric study. *International Journal of Sustainable Built Environment, 5*(2), 587-603.

Rodriguez, J., Ortega, L. M., Casal, J., & Diez, J. M. (1996). Corrosion of reinforcement and service life of concrete structures. *Durability of Building Materials and Components, 1*, 117-126

Rodríguez, P., Ramírez, E., & González, J. A. (1994). Methods for studying corrosion in reinforced concrete. *Magazine of Concrete Research, 46*(167), 81-90.

Scott, A. N. (2004). The influence of binder type and cracking on reinforcing steel corrosion in concrete (PhD thesis), Department of civil engineering, University of Cape Town, Cape Town.

Scott, A., & Alexander, M. G. (2007). The influence of binder type, cracking and cover on corrosion rates of steel in chloride-contaminated concrete. *Magazine of Concrete Research, 59*(7), 495-505.

Shafei, B. (2011). Stochastic finite-element analysis of reinforced concrete structures subjected to multiple environmental stressors. *Ph.D. Dissertation*, University of California, Irvine, CA.

Shafei, B., Alipour, A., & Shinozuka, M. (2012). Prediction of corrosion initiation in reinforced concrete members subjected to environmental stressors: A finite-element framework. *Cement and Concrete Research, 42*(2), 365-376.

- Shafei, B., Alipour, A., & Shinozuka, M. (2013). A stochastic computational framework to investigate the initial stage of corrosion in reinforced concrete superstructures. *Computer-Aided Civil and Infrastructure Engineering*, 28(7), 482-494.
- Shafei, B., & Alipour, A. (2015). Application of large-scale non-Gaussian stochastic fields for the study of corrosion-induced structural deterioration. *Engineering Structures*, 88, 262-276.
- Shafei, B., & Alipour, A. (2015). Estimation of corrosion initiation time in reinforced concrete bridge columns: How to incorporate spatial and temporal uncertainties. *Journal of Engineering Mechanics*, 141(10), 04015037, 1-12.
- Shi, W., Najimi, M., & Shafei, B. (2020a). Reinforcement corrosion and transport of water and chloride ions in shrinkage-compensating cement concretes. *Cement and Concrete Research*, 135, 106121, 1-9.
- Shi, W., Najimi, M., & Shafei, B. (2020b). Chloride penetration in shrinkage-compensating cement concretes. *Cement and Concrete Composites*, 113, 103656, 1-11.
- Song, H. W., & Saraswathy, V. (2007). Corrosion monitoring of reinforced concrete structures — A review. *International Journal of Electrochemical Science*, 2(1), 1-28.
- Song, H. W., Kim, H. J., Kwon, S. J., Lee, C. H., Byun, K. J., & Park, C. K. (2005). Prediction of service life in cracked reinforced concrete structures subjected to chloride attack and carbonation. *Proceedings of the International Conference on Cement Combinations for Durable Concrete*, Dundee, Scotland, U.K.
- Sørensen, H. E., & Frølund, T. (2002). Monitoring of reinforcement corrosion in marine concrete structures by the galvanostatic pulse method. *International Conference on Concrete in Marine Environments*, October 6-10, Hanoi, Vietnam.
- Stewart, M., & Rosowsky, D. (1998). Time-dependent reliability of deteriorating reinforced concrete bridge decks. *Journal of Structural Safety*, 20(1), 91-109.
- Stratfull, R. F., Jurkovich, W. J., & Spellman, D. L. (1975). Corrosion testing of bridge decks. *Transportation Research Record*, 539, 50-59.
- Streicher, P. E., & Alexander, M. G. (1995). A chloride conduction test for concrete. *Cement and Concrete Research*, 25(6), pp. 1284-1294.
- Thomas, M. (1996). Chloride thresholds in marine concrete. *Journal of Cement and Concrete Research*, 26(4), 513-519.
- Tuutti, K. (1993). Effect of cement type and different additions on service life. *Proceedings of the International Conference Concrete 2000 — Economic and Durable Construction through Excellence*, E&FN Spon, 1285-1295.

- Vassie, P. (1984). Reinforcement corrosion and the durability of concrete bridges. *Proceedings of the Institution of Civil Engineers, Part I*, 76, 713-723.
- Vidal, T., Castel, A., & Francois, R. (2007). Corrosion process and structural performance of a 17-year-old reinforced concrete beam stored in chloride environment. *Cement and Concrete Research*, 37(11), 1551–1561.
- Vidal, T., Castel, A., & Francois, R. (2004). Analyzing crack width to predict corrosion in reinforced concrete. *Cement and Concrete Research*, 34(1), 165–174.
- Vu, K., & Stewart, M. G. (2000). Structural reliability of concrete bridges including improved chloride induced corrosion models. *Structural Safety*, 22(4), 313-333.
- Yu, B., Liu, J., & Li, B. (2017). Improved numerical model for steel reinforcement corrosion in concrete considering influences of temperature and relative humidity. *Construction and Building Materials*, 142, 175-186.
- Yuan, Q., Shi, C., & De Schutter, G. (2009). Chloride binding of cement-based materials subjected to external chloride environment - A review. *Construction and Building Materials*, 23, 1-13.
- Zhang, J., Ling, X., & Guan, Z. (2017). Finite element modeling of concrete cover crack propagation due to non-uniform corrosion of reinforcement. *Construction and Building Materials*, 132, 487-499.
- Zhang, R., Castel, A., & Francois, R. (2010). Concrete cover cracking with reinforcement corrosion of RC beam during chloride-induced corrosion process. *Cement and Concrete Research*, 40(3), 415–425.
- Zhang, W., Zhou, B., Gu, X., & Dai, H. (2014). Probability distribution model for cross-sectional area of corroded reinforcing steel bars. *Journal of Materials in Civil Engineering*, 26(5), 822-832.
- Zhang, Y., & Su, R. K. (2019). Concrete cover delamination model for non-uniform corrosion of reinforcements. *Construction and Building Materials*, 223, 329-340.
- Zhu, W., & Francois, R. (2015). Structural performance of RC beams in relation with the corroded period in chloride environment. *Materials and Structures*, 48, 1757–1769.
- Zhu, W., Francois, R., & Liu, Y. (2017). Propagation of corrosion and corrosion patterns of bars embedded in RC beams stored in chloride environment for various periods. *Construction and Building Materials*, 145, 147-156.
- Zhu, W., Francois, R., Fang, Q., & Zhang, D. (2016). Influence of long-term chloride diffusion in concrete and the resulting corrosion of reinforcement on the serviceability of RC beams. *Cement and Concrete Composites*, 71, 144-152.
- Živica, V., Krajči L., Bágel, L., & Vargová, M. (1997). Significance of the ambient temperature and the steel material in the process of concrete reinforcement corrosion. *Construction and Building Materials*, 11(2), 99-103.

APPENDIX A: PHOTOS OF IN-PROGRESS REPAIRS

A.1 PIER 12WB



Figure A.1. East face of Pier 12WB



Figure A.2. South end of east face of Pier 12WB



Figure A.3. Spalling on south end of east face Pier 12WB



Figure A.4. Rebar section loss in spalling, east face Pier 12WB, with rebar diameters approximately 1/2" and 3/8", respectively



Figure A.5. West face of Pier 12WB



Figure A.6. Spalling and delamination on north side of the west face of Pier 12WB



Figure A.7. Spalling on west face of Pier 12WB showing longitudinal and stirrup rebar



Figure A.8. Corroded stirrup rebar diameter 9/16" on west face of Pier 12WB



Figure A.9. North end of Pier 12WB showing significant spalling on corners and exposure of longitudinal and stirrup rebar

A.2 PIER 15EB



Figure A.10. East face of Pier 15EB showing significant areas of delamination on top of the pier between beams on south side of beam and on bottom of the pier on the north side of the beam



Figure A.11. Spalling and delamination on east face of Pier 15EB showing exposed longitudinal and stirrup rebars between piles 3 and 4



Figure A.12. Exposed rebar to the north of pile 3 on Pier 15EB



Figure A.13. West face of Pier 15EB showing notable spalling on south end of the pier, delamination on top of beam above pile 5



Figure A.14. Vertical and horizontal portions of exposed stirrup shown in Pier 15EB Figure A.3, with rebar diameters of 19/32" and 3/8", respectively



Figure A.15. West end of Pier 15EB showing two areas of spalling, with entire south corner having rebar exposed nearly to pile 6



Figure A.16. South end of Pier 15EB showing nine stirrups and all longitudinal rebar on the west face entirely or partially exposed, as well as delamination on top and bottom of pier, most notably on the top near the midpoint of the two piles



Figure A.17. North end of west face of Pier 15EB showing corner and face spalling as well as delamination on the top of the pier



Figure A.18. Exposed stirrups on south end of the west face of Pier 15EB, with rebar diameters of 3/8" and 7/16", respectively



Figure A.19. Top of Pier 15EB at north-most beam connection, with connections showing extreme deterioration and corrosion and spalling evident at top of pier



Figure A.20. Spalling and delamination at north end of Pier 15EB



Figure A.21. Underneath Pier 15EB at pile 1, with rust stains present and spalling exposing longitudinal and stirrup rebar



Figure A.22. West face of Pier 15EB showing multiple spalling and delamination areas at north side of the pier



Figure A.23. South end of west face of Pier 15EB showing spalling on face of the pier, delamination on top and bottom of pier



Figure A.24. Severely corroded rebar specimens from south end of Pier 15EB

A.3 PIER 21EB



Figure A.25. East face of Pier 21EB showing pier encapsulated in RC



Figure A.26. Northern side of the east face of Pier 21EB showing spalling where concrete has fallen off as well as areas where concrete was retained during spalling



Figure A.27. Area of spalling on east face of Pier 21EB where stirrup rebar is exposed



Figure 28. Exposed corroded rebar with diameter of 3/4"



Figure A.29. West face of Pier 21EB



Figure A.30. North end of west face of Pier 21EB showing one area of spalling with exposed rebar



Figure A.31. Spalling with exposed stirrups on west face of Pier 21EB



Figure A.32. Exposed corroded rebar with diameter of 1/2"

A.4 PIER 48EB



Figure A.33. West face of Pier 48EB showing delamination between multiple columns and on the columns themselves



Figure A.34. Close-up of delaminated area in the center of the west face of Pier 48EB



Figure A.35. Underneath angle showing severe delamination on Pier 48EB



Figure A.36. East face of Pier 48EB



Figure A.37. Delamination exposing corroded rebar on top of Pier 48EB from the east face at the north side of the pier



Figure A.38. Exposed longitudinal and stirrup rebar with minimal corrosion from section shown in Figure A. 37, with rebar diameters of about 1/2" and 1 1/2", respectively



Figure A.39. Severely corroded stirrups, broken over top of Pier 48EB, and diameter reduced to approximately 1/2" on the east side



Figure A.40. Connection on top of Pier 48EB showing corrosion on the connecting plates and bolts



Figure A.41. East face of Pier 48EB



Figure A.42. Corroded longitudinal bars in area shown in Figure A.37, with rebar diameters of about 1 1/2"



Figure A.43. Delaminated area shown in Figure A.37 from the east side of Pier 48EB



Figure A.44. Exposed longitudinal bars with little corrosion on the east face of Pier 48EB



Figure A.45. Exposed rebar with mild corrosion from area in Figure A.37, with rebar diameters of 1 1/2" and 1/2", respectively



Figure A.46. Additional delaminated area on the west face of Pier 48EB



Figure A.47. Exposed rebar in area from Figure A.46, showing both stirrups and longitudinal bars

APPENDIX B: SAMPLE EXTRACTION

B.1 SAMPLES S4 AND S7 EXTRACTED FROM PIER 12WB

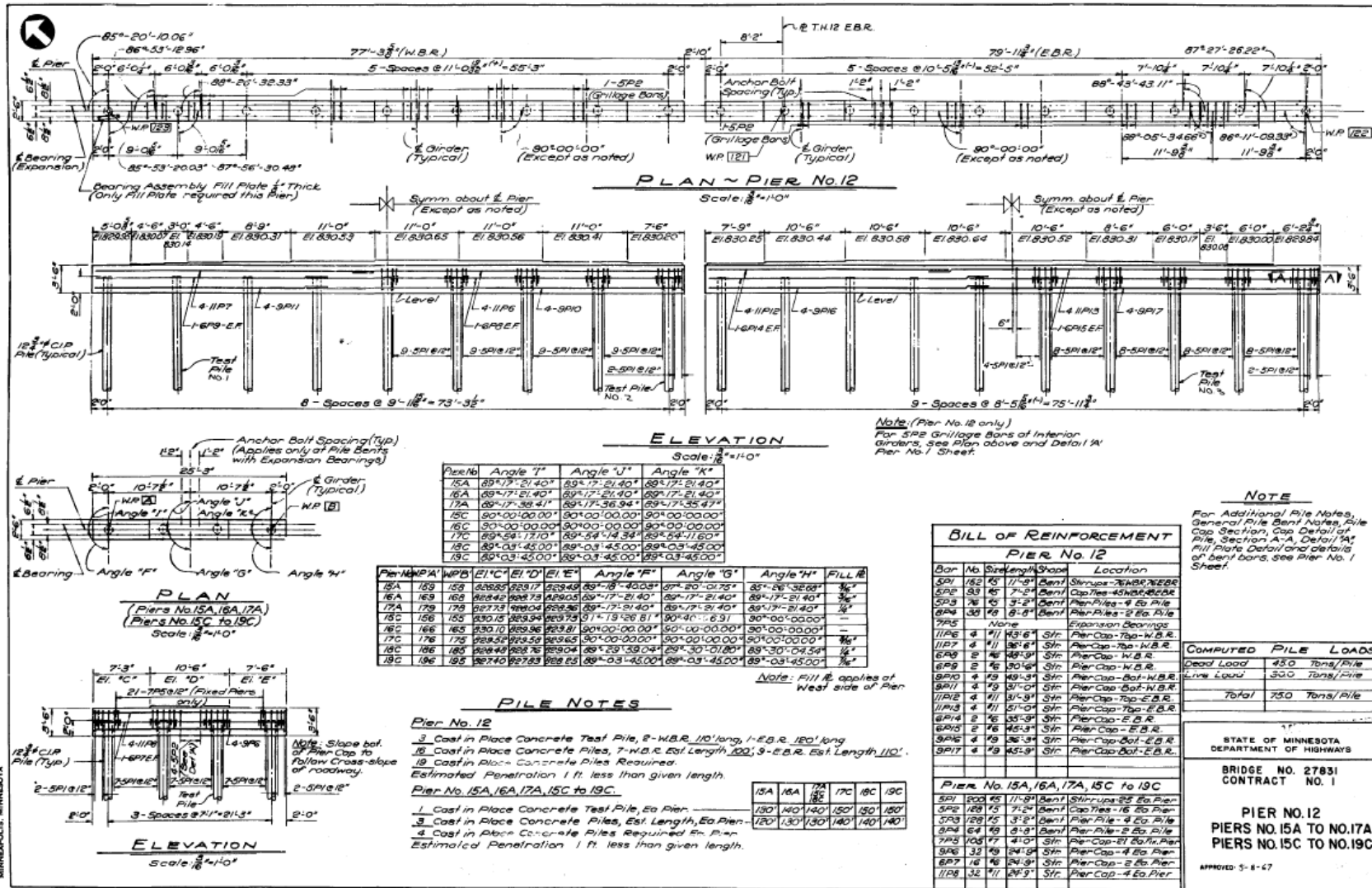


Figure B.1. Original design reinforcement

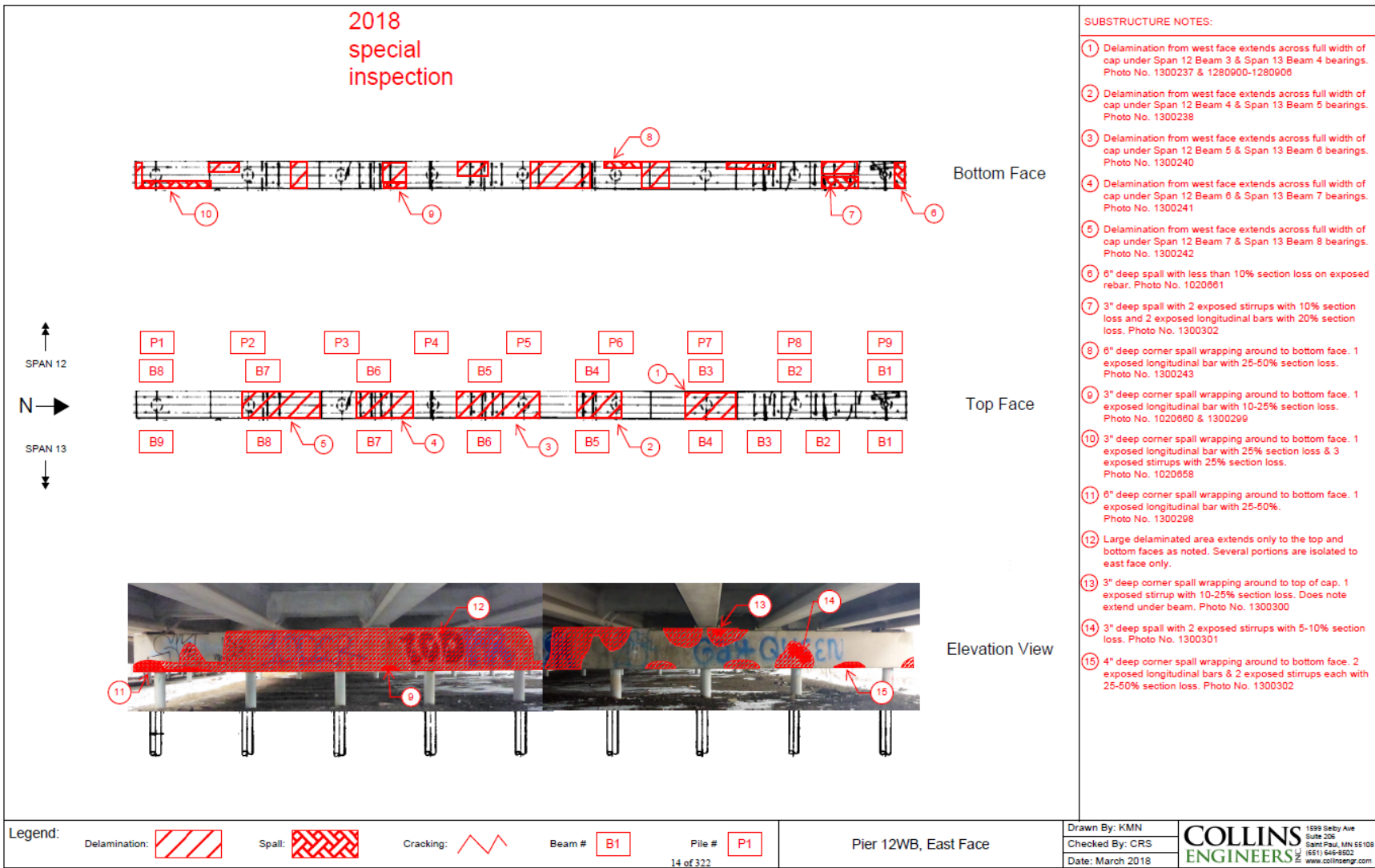
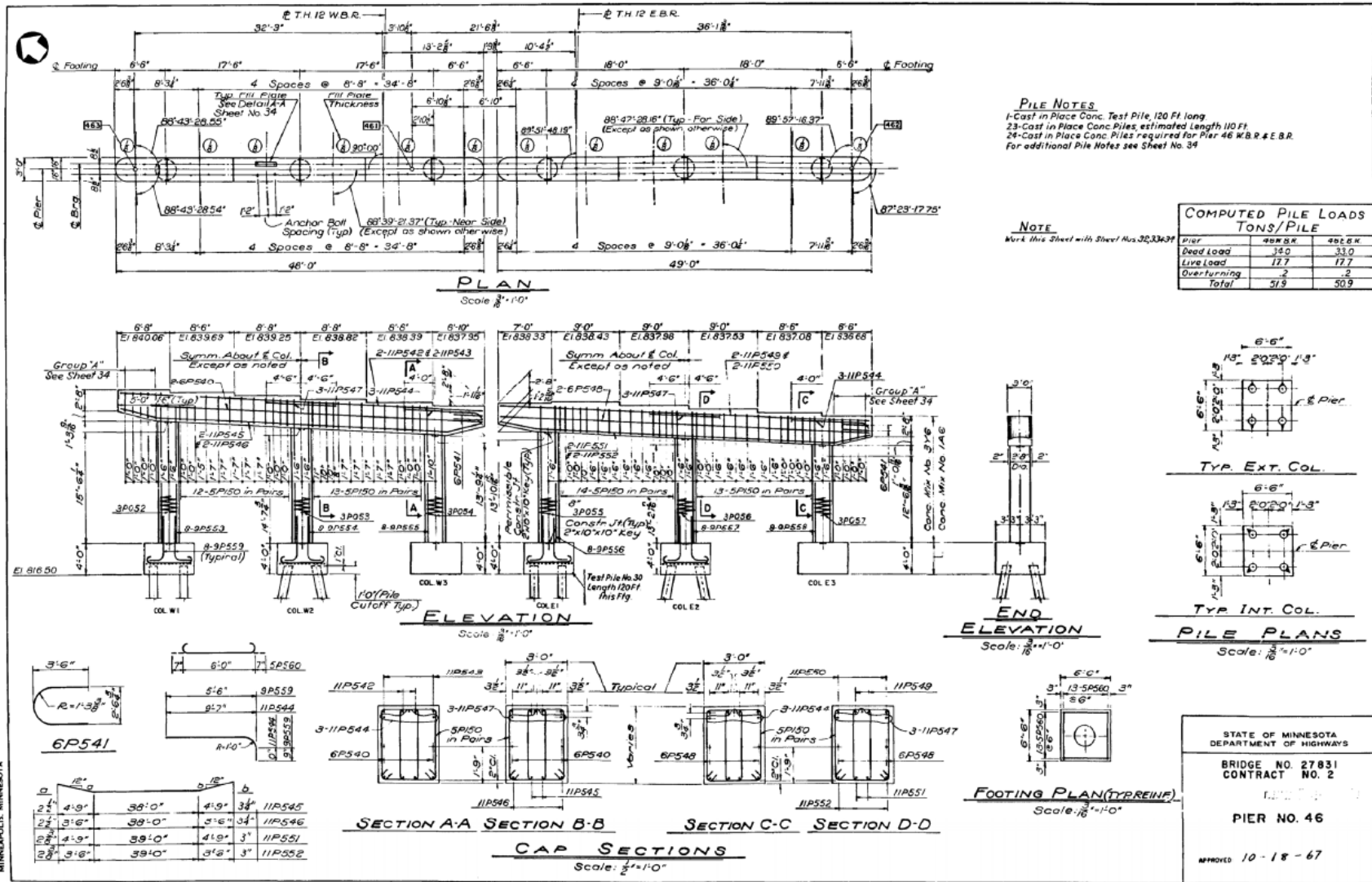


Figure B.2. Pre-project inspection sketches



Figure B.3. Sample rebar collection sites during contract repairs

B.2 SAMPLES S1 THROUGH S3, S6, AND S8 EXTRACTED FROM PIER 46WB



EDWARDS AND KELCEY
 ENGINEERS AND CONSULTANTS
 MINNEAPOLIS, MINNESOTA

STATE OF MINNESOTA
 DEPARTMENT OF HIGHWAYS
 BRIDGE NO. 27831
 CONTRACT NO. 2
 PIER NO. 46
 APPROVED 10-18-67
 SHEET NO. 24 OF 109 SHEETS 27831

Figure B.4. Original design reinforcement

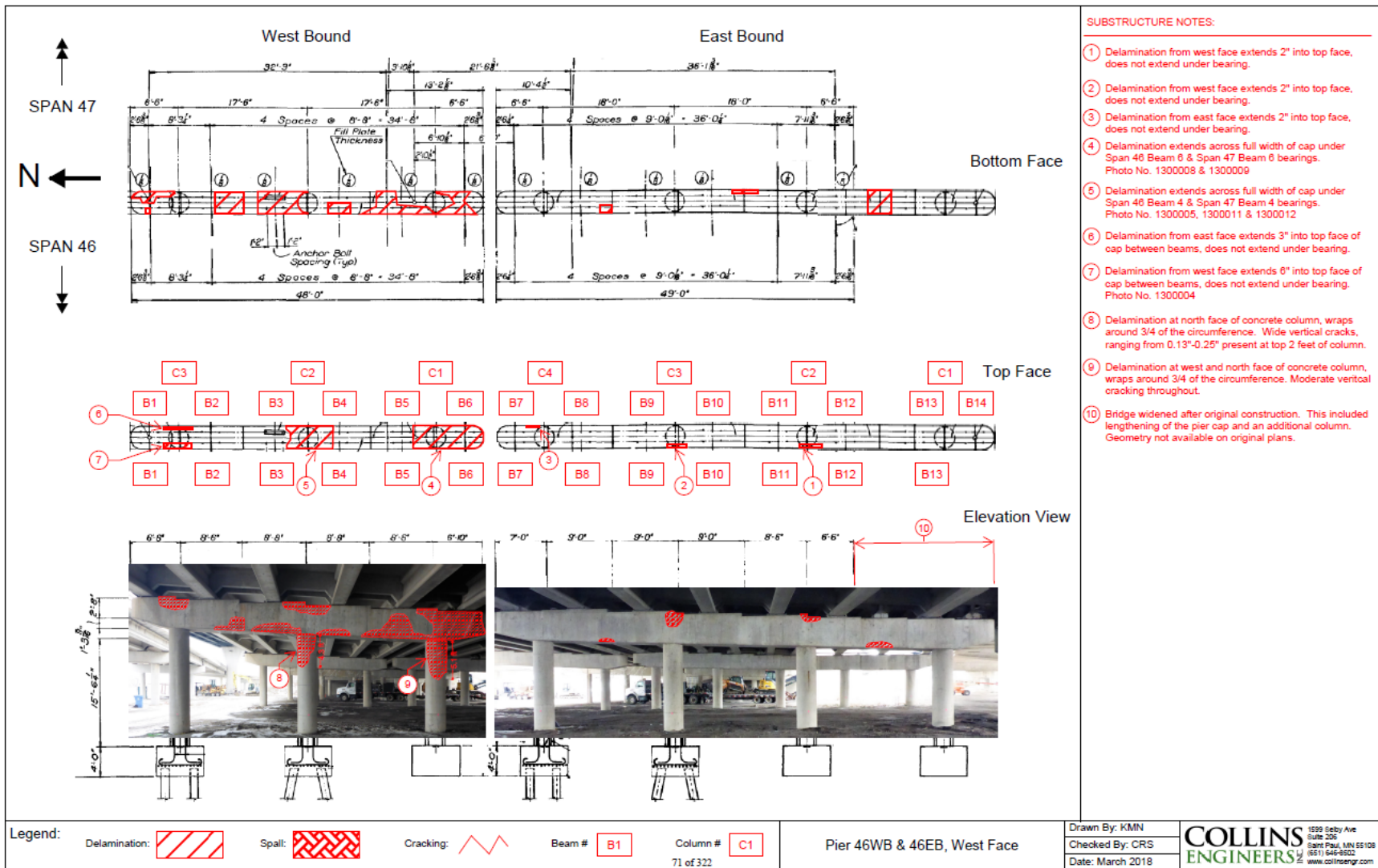


Figure B.5. Pre-project inspection sketches



Figure B.6. Sample rebar collection sites during contract repairs

B.3 SAMPLE S5 EXTRACTED FROM PIER 21EB

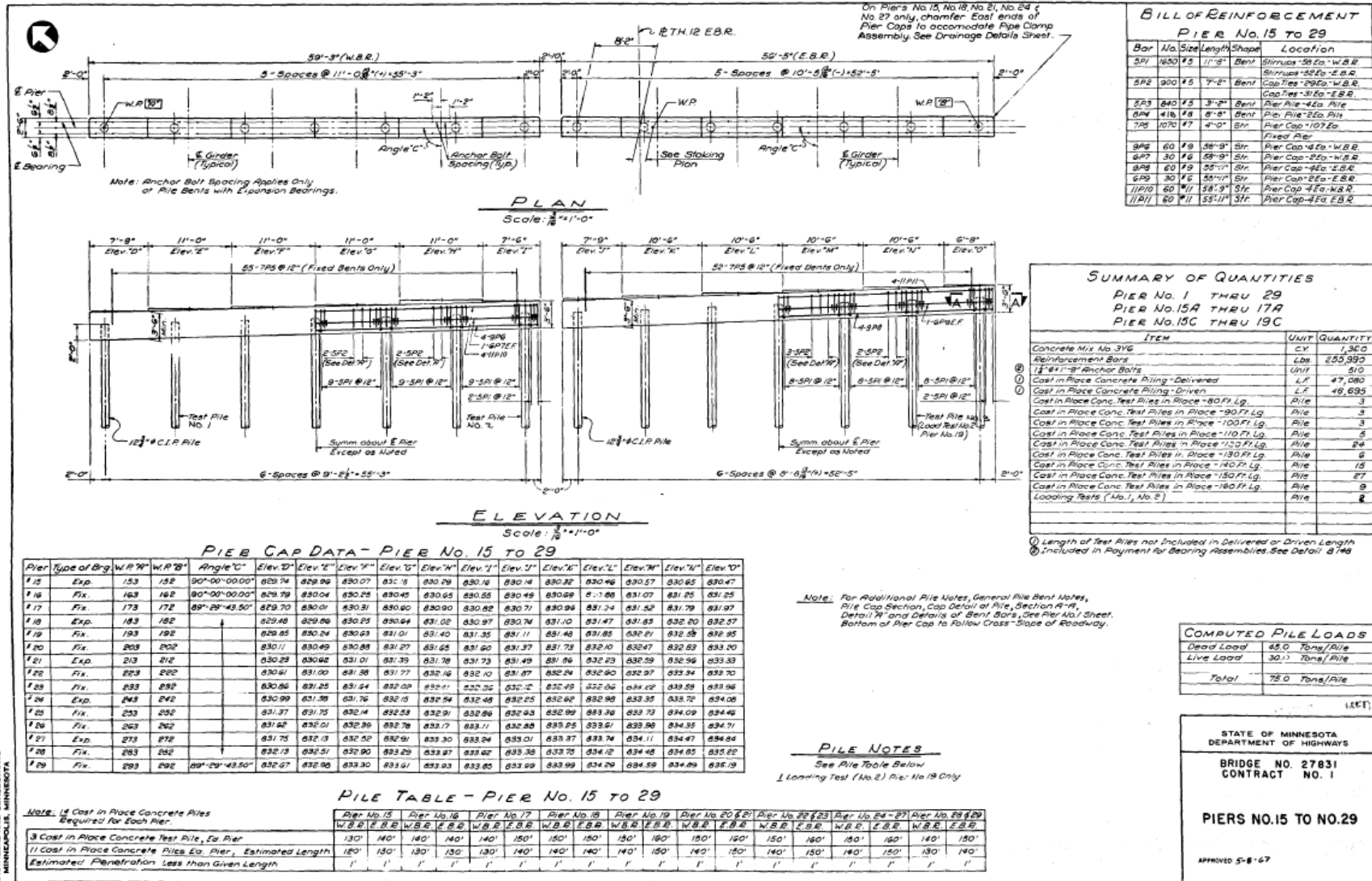


Figure B.7. Original design reinforcement

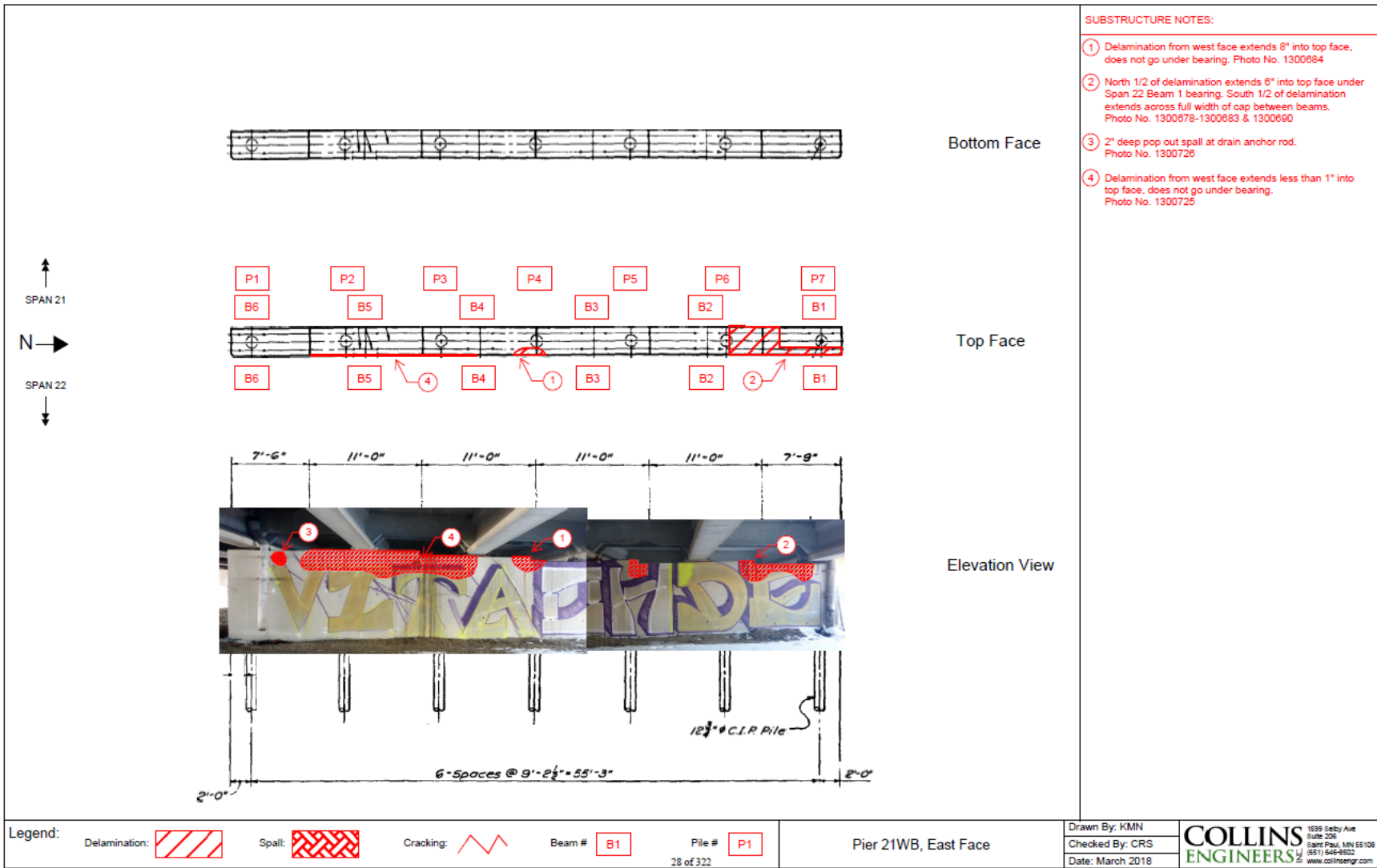


Figure B.8. Pre-project inspection sketches



Figure B.9. Sample rebar collection sites during contract repairs

B.4 SAMPLE S9 EXTRACTED FROM PIER 15A

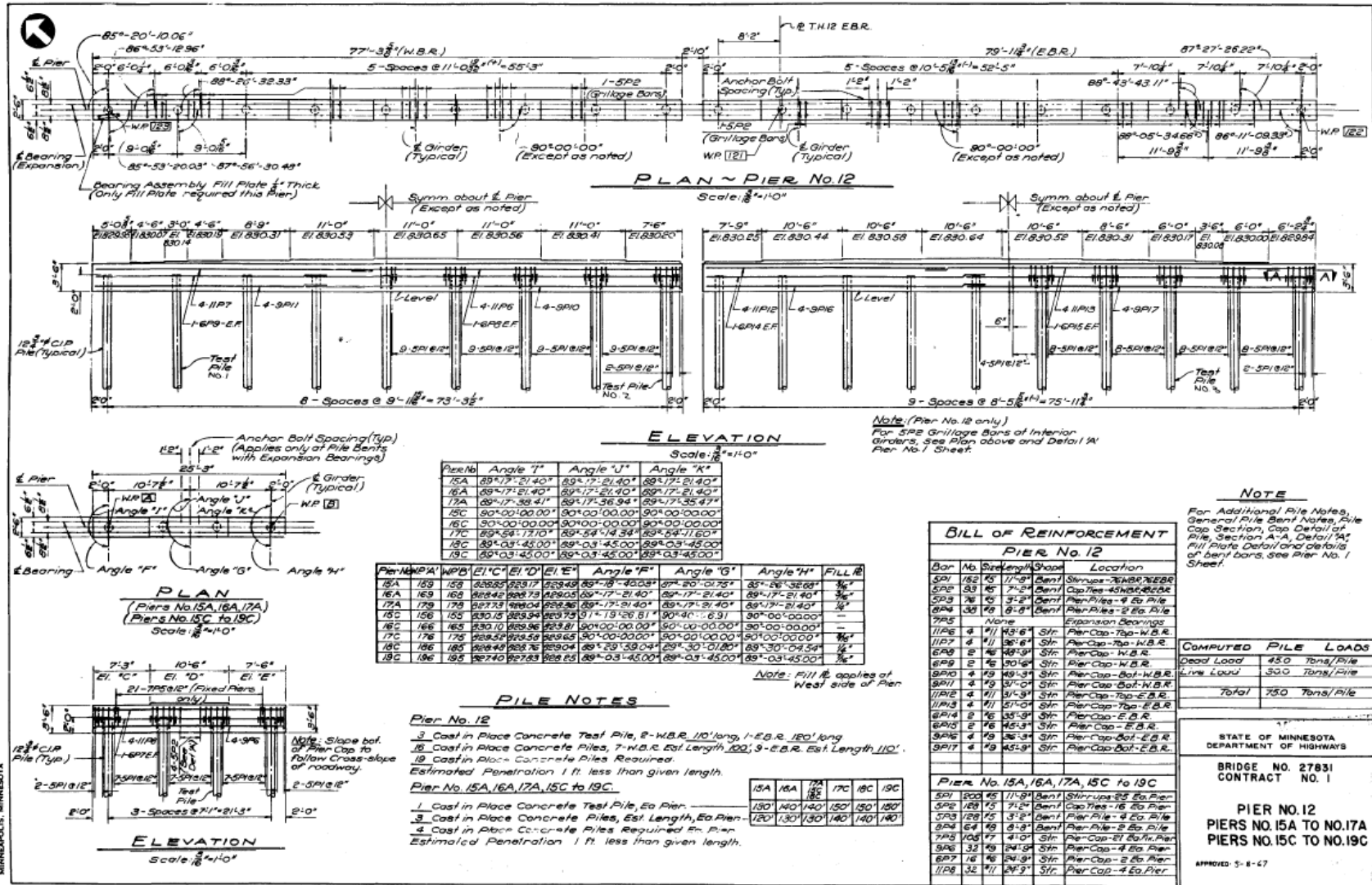


Figure B.10. Original design reinforcement

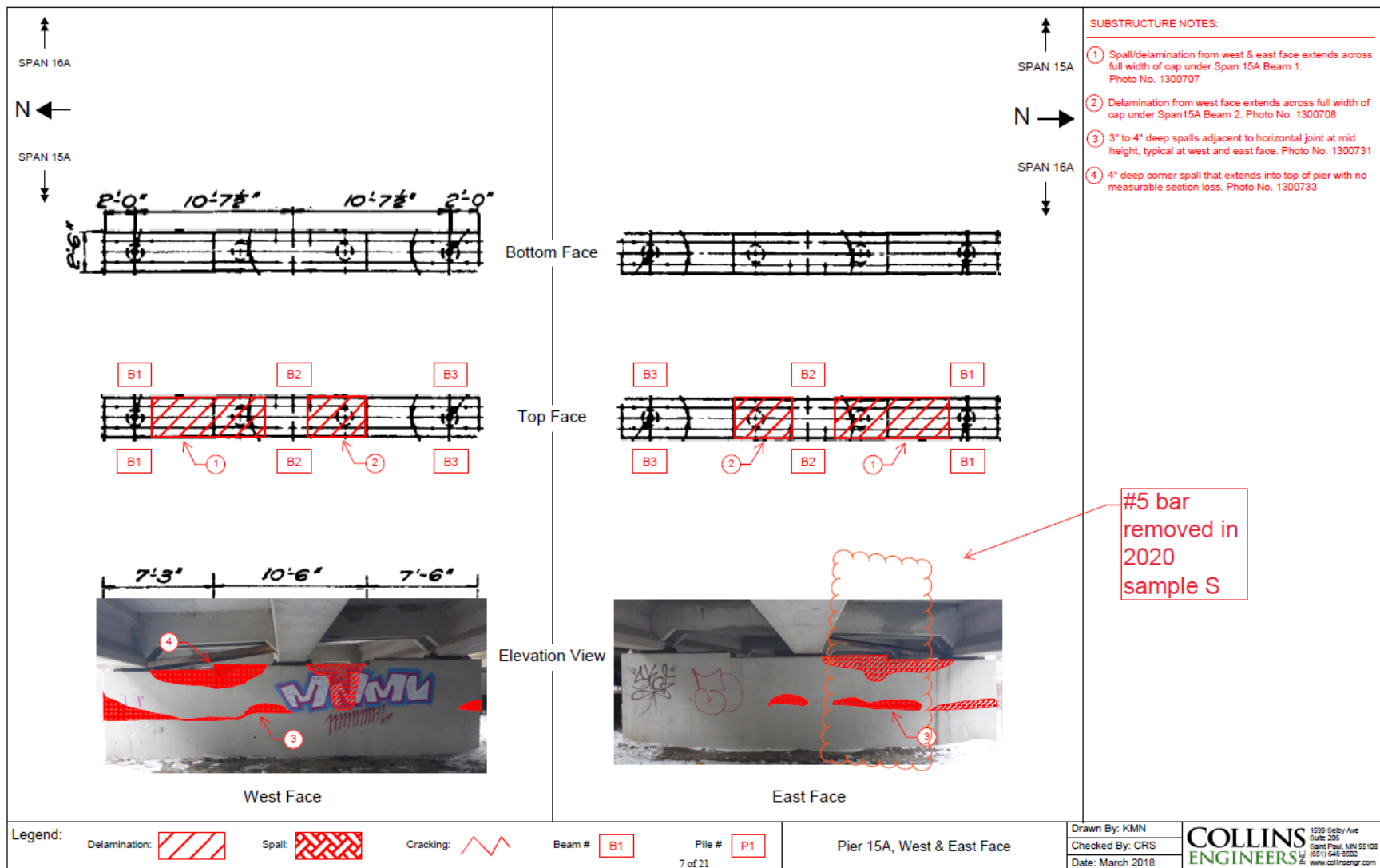


Figure B.11. Pre-project inspection sketches



Figure B.12. Sample rebar collection sites during contract repairs. Note that bar size for sample S9 exhibited larger than normal cross-sectional area for #5 rebar and therefore was assigned a #6 rebar designation in laboratory.